SYNTHESIS, CHARACTERIZATION AND BIOMEDICAL APPLICATIONS OF SURFACE FUNCTIONALIZED NANOPARTICLES

By

SUMAN RANA

CHEM01200904024

Bhabha Atomic Research Centre, Mumbai

A thesis submitted to the
Board of Studies in Chemical Sciences

In partial fulfillment of requirements
for the Degree of

DOCTOR OF PHILOSOPHY
of
HOMI BHABHA NATIONAL INSTITUTE

December, 2015

Homi Bhabha National Institute

Recommendations of the Viva Voce Committee

As members of the Viva Voce Committee, we certify that we have read the dissertation prepared by **Suman Rana** entitled **"Synthesis, Characterization and Biomedical Applications of Surface Functionalized Nanoparticles"** and recommend that it may be accepted as fulfilling the thesis requirement for the award of Degree of Doctor of Philosophy.

Chairman – **Dr. D. Das**		Date: 30/9/16
Guide / Convener – **Dr. P. A. Hassan**		Date: 30/9/2016
Member 1 – **Dr. S. Kapoor**		Date: 30/9/16
Member 2 – **Dr. S. Adhikari**		Date: 30/9/16
Member 3 – **Dr. G. Verma**		Date: 30/9/16
External Examiner- **Dr. Nand Kishore Prasad**		Date: 30/9/16

Final approval and acceptance of this thesis is contingent upon the candidate's submission of the final copies of the thesis to HBNI.

I hereby certify that I have read this thesis prepared under my direction and recommend that it may be accepted as fulfilling the thesis requirement.
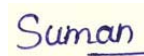
Date: 30/9/2016

Place: Mumbai

Dr. P. A. Hassan
Guide

STATEMENT BY AUTHOR

This dissertation has been submitted in partial fulfillment of requirements for an advanced degree at Homi Bhabha National Institute (HBNI) and is deposited in the Library to be made available to borrowers under rules of the HBNI.

Brief quotations from this dissertation are allowable without special permission, provided that accurate acknowledgement of source is made. Requests for permission for extended quotation from or reproduction of this manuscript in whole or in part may be granted by the Competent Authority of HBNI when in his or her judgment the proposed use of the material is in the interests of scholarship. In all other instances, however, permission must be obtained from the author.

Suman

Suman Rana

DECLARATION

I, hereby declare that the investigation presented in the thesis has been carried out by me. The work is original and has not been submitted earlier as a whole or in part for a degree / diploma at this or any other Institution / University.

Suman

Suman Rana

List of Publications arising from the thesis

Journal

1. "Folic acid conjugated Fe_3O_4 magnetic nanoparticles for targeted delivery of doxorubicin",
Suman Rana, N. G. Shetake, K. C. Barick, B. N. Pandey, H. G. Salunke and P. A. Hassan
Dalton Trans. (2016) accepted.

2. "PEG functionalized luminescent lipid particles for cellular imaging"
Suman Rana, K. C. Barick, N. G. Shetake, G. Verma, V. K. Aswal, L. Panicker, B. N. Pandey and P. A. Hassan
Chem. Phys. Lett. 2016, 659, 225-229.

3. "Stimuli responsive carboxyl PEGylated Fe_3O_4 nanoparticles for therapeutic applications"
Suman Rana, K. C. Barick and P. A. Hassan
J. Nanofluids 2015, 4, 1-7.

4. "Surface modification of magnetic nanoparticles for therapeutic applications"
K. C. Barick, **Suman Rana** and P. A. Hassan
J. Surface Sci. Technol. 2015, 31, 123–132.

5. "Making sense of brownian motion: Colloids characterisation by dynamic light scattering"
P. A. Hassan, **Suman Rana** and G. Verma
Langmuir 2015, 31, 3-12.

6. "Polyaniline shell cross-linked Fe_3O_4 magnetic nanoparticles for heat activated killing of cancer cells"
Suman Rana, Neena V. Jadhav, K. C. Barick, B. N. Pandey and P. A. Hassan
Dalton Trans. 2014, 43, 12263-12271.

7. "Biocompatible phosphate anchored Fe_3O_4 nanocarriers for drug delivery and hyperthermia"
P. Sharma, **Suman Rana**, K. C. Barick and P. A. Hassan
New J. Chem. 2014, 38, 5500-5508.

8. "Folate-conjugated luminescent Fe_3O_4 nanoparticles for magnetic hyperthermia"
K. C. Barick, **Suman Rana** and P. A. Hassan
AIP Conf. Proceedings 2013, 1591, 561-562.

9.   "Microstructural investigation of lipid solubilized microemulsions using laser light scattering"
Suman Rana, G. Verma and P. A. Hassan
Adv. Mat. Lett. 2013, 4, 476-481.

Chapters in Book

1.   "Interfacial engineering of nanoparticles for cancer therapeutics"
Suman Rana, J. Bhattacharjee, K. C. Barick, G. Verma, P. A. Hassan and J. V. Yakhmi
Therapeutic Nanostructures Multi Volume SET (I-V), Elsevier.

Conferences

Papers presented at national/ international conferences:

1. Cysteine modified magnetic nanoparticles for drug delivery applications; **Suman Rana**, K. C. Barick, Neena G. Shetake, B. N. Pandey and P. A. Hassan; *5th Interdisciplinary Symposium on Materials Chemistry,* Dec. 9-13, 2014, BARC, Mumbai (Received 2nd best poster award).

2. Folate conjugated magnetic nanocarriers for targeted drug delivery and hyperthermia treatment of cancer; **Suman Rana**, K. C. Barick and P. A. Hassan; *Faraday Discussions 175*, September 17-19, 2014, University of Bristol, United Kingdom.

3. Biocompatible Fe_3O_4 nanoparticles for targeted cancer therapy; **Suman Rana**, K. C. Barick and P. A. Hassan; *National Conference on Advances in Synthetic and Materials Chemistry (NCASMC-2014),* Mar. 10-11, 2014, University of Mumbai, Mumbai, India.

4. Bifunctional Fe_3O_4 nanoparticles via thiol-ene click reaction for targeted cancer therapy; **Suman Rana**, K. C. Barick and P. A. Hassan; *7th India-Singapore symposium on experimental condensed matter physics,* Feb. 24-26, 2014, IIT Bombay, Mumbai, India.

5. Folic acid-FITC tagged Fe_3O_4 nanoparticles for thermal therapy; K. C. Barick, **Suman Rana** and P. A. Hassan; *Mumbai-Pune Soft Matter Meeting,* Jan. 25, 2014, BARC, Mumbai, India.

6. PEG functionalized Fe_3O_4 nanoparticles for targeted drug delivery, **Suman Rana**, K. C. Barick and P. A. Hassan; *Mumbai-Pune Soft Matter Meeting,* Jan. 25, 2014, BARC, Mumbai, India.

7. Folate-conjugated luminescent Fe_3O_4 nanoparticles for magnetic hyperthermia; K. C. Barick, **Suman Rana** and P. A. Hassan; *58th DAE Solid State Physics Symposium* (*SSPS 2013*), Dec 17-21, 2013, Thapar University, Patiala, India.

8. PEGylated Fe_3O_4 nanoparticles for therapeutic application; **Suman Rana**, K. C. Barick, J. K. Sainis, A. Gupta and P. A. Hassan; *58th DAE Solid State Physics Symposium* (*SSPS 2013*), Dec. 17-21, 2013, Thapar University, Patiala, India.

9. Synthesis and characterization of core-shell nanoparticles for hyperthermia applications, *Research Scholars Meet (RSM),* February 15-16, 2013, Mumbai.

10. Fe$_3$O$_4$-polyaniline nanocomposites for biomedical applications; **Suman Rana**, K. C. Barick and P. A. Hassan; *4th Interdisciplinary Symposium on Materials Chemistry (ISMC)*, Dec. 11-15, 2012, BARC, Mumbai (Received 3rd best poster award).

11. Laser light scattering studies of solid lipid nanoparticles prepared in surfactants; **Suman Rana**, G. Verma, P. A. Hassan; *Emerging Trends in Applications of Lasers & Accelerators in Nanomaterials (ETALAN),* Oct. 20-21, 2011.

Participated at national/ international conferences:

1. Attended 2 days, *National Workshop on Material Chemistry (NWMC),* December 2011, BARC, Mumbai.

2. Attended one day seminar on *Emerging Frontiers in Nano Delivery Systems,* Mar. 19, 2011 in Indian Institute of Chemical Technology, Matunga (Mumbai).

3. Attended *3rd International Symposium on Materials Chemistry (ISMC),* Dec. 7-11, 2010, BARC, Mumbai.

Suman Rana

Dedicated to......

My loving daughter, Zinnia

&

Husband, Mr. Paramjit Rana

ACKNOWLEDGEMENTS

Though only my name appears on the cover of this thesis, many people have contributed to its completion. These pages reflect the support of many generous and inspiring people who contributed in many ways to the success of this study and made this journey an unforgettable experience for me. The list is long, but I would like to express my gratitude to all of them who have encouraged and contributed both academically and emotionally during the tenure of my research.

*At this moment of accomplishment, first of all I pay my sincere gratitude to my guide, **Dr. P. A. Hassan**, for being a constant source of motivation, guidance and continuous encouragement throughout the course of this work and giving me a chance to accelerate my research skills in the field of nanotechnology. His expertise, understanding and patience have added greatly to my research experience. It's his patience and support, which helped me to overcome many crises and finish this dissertation. I am also thankful to him for his assistance and guidance in improving my writing skill and for constant help by means of productive discussions, showing me how to improve the presentation of my work, which will surely be helpful in the future also.*

*I give my sincere thanks to **Dr. K. C. Barick**, as the present research work would have never been completed without his proper guidance, regular supervision, and constant encouragement. His expertise in nanostructured materials along with his vision of nanotechnology has been the source of inspiration to me for further research in the field. His ability to explain things clearly, paying attention to details, his in-depth knowledge, dedication to quality research, careful and critical reading of my*

CONTENTS

SYNOPSIS

During the last decade, there has been extensive effort to explore applications of nanostructured materials in various biomedical devices and processes. One of the prerequisite for successful use of nanoparticles for biological applications is its biocompatibility and ability to target to the site of interest. Interfacial modification of nanoparticles plays a crucial role in this respect. Magnetic nanoparticles offer a range of opportunities for biomedical research, as their response can be tailored by choosing from a variety of magnetic materials with different magnetic properties that can be manipulated by the use of external magnetic fields and by modification of their surfaces with molecules specific for intended applications [1].

Magnetic nanoparticles are a major class of nanoscale materials with the potential to revolutionize current clinical diagnostic and therapeutic techniques. Due to their unique physical properties and ability to function at the cellular and molecular level of biological interactions, they are being actively investigated as the next generation contrast agents for magnetic resonance imaging (MRI), carriers for targeted drug delivery, heating sources for hyperthermia treatment of cancer and magnetic separation agent in separation science [2-4]. The advantage of magnetic nanoparticles in biotechnology arises from a multitude of properties. First, they have sizes that place them at dimensions comparable to those of a virus (20–500 nm), a protein (5–50 nm) or a gene (2 nm wide and 10–100 nm long). Second, the nanoparticles are magnetic, and hence can be manipulated by an external magnetic field gradient. Third and finally, nanoparticles have a large surface that can be properly modified to attach biological agents. Applications in nanobiotechnology impose strict requirements on the particles physical, chemical and pharmacological

properties, including chemical composition, granulometric uniformity, crystal structure, magnetic behaviour, surface structure, solubility and low own toxicity. For example, in order for magnetic drug-targeting to be safe and effective (with the minimum amount of magnetic particles, a maximum of drug should be easily administered and transported to a specific site), the following parameters of the nanomagnets are critical: (a) particle size (small as possible to improve tissular diffusion, and to have long sedimentation times and high effective surface areas), (b) surface characteristics (easy encapsulation of the magnetic nanoparticles protects them from degradation and provides biocompatibility), and (c) good magnetic response. The recent surge of interest in nanotechnology has significantly expanded the breadth and depth of magnetic nanoparticles research. They have been explored in a wide range of applications in the detection, diagnosis, and treatment of illnesses, such as cancer [5], cardiovascular disease [6], and neurological disease [7-8]. Amongst the various magnetic nanoparticles, Fe_3O_4 nanoparticulates have received a great deal of attention due to their potential applications such as contrast agent for MRI, hyperthermia treatment of cancer and drug delivery.

Surface modification of magnetic nanoparticles is important to render them not only non-toxic, biocompatible, soluble in water, but chemically functional, and thus allow a targetable delivery with particle localization in a specific area [9]. Higher effective surface area of nanoparticles facilitates easy attachment of ligands, lower sedimentation rates (high stability in colloidal suspension) and improved tissular diffusion. For most of therapeutic applications, the first significant challenge is to avoid undesirable uptake of nanoparticles by the reticulo-endothelial system (RES) [10]. The next step is to achieve selective targeting of the system to the site of interest

for the in-vivo studies. Surface functionalized small sized nanoparticles have higher diffusion rates which increase the concentration of nanoparticles at the centre of a blood vessel, thereby limiting the interactions of nanoparticles with endothelial cells and prolonging the nanoparticles blood circulation time.

The objectives of the present study have been the fabrication of surface modified Fe_3O_4 nanoparticulates, and the investigation of their structural/ microstructural, thermal and magnetic properties and exploration of their applications in biomedical field. The results obtained from the present investigations have been described and compiled under different chapters of this thesis, along with an introduction to the topic. A brief account of each chapter has been given below.

Chapter 1: Introduction to nanomaterials

This chapter deals with the basic introduction to the present work, literature survey related to the surface functionalization of magnetic nanoparticles, general information about properties of magnetic nanomaterials and various synthesis approaches. This chapter also provides the background for understanding and exploring the biomedical applications of magnetic nanoparticles. The gap areas have been identified and the objective of the present investigations is clearly brought out.

Chapter 2: Experimental techniques

A brief overview of the different experimental techniques used in the current thesis has been illustrated in this chapter. The working principle of dynamic light scattering technique (DLS), X-ray diffraction (XRD), UV-visible spectrophotometer, zeta potential measurements, Fourier transforms infrared spectroscopy (FTIR) and induction heating measurements has been explained. Some other complementary

techniques employed for the characterization of MNPs such as thermogravimetric analysis (TGA), transmission electron microscope (TEM), magnetic measurements, cell culture, cell viability measurements, confocal microscopic measurements are also discussed.

Chapter 3: Synthesis and characterization of polyethylene glycol modified Fe_3O_4 magnetic nanoparticles for biomedical applications

With the objective of introducing polyethylene glycol coating and anionic charge on the surface of magnetic nanoparticles for cationic drug binding, polyethylene glycol diacid (PEG-diacid) is used as a coating material. The main characteristic of PEG-diacid is that it has two carboxylic moiety at the terminal positions and this PEG diacid is chemisorbed onto the surface of Fe_3O_4 nanoparticles through one carboxylate ion (COO−) leaving the other one free on the surface. The free carboxylate group creates the negative charge on the surface of magnetic nanoparticles which is advantageous for the conjugation of positively charged anticancer drug, doxorubicin (DOX).
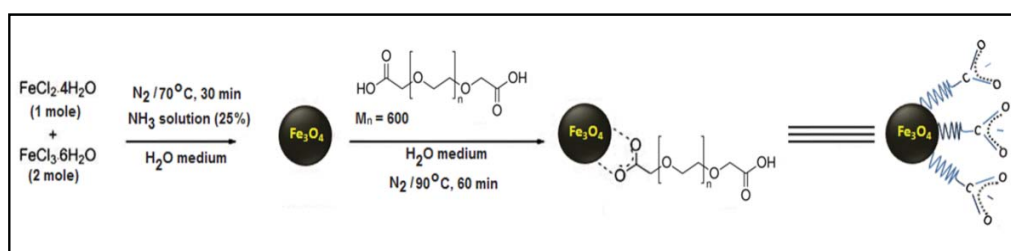
Fig. 1. *Schematic representation of the synthesis of CPMN.*

In this chapter, carboxyl PEGylated Fe_3O_4 magnetic nanoparticles (CPMN) have been synthesized by a facile soft-chemical approach. CPMN were prepared by co-

precipitation of Fe^{2+} and Fe^{3+} in basic medium followed by *in-situ* coating of PEG-diacid (Fig. 1).

XRD analysis of the samples revealed that Fe_3O_4 nanoparticles crystallize into a single phase inverse- spinel structure with an average crystallite size of ~10 nm. The carboxyl PEGylation of Fe_3O_4 is evident from FTIR spectra, DLS, TGA and zeta-potential measurements. The 'colloidal' stability of these CPMN samples may be due to the formation of hydrogen bonds between the carboxyl groups of functionalized magnetic nanoparticles and water. CPMN exhibit superparamagnetic behaviour at room temperature and the maximum magnetization was found to be 67.5 emu/g at 20 kOe. The drug loading and release behaviour of CPMN was investigated by using doxorubicin hydrochloride (DOX) as a model drug to evaluate their potential as a carrier system. Results show high loading affinity of negatively charged CPMN for positively charged anticancer drug and their sustained release in the mild acidic environments. This is desirable for cancer therapy as the relatively low pH in tumors will stimulate the DOX release at the target site. Additionally, the time-dependent calorimetric measurements show good specific absorption rate (SAR) of CPMN suspension, which indicate that these nanoparticles can also be used as effective heating source for hyperthermia treatment of cancer. The heat activated killing of cancer cells (Mouse Fibrosarcoma Cells, WEHI-164) was evaluated under AC magnetic field (AMF) with respective controls using the MTT assay. The MTT assay with WEHI-164 cells clearly shows that CPMN suspension is highly biocompatible and does not have toxic effect for further *in-vivo* use. Furthermore, these magnetic nanoparticles can be explored for the targeted drug delivery by exploiting their surface functionality.

Chapter 4: Polyaniline shell cross-linked Fe_3O_4 magnetic nanoparticles for heat activated killing of cancer cells

Effective transfer of heat from the magnetic core to the surrounding medium is one of the key requirements of thermal therapy. Conducting polymer shell is important for the easy transport of heat from the core of magnetic nanoparticles to the medium for the killing of the cancer cells. For this purpose, we used Polyaniline (PANI) which has unique π-conjugated structures, good environmental stability and high electrical conductivity. Carboxyl PEGylated Fe_3O_4 magnetic nanoparticles (CPMN, discussed in the previous chapter) were chosen as the core material for fabrication of the polyaniline shell due to their high negative surface charge and good aqueous colloidal stability.

Polyaniline shell cross-linked magnetic nanoparticles (PSMN) have been synthesized by *in-situ* polymerization of aniline hydrochloride on the surface of CPMN. XRD and TEM (Fig. 2a) analysis revealed the formation of single phase inverse spinel Fe_3O_4 nanoparticles of size about 10 nm. The successful growth of polyaniline shell on the surface of CPMN is evident from FTIR spectra, DLS, TGA, zeta-potential and magnetic measurements. DLS measurements indicate that PSMN show monomodal distribution with mean hydrodynamic diameter of 65 nm (polydispersity index ~0.2). The larger hydrodynamic diameter of PSMN as compared to CPMN (40 nm) is primarily due to the presence of associated and hydrated long chain organic layers. As DLS is weighted towards large sizes, the average hydrodynamic diameter could be higher than those obtained from TEM.

.
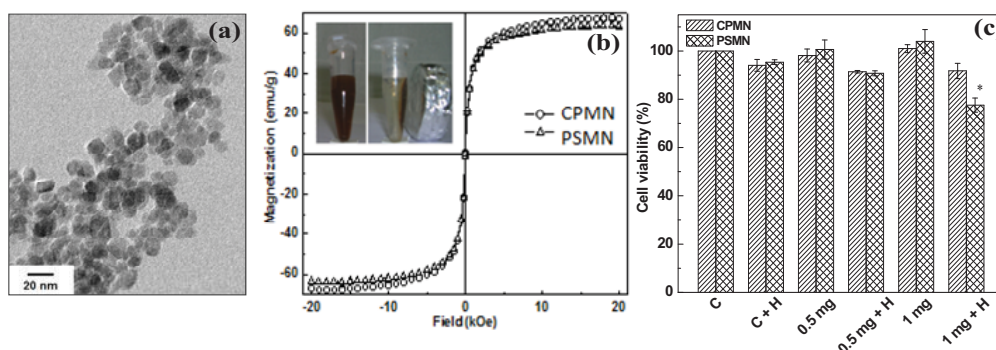
Fig. 2. *(a) TEM micrograph of PSMN, (b) M vs H plots of CPMN and PSMN (Inset shows PSMN suspension in the presence and absence of permanent magnet of field strength ~2.5 kOe) and (c) Viability of WEHI-164 upon exposure of AMF for 10 min in presence of CPMN and PSMN.*

Further, the average hydrodynamic diameter and polydispersity index hardly varies with time revealing their excellent aqueous colloidal stability. These nanoparticles are hydrophilic in nature possibly due to the formation of hydrogen bonds between surface functional groups and water. In order to assess the potential of PSMN in hyperthermia, we have investigated their magnetic and thermomagnetic properties. PSMN exhibit superparamagnetic behaviour at 300 K (Fig. 2b). The maximum magnetization was found to be 63.5 emu/g at 20 kOe. The low magnetization of PSMN as compared to CPMN is due to the grafting of polyaniline shell, which directly affects the crystallo-chemical properties of the magnetic nanoparticles surface and leads to an increase in the magnetically disordered surface layer. However, the retention of superparamagnetic property at room temperature with biocompatible organic shell makes these nanoparticles suitable as effective heating source for hyperthermia treatment of cancer cells. It has been observed that the heating efficacy of PSMN under AMF slightly reduced as compared to that of CPMN which is obvious as they possess less magnetic moment. Further, PSMN shows high

loading affinity for anticancer drug doxorubicin, its sustained release and substantial internalization in tumor cells. The enhanced toxicity of PSMN to cancer cells under AMF suggests their strong potential for magnetic hyperthermia (Fig. 2c). We believe that such composite structures of PANI and PEG could be advantageous for the effective heat transport from the Fe_3O_4 core to the surrounding medium.

Chapter 5: Biocompatible phosphate anchored Fe_3O_4 magnetic nanocarriers for drug delivery and hyperthermia

The most common strategies used for surface functionalization of magnetic nanocarriers comprise coating of bioactive organic and inorganic molecules onto the surface of nanoparticles. The presence of these bioactive layers on the surface not only stabilizes the iron oxide nanoparticles, but also provides accessible surface for conjugation of biomolecules and drugs. The phosphonates and phosphates have a strong affinity towards transition metal oxide surfaces. Sodium hexametaphosphates (SHMP), a food additive and its use as a stabilizer in the generation of nanoparticles is safe.

In this chapter, biocompatible, water-dispersible phosphate anchored Fe_3O_4 magnetic nanocarriers (PAMN) has been synthesized by *in-situ* functionalization of Fe_3O_4 nanoparticles with SHMP during co-precipitation of Fe^{2+} and Fe^{3+} ions in basic medium. SHMP was chosen as the coating material due to its low toxicity and immunogenicity. These nanoparticles show better aqueous colloidal stability, good magnetic response and excellent self-heating efficacy under external AC magnetic field. The bioactive shell not only provides colloidal stability to the particles but also create functionalized exteriors with high densities of phosphate moieties for conjugation of drug molecules. Furthermore, nanocarriers showed high loading

affinity for DOX and their sustained release profile under acidic environment. This sustained release of drug is desirable for cancer therapy as the relatively low pH in tumors will specifically stimulate the release of drug at the target site. Specifically, high loading affinity for DOX with their sustained release profile and self-heating capacity makes these novel nanocarriers suitable for drug delivery and magnetic hyperthermia.

Chapter 6: Folic acid conjugated magnetic nanoparticles for targeted cancer therapy

Bifunctional magnetic nanoparticles (BMNPs) which contains a carboxylic moiety for drug binding and folate receptor for drug targeting were prepared by introducing bioactive cysteine molecules onto the surface of undecenoic acid coated Fe_3O_4 magnetic nanoparticles (UMNPs) via thiol-ene click reaction. The XRD and TEM analysis reveal the formation of highly crystalline single-phase Fe_3O_4 nanostructures. These nanoparticles are of average size 10 nm and resistant to protein adsorption under physiological medium. FTIR spectra clearly suggest that cysteine molecules were successfully conjugated to the surface of UMNPs. The changes in the interfacial characteristics of the particles and the presence of organic coating were confirmed from dynamic light scattering, zeta-potential, thermogravimetric and field-dependent magnetic measurements. Induction heating experiments suggest that these nanoparticles possess excellent self-heating efficiency under external AC magnetic field. The efficacy of the carriers in heat activated killing of cancer cells is expressed in terms of the specific absorption rate (SAR). The SAR values of BMNPs (1 mg/ml of Fe) were found to be 41.2, 64.0 and 88.0 W/g of Fe with an applied field of 0.251, 0.335 and 0.419 kOe, respectively (at a fixed frequency of 265 kHz). This indicates

superior heating ability of these particles. Further, the infrared thermal imaging indicates that the temperature rise can be localized to the region of interest. To achieve site specific targeting of the carrier to cancer cells, the cysteine functionalized particles were conjugated with folic acid via amide linkage. This leads to the formation of bifunctional particles with free carboxyl group on cysteine for binding of cationic drugs like doxorubicin. These folate conjugated nanoparticles (FBMNPs) show high loading affinity for doxorubicin and pH dependent release profile. This is highly conducive for cancer therapy as the relatively low pH in tumours will specifically stimulate the drug release at the site of interest.

Chapter 7: Luminescent marker loaded Fe_3O_4 nanoparticles for drug tracking

MNPs conjugated with specific luminescent markers (FITC, lanthanides) and targeting receptors (FA, peptides) can provide detailed understanding of disease-related biological processes at the molecular level. Luminescent markers are used to track the MNP location in the body from the fluorescence images.

In this chapter, the synthesis of folate-conjugated luminescent iron oxide nanoparticles (FLIONs) and their application has been discussed. XRD and TEM analyses reveal the formation of highly crystalline single-phase Fe_3O_4 nanoparticles of size about 10 nm. The conjugation of folate receptor (folic acid, FA) and luminescent molecule (fluorescein isothiocyanate, FITC) onto the surface of nanoparticles was evident from FTIR and UV-visible spectroscopy. These FLIONs show good colloidal stability, high magnetic field responsivity and excellent self-heating efficacy. Specifically, a new class of magnetic nanoparticles has been fabricated, which can be used as an effective heating source for hyperthermia.

Chapter 8: Conclusion and future scope

This chapter summarizes the work; the important conclusions arrived at from the analysis of the present investigations and scope for future work.

In summary, different types of surface functionalized magnetic nanoparticles were successfully fabricated. The various structural aspects, effects of some physical parameters, the magnetic properties and possible applications of these nanoparticles were investigated.

References

1. B. L. Cusching, V. L. Kolesnichenko and C. J. O'Connor, Recent Advances in the Liquid-Phase Syntheses of Inorganic Nanoparticles, *Chem. Rev.* **104** (2004) 3893-3946.

2. K. C. Barick, S. Singh, N. V. Jadhav, D. Bahadur, B. N. Pandey and P. A. Hassan, pH-responsive peptide mimic shell cross-linked magnetic nanocarriers for combination therapy, *Adv. Funct. Mater.* **22** (2012) 4975–4984.

3. J. Cheon and J.- H. Lee, Synergistically integrated nanoparticles as multimodal probes for nanobiotechnology, *Acc. Chem. Res.* **41** (2008) 1630–1640.

4. K. C. Barick and P. A. Hassan, Glycine passivated Fe_3O_4 nanoparticles for thermal therapy, *J. Coll. Interf. Sci.* **369** (2012) 96–102.

5. M. Ferrari, Cancer nanotechnology: opportunities and challenges, *Nature Reviews, Cancer* **5** (2005) 161-171.

6. S. A. Wickline, A. M. Neubauer, P. M. Winter, S. D. Caruthers and G. M. Lanza, Molecular imaging and therapy of atherosclerosis with targeted nanoparticles, *Journal of magnetic Resonance Imaging* **25** (2007) 667-680.

7. C. Corot, K.G. Petry, R. Trivedi, A. Saleh, C. Jonkmanns, J. F. Le Bas, E. Blezer, M. Rausch, B. Brochet, P. Foster-Gareau, D. Baleriaux, S. Gaillard and V. Dousset, Macrophage imaging in central nervous system and in carotid atherosclerotic plaque using ultrasmall superparamagnetic iron oxide in magnetic resonance imaging, *Investigative Radiology* **39** (2004) 619-625.

8. C. Sun, J. S. H. Lee and M. Zhang, Magnetic nanoparticles in MR imaging and drug delivery*, Adv. Drug Deliv. Rev.* **60** (2008) 1252-1265.

9. A. Ito, M. Shinkai, H. Honda and T. Kobayashi, Medical application of functionalized magnetic nanoparticles, *J. Biosci. Bioeng.* **100** (2005) 1–11.

10. V. Lenaerts, J. F. Nagelkerke, T. J. Van Berkel, P. Couvreur, L. Grislain, M. Roland and P. Speiser, In vivo uptake of polyisobutyl cyanoacrylate nanoparticles by rat liver Kupffer, endothelial, and parenchymal cells, *J. Pharm. Sci.* **73** (1984) 980-982.

LIST OF FIGURES

distribution.

LIST OF TABLES

LIST OF ABBREVIATIONS

NPs	Nanoparticles
QDs	Quantum dots
MNPs	Magnetic nanoparticles
M	Magnetization
H	Magnetic field
Fe_3O_4	Magnetite
AMF	Alternating magnetic field
PEG	Polyethylene glycol
MRI	Magnetic resonance imaging
DMSA	2, 3-dimercapto succinic acid
TEOS	Tetraethoxyortho silane
CT	Computed tomography
SAR	Specific absorption rate
Cys- Fe_3O_4 NPs	Cysteine modified Fe_3O_4 magnetic nanoparticles
CH	Chitosan
GLD	Glutaraldehyde
CA-MNP	Citric acid functionalized Fe_3O_4 nanoparticles
DOX	Doxorubicin
EPR	Enhanced permeability and retention
SPIO	Superparamagnetic iron oxide
SPION	Superparamagnetic iron oxide nanoparticles
RES	Reticuloendothelial system
MPS	Mononuclear phagocyte system
siRNA	Small interfering RNA
Tf-L-DOX/VER	Transferrin-conjugated liposomes with DOX and verapamil
FA	Folic acid
FA-PEG-PEI-PCL	FA-PEG-polyethyleneiminepoly (caprolactone)
MDT	Magnetic drug targeting
FA-PEG-SPION NCs	FA and PEG-modified SPION nanoclusters

PMNCs	pH responsive peptide mimic shell cross-linked magnetic nanocarriers
DOX-PMNCs	DOX-loaded PMNCs
XRD	X-ray diffraction
DLS	Dynamic light scattering
FTIR	Fourier transforms infrared spectroscopy
SAR	Specific absorption rate
UV	Ultra-violet
Hkl	Miller indices
FWHM	Full width at half maximum
JCPDS	Joint Committee on Powder Diffraction Standards
KBr	Potassium bromide
OPD	optical path difference
DTGS	Deuterated triglycine sulphate
PZC	isoelectric point
IR	Infrared
AB	Acetate Buffer
PBS	Phosphate buffer saline
TEM	Transmission electron microscope
HRTEM	High resolution transmission electron microscopy
BF	Bright field
TGA	Thermogravimetric analysis
ZFC	Zero-field cooled
FC	Field cooled
NaCl	Sodium chloride
SRB	Sulforhodamine B
MTT	3-(4,5-dimethylthiazol-2-yl)-2,5-diphenyltetrazolium bromide
DMSO	Dimethyl sulfoxide
BSA	Bovine serum albumin
PEG-diacid	Poly (ethylene glycol) bis (carboxymethyl) ether
NHS	N-Hydroxysuccinimide

EDC	1-ethyl-3-(3-dimethylaminopropyl) carbodiimide
AIBN	Azobisisobutyronitrile
DMEM	Dulbecco's modified eagle medium
FCS	fetal calf serum
CPMN	Carboxyl PEGylated Fe_3O_4 magnetic nanoparticles
ILP	Intrinsic loss power
PSMN	Polyaniline shell cross-linked magnetic nanoparticles
PDI	Polydispersity index
PANI	Polyaniline
HAP	Hydroxyapatite
PAMN	Phosphate anchored Fe_3O_4 magnetic nanoparticles
SHMP	Sodium hexametaphosphate
FR	Folate receptors
BMNPs	Bifunctional Fe_3O_4 magnetic nanoparticles
UMNPs	Undecenoic acid coated Fe_3O_4 magnetic nanoparticles
FBMNPs	Folic acid conjugated BMNPs
AIONs	Amine functionalized iron oxide nanoparticles
FIONs	Folate-conjugated iron oxide nanoparticles
FLIONs	Folate-conjugated luminescent iron oxide nanoparticles
RT	Room temperature
FITC	Fluorescein isothiocyanate
LSM	Lipid solubilized microemulsions
LPs	Lipid particles
LLPs	Luminescent lipid particles
IPM	Isopropyl myristate
SANS	Small angle neutron scattering
DSC	Differential Scanning Calorimetry

Chapter 1

Introduction to nanomaterials

The term 'nanomaterials' is used to describe materials and systems that possess length scale between 1 to 100 nm in at least one dimension and 'nanotechnology' refers to products derived from them. In practise, nanotechnology combines chemical science, physical science, engineering and material science which provide different applications in biology, medicine, information technology and environmental science. Nanomaterials, such as nanoparticles, nanowires, nanotubes and thin films etc. provide a useful platform for the development of wide-ranging therapeutic and diagnostic applications in the biomedical area. Among the various forms of nanomaterials, nanoparticles have huge potential for application in the field of biomedicine.

1.1. Nanoparticles (NPs)

In general, nanoparticles (NPs) are spherical particles, whether naked or functionalized, measuring <100 nm of radius, though other shapes can also come under this class. NPs can exhibit novel properties that are different from their molecular and bulk forms. One of the reasons behind the novel properties of NPs is the high surface area to volume ratio. Surface effects are negligible in the bulk materials but are very much significant in nanoparticles. Because their properties differ from those of their bulk counterparts, NPs offer a wide range of potential applications based on their unique characteristics. For example, one way of obtaining beautiful colours to the stained glass windows are a result of the presence of small metal oxide clusters in the glass. It is due to that the particles of different sizes scatter different wavelengths of light, imparting different colours to the glass. Different types of NPs arranged by their novel physical properties are discussed in next sections.

1.1.1. Metallic nanoparticles

Metal NPs consist of metallic elements with at least one dimension between 1-100 nm. As metals are very abundant elements in periodic table with various physical properties, metal NPs can possess a variety of properties that are determined by a set of physical parameters such as composition, size, shape and structure. Advancements in the fabrication of metal NPs provide tools to fine-tune their electronic, optical, catalytic and magnetic properties by controlling the different parameters. Superparamagnetism and surface plasmon resonance (SPR) are two distinct properties of magnetic and optically active metal NPs, respectively which are useful for biomedical applications. When the size of ferromagnetic NPs are reduced below to a critical size, ambient thermal energy can be sufficient to switch and randomize the magnetic spin direction, resulting in a net magnetization of zero. This behaviour is called superparamagnetism. Above certain critical temperature, called "blocking" temperature, superparamagnetic materials have no net permanent magnetic moment in the absence of magnetic field; however they can quickly respond to an external magnetic field. The critical size is dependent on the material, and is typically less than 20 nm. The transition temperature from ferromagnetism to superparamagnetism is also determined by the size of NPs. Superparamagnetic NPs include Co [1], Fe [2], Ni [3], FePt [4], CoPt [5], CoPt$_3$ [6] and FeCoPt [7] NPs. These NPs have demonstrated their potential for imaging and therapeutic applications such as magnetic resonance imaging (MRI) and magnetic hyperthermia therapy [8]. Metallic NPs exhibit SPR, which are coherent oscillations of their conduction electrons throughout each nanoparticle that are excited by the electrical field of light. They can resonantly absorb and scatter incident light upon excitation of their surface

plasmon oscillations. Copper, silver and gold NPs are known to show colour because of their plasmon frequencies in the visible spectrum. The plasmon resonance frequency is dependent on the volume, size and shape of the NPs. When two metallic NPs are in close proximity to each other, the electric fields of their plasmon resonances may couple, resulting in a red-shift in the plasmon frequency. Small colloidal particles of silver are used in photography for image formation. Further, the catalytic behaviour of the metals depends upon their size. For example, gold NPs (2-5 nm) can be used for catalytic activity where the structure is icosahedral instead of the bulk face centred cubic (FCC) arrangement. Odour eaters in bathrooms are based on gold NPs on Fe_2O_3 substrate [9]. Noble metal NPs have many biomedical applications as they have pronounced SPR effect that can be easily tuned by their size, shape and structure [10]. SPR properties of spherical gold NPs are restricted in the visible region but they can be easily shifted to near Infrared (NIR) region by changing their shapes from gold nanospheres to nanorod, nanoshell, or nanocage [11-12]. These SPR characteristics in NIR region can be beneficial for biomedical applications that demand deep tissue penetrations.

1.1.2. Semiconductor nanoparticles

Semiconductor NPs or quantum dots (QDs) are fluorescent nanocrystals with their typical size in the range of 1–10 nm. The size regime shows quantum phenomena such as atomic-like electronic structure and discrete energy levels, which results in novel optical and electronic properties that cannot be observed in bulk semiconductor materials [13-14]. Electron-hole pairs (excitons) can be generated upon optical or electronic excitation of QDs, and recombination of the excitons can result in photoluminescence (PL) emission. The optical absorption/emission properties of QDs

can be tuned by their size, shape and chemical composition. QDs have many advantages over conventional organic dyes, which includes the large absorption coefficient, bright PL emission (~10–100 times brighter than single organic dye), narrow and symmetric emission profile and high photochemical stability [15-16]. The high photostability and notable brightness of QDs can allow long-term acquisition of PL emissions with a good signal-to-noise ratio. This can be advantageous for cellular labelling [17-19], single molecular tracking [20] and *in-vivo* imaging [21-24]. QDs have continuous and broad absorption spectra, which suits well for achieving simultaneous and multi-colour signals. Their narrow and symmetric emission profiles allow effective unmixing of the PL signals. The emission wavelength regime of QD spans from UV-visible to infrared, and thus opens a large spectral window for multiplexed imaging [23-24]. Over the past two decades, cadmium chalcogenide QDs such as CdS [25], CdSe [25], CdTe [25] QDs have been extensively studied. Especially, CdSe/ZnS (core/shell) QD has been well studied for the synthesis and for biological applications among others [16]. For bio imaging applications, near-infrared is more advantageous for the QD emission because it provides longer tissue penetrations by the reduced photon scatterings and auto fluorescence.

Many NIR emitting QDs, including PbSe [26], CdTe/CdSe (core/shell) [27], PbS, InAs and Ag_2S. QDs have been developed. For example, CdTe/CdSe QDs injected intradermally into living pigs could be taken up by sentinel lymph nodes and could clearly visualize the lymph nodes in 1 cm depth in tissue [22].

1.1.3. Metal oxide nanoparticles

Metal oxides exhibit a wide variety of structures, properties and phenomena. They have been used in many important technology areas, including magnetic ferrites,

ferroelectric oxides (barium strontium titanate (BST), lead zirconate titanate (PZT)), superconductors ($YBa_2Cu_3O_{7-x}$), ionic conductors (yittria-stabilized zirconia (YSZ)), phosphors, and photocatalysts (TiO_2) [28-29]. Among the others, magnetic metal oxide NPs are widely used in biomedical applications such as MRI and magnetic hyperthermia. At nanoscale size regime, each magnetic particle becomes a single magnetic domain and shows superparamagnetic behaviour. Such NPs can have a high magnetic moment and can behave like a giant paramagnetic atom showing a fast response against applied magnetic fields with no remanence (residual magnetism) and coercivity (the field required to bring the magnetization to zero). These characteristics make these superparamagnetic metal oxide NPs very attractive for an extensive range of biomedical applications because they do not easily form agglomerations at room temperature. The use of these magnetic metal oxide NPs for biomedical applications, synthesis of high-quality NPs, in terms of size, crystalline phase and stoichiometry, is required. Iron oxide NPs (Fe_3O_4, γ-Fe_2O_3) are the most well studied metal oxide nanoparticle systems that are used for biomedical applications.

1.2. Magnetic nanoparticles (MNPs)

In recent years, magnetic nanoparticles (MNPs) have fascinated much attention due to their unique and tunable physio-chemical properties. The medical uses of magnetic particles have extended to different fields like cardiology, neurology, dentistry, oncology and radiology etc. Much attention has been paid to the synthesis of different kinds of MNPs due to their applications in healthcare, energy and environment. Industrial applications of MNPs cover a broad spectrum of magnetic recording media and biomedical applications, for example, biological separation, magnetic resonance contrast media and therapeutic agents in cancer treatments. Each

potential application of the MNPs requires different properties of the particles. In data storage applications, the particles need to have a stable, switchable magnetic state to represent bits of information that are not affected by temperature fluctuations. MNPs also have applications in spintronics. In the biomedical field, MNPs have been widely explored for MRI signal-enhancing applications [30]. Iron oxide NPs can modulate T_2-relaxation time of nearby water molecules, and can contrast the T_2-weighted MRI images. Another interesting application by magnetic NPs is for hyperthermia treatment of cancer [31]. When MNPs are exposed to alternating (ac) magnetic field, heat can be generated by the magnetic hysteresis loss, Néel-relaxation, and Brownian-relaxation losses. As a result, magnetic NPs can be a powerful local heat source that can destroy tumour cells [32]. This thesis is mainly focussed on MNPs, so their properties and applications are discussed in detail, in the proceeding sections.

1.2.1. Properties of magnetic nanoparticles

The behaviour of magnetic material depends on the structure of the material, mainly on its electronic configuration. Magnetic effects are caused by movements of the particles that have both mass and electric charges i.e. electrons, protons, and positive and negative ions. A spinning electric-charged particle creates a magnetic dipole, so called magneton. The orientations of the magnetic moments in a material are useful to recognize different forms of magnetism. If a magnetic field 'H' induces magnetisation 'M' in a material, the material is said to possess a magnetic susceptibility,

$$M = \chi_\text{v} H \quad .$$

.... (1.1)

where M and H are measured in units of Am^{-1}, where $1\ Am^{-1} = 4\pi/10^3\ Oe$ and χ_v is the volume susceptibility which is a dimensionless quantity. On a microscopic level the magnetism arises due to the presence of magnetic moments, a single unpaired electron has a moment of 1 μ_B (Bohr magneton), where $1\mu_B = 9.27402\times10^{-24}\ Am^2$. The magnetisation per unit mass, σ_m is magnetism divided by the mass of the sample, and so has units of Am^2kg^{-1}, note that $1\ Am^2kg^{-1} = 1\ emu.g^{-1}$.

Magnetic materials are classified based on their response to an externally applied magnetic field [33]. Most materials display either diamagnetic or paramagnetic behaviour in the presence of an applied field, depending on whether it possesses unpaired electrons or not. However, some materials display ordered magnetic states and are magnetic even in the absence of applied magnetic field and these are classified as ferromagnetic, ferrimagnetic and antiferromagnetic–prefix refers to the nature of the coupling interaction between the electrons within the material [33]. In diamagnetic materials, there are no unpaired electrons, so the induced magnetic moment is antiparallel to H resulting in very small and negative susceptibilities (-10^{-6} to -10^{-3}). They do not retain magnetic properties when the external field is removed. Paramagnetic materials have magnetic moments aligned parallel to H and susceptibilities of the order of 10^{-6} to 10^{-1}. While in ferri- and ferromagnetic materials, magnetic moments also align parallel to H, coupling interactions between the electrons of the material result in ordered magnetic states, i.e., magnetic domains, and large spontaneous magnetization. The susceptibilities of these materials depend on their atomic structures, temperature, and the external field H. At small sizes (of the order of tens of nm), ferri- or ferromagnetic materials, such as MNPs, become a single magnetic domain and therefore maintain one large

magnetic moment. Furthermore, the coupling interactions within these single magnetic domains result in much higher magnetic susceptibilities than paramagnetic materials [33-34]. The susceptibility in these ordered materials depends on temperature and applied magnetic field (H), which gives rise to the characteristic sigmoidal shape of the M-H curve, with M approaching saturation value at large values of H. Moreover, both ferromagnetic and ferrimagnetic materials exhibit a behaviour called hysteresis, meaning that they can retain a memory of an applied field after it has been removed. A typical magnetization (M) vs. magnetic field (H)) curve for ferromagnetic and superparamagnetic materials is shown in Fig. 1.1. Particle size is the deciding factor for the shapes of these curves. The hysteresis loop shows that the magnetization of ferromagnetic materials can increase with increasing applied field up to a point, called the saturation magnetization. However, when the field is removed, the magnetization is retained; even as the field is reduced to zero. This is called as remanence magnetization which is retained due to the hysteresis. To reduce the magnetization back to zero, some amount of magnetic field of opposite direction has to be applied; this field is termed as coercivity.

Domains, which are groups of spins all pointing in the same direction and acting cooperatively are separated by domain walls, which have a characteristic width and energy associated with their formation and existence. The motion of domain walls is a primary means of reversing magnetization. Experimental investigation of the dependence of coercivity on particle size showed behaviour similar to that schematically illustrated in Fig. 1.2. In large particles (micron sized or more) there is a multi-domain ground state that leads to a narrow hysteresis loop since it takes relatively little field energy to make the domain walls move. As we shrink the particle

size, a critical size is reached where domain walls can no longer be accommodated and the whole particle behaves as a single domain [36]. Single domain particles have broad hysteresis loops and the coercivity increases to a maximum and then decreases towards zero.
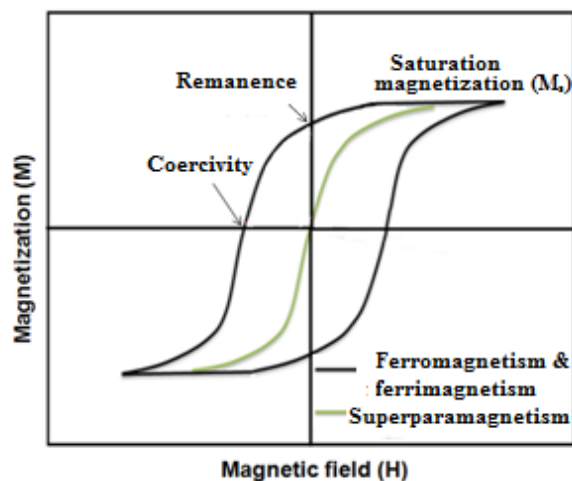
Fig. 1.1. *Magnetization vs. applied magnetic field representation for different classes of magnetism.*

When the size of single-domain particles further decreases below a critical diameter, the coercivity becomes zero and such particles are known as superparamagnetic particles [33]. In these particles, the thermal fluctuations are strong enough to spontaneously demagnetize a previously saturated assembly; therefore, these particles have zero coercivity and have no hysteresis. Superparamagnetism generally occurs in the nanometer size range. In the absence of the magnetic field, thermal energy causes magnetic moments of the superparamagnetic particles to fluctuate, resulting in zero net magnetic moment. NPs become magnetic in the presence of an external magnet, but revert to a nonmagnetic state when the external magnet is removed. This avoids 'active' behaviour of NPs in the absence of magnetic

field. Ferrite oxide-Fe_3O_4 (magnetite) is the most magnetic of all the naturally occurring minerals on earth and their superparamagnetic property, marked by the lack of remanant magnetization after removal of external fields, enables the particles to maintain their colloidal stability and avoid aggregation making it feasible for their use in biomedical applications.
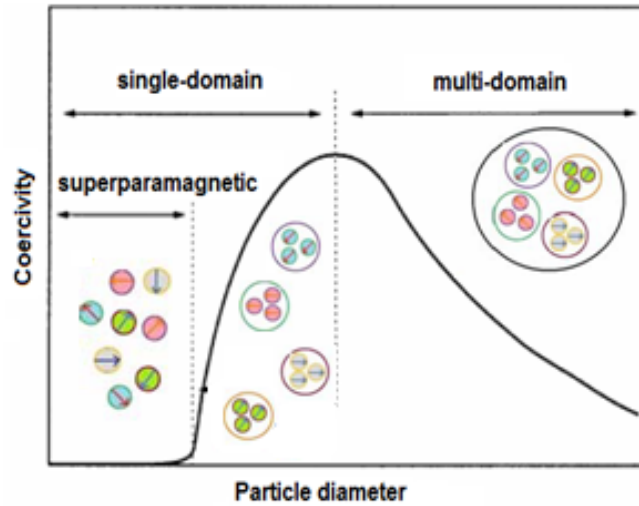
Fig. 1.2. Variation of coercivity with particle diameter.

1.2.2. Structure of Magnetite (Fe_3O_4)

Fe_3O_4 is a well-known ferrimagnetic material (in ferrimagnetic material, the iron ions are having opposing magnetic moments and the opposing moments are unequal and therefore a spontaneous magnetization remains). This happens when the material consist of different ions (such as Fe^{2+} and Fe^{3+}) that exhibits different magnetic properties depending on their particle size. It crystallizes in cubic inverse spinel structure (Fig. 1.3), where Fe^{3+} ions are filled in tetrahedral holes and Fe^{2+} and remaining Fe^{3+} randomly distributed in the octahedral holes [37].

In ferrimagnetic bulk Fe_3O_4, spontaneous magnetic domains occur where each individual domain contains its own magnetization direction and is separated from

other domains by domain walls. In the case of Fe_3O_4 nanoparticle, each particle behaves as a single domain, constraints are removed, and each single domain can spontaneously switch directions showing so called superparamagnetic behaviour. When an alternating magnetic field (AMF) is applied to these NPs, the particles undergo thermal fluctuations as the spins overcome their blocking energy barrier and flip with the alternating magnetic field [38]. The ability to produce heat from the thermal fluctuations makes Fe_3O_4 colloidal suspensions a good candidate for hyperthermia treatment of cancer [39]. This treatment works by directing the MNPs to the cancerous area and when a magnetic field is applied, the temperature of the cancerous area is raised to 42-43°C, resulting in the killing of the cancerous cells. Further, superparamagnetic Fe_3O_4 NPs exhibit a unique magnetic resonance contrast enhancement effect that enables non-invasive MR imaging of cell trafficking, gene expression and cancer.
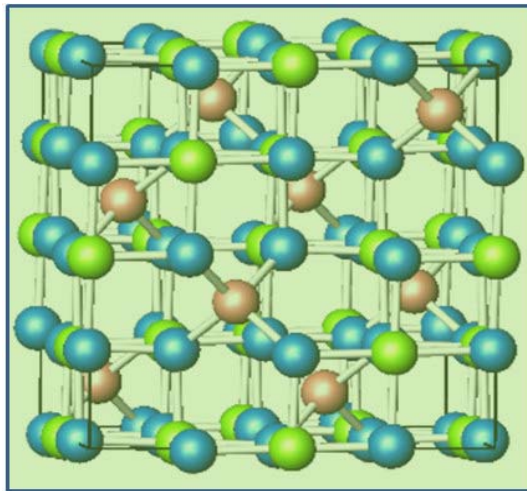
Fig. 1.3. *Inverse spinel structure of Fe_3O_4 (The blue atoms are O, the red atoms are Fe in tetrahedral site and the green atoms are Fe in octahedral site) [37].*

1.2.3. Synthesis of Fe₃O₄ MNPs

The synthesis of MNPs of controlled size has long been of scientific and technological interest. Stable suspensions of magnetic particles were first synthesized by Papell in 1964 [40]. There are many synthetic procedures reported in the literature for preparing nanosized crystalline magnetite. The sensitivity to reagent, stoichiometry and a large number of other reaction parameters often complicate the ability to obtain pure magnetite crystalline structures.

(a) Co-precipitation

Co-precipitation is a facile and convenient way to synthesize MNPs (metal oxides and ferrites) from aqueous salt solutions [41]. This is done by the addition of a base under inert atmosphere at room temperatures or at elevated temperature (Fig. 1.4). Complete precipitation should be expected at a pH levels between 8 and 14, with a stoichiometric ratio of 2:1 (Fe^{3+}/M^{2+}) in nitrogen environment [42-43]. The overall reaction may be written as:

$$M^{2+} + Fe^{3+} + 8OH^- \longrightarrow MFe_2O_4 + 4H_2O \qquad .... (1.2)$$
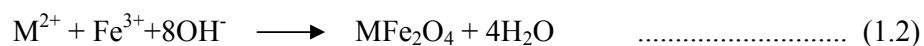
Where M can be Fe^{2+}, Mn^{2+}, Co^{2+}, Cu^{2+}, Mg^{2+}, Zn^{2+} and Ni^{2+}etc. The size, shape and composition of the MNPs dependent on many factors like the type of salts used (*e.g.* chlorides, sulphates, nitrates), M^{2+}/Fe^{3+} ratio, temperature of the reaction, pH of the reaction medium, type of base used, kinetics of the reaction, ionic strength of the media, addition sequence of reactants and bubbling of nitrogen gas during the course of reaction. In the synthesis of Fe_3O_4, precipitation at lower temperature (<60°C) produces an amorphous hydrated oxyhydroxide that can be easily converted to Fe_2O_3, while higher reaction temperatures (>80°C) favour the formation of Fe_3O_4 [44-45].

The suitable pH (basic pH) for the rapid formation of Fe_3O_4 can be attained by the addition of excess base. Hong et al. [46] observed that when Fe_3O_4 NPs precipitated using NH_4OH instead of NaOH, highly crystalline, higher saturation magnetization and narrow size distribution can be obtained. Nitrogen gases bubbling through the solution not only protects against critical oxidation of the magnetite NPs but also reduces the particle size when compared to methods without oxygen removal [47-48]. In the presence of oxygen, Fe_3O_4 formed may be oxidized to $Fe(OH)_3$

$$4\ Fe_3O_4 + O_2 + 18\ H_2O \longrightarrow 12\ Fe(OH)_3 \qquad \text{............................ (1.3)}$$
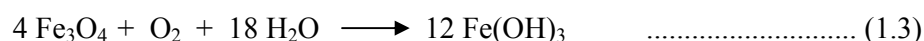
In order to prevent possible oxidation and aggregation, Fe_3O_4 NPs are usually coated with organic or inorganic molecules during the precipitation process. Co-precipitation is the preferred route of synthesis because of the simplicity of the method. In this method, the reaction temperature and time are lower as compared to other methods such as thermal decomposition and hydrothermal. Also, solvent is environmental friendly (water) besides the reaction yield is high and scalable.
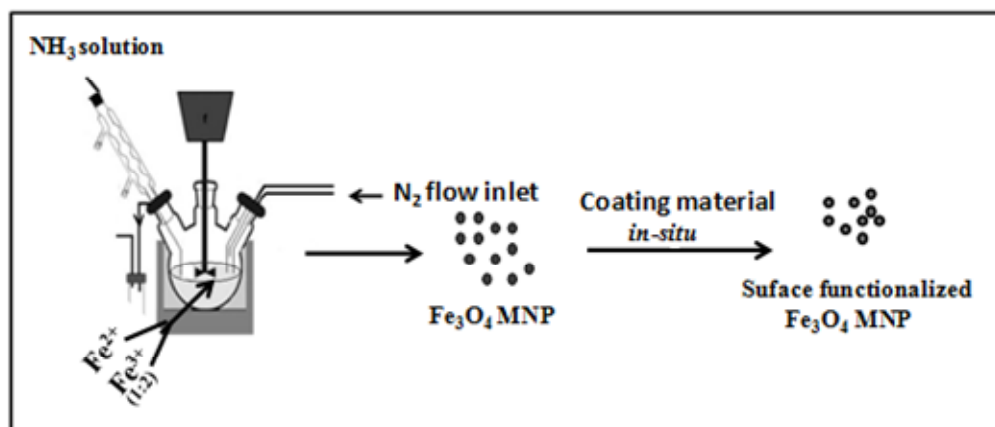
Fig. 1.4. *Schematic representation of synthesis of MNPs by co-precipitation followed by their surface functionalization.*

This is a convenient and cheap method used to prepare well dispersed (water-base) Fe_3O_4 nanoparticles. It also suggests a low-temperature alternative to conventional powder synthesis techniques in the production of NPs [49-51]. Chemical co-precipitation can produce fine, high-purity, stoichiometric particles of single and multi- component metal oxides. Furthermore, if process conditions such as pH of the reaction medium, reaction temperature, stirring rate, solute concentration and surfactant concentration are carefully controlled, oxide particles of the desired shape and sizes can be produced.

(b) Thermal decomposition

This is a non-aqueous method of synthesis involving decomposition of metal salt or precursors at high temperature in high-boiling organic solvent. NPs can be synthesized by high temperature decomposition of organometallic precursors, such as $Fe(CO)_5$, $Mn(CO)_5$, and salts such as $FeCl_2$, $MnSO_4$,$CoCl_2$ and $Fe(acac)_3$ (acac = acetylacetonate) [52-53], $M^x(cup)_x$ (cup= N-nitrosophenylhydroxylamine) or carbonyls (such as $Fe(CO)_5$) using organic solvents and surfactants such as fatty acids, oleic acid and hexadecylamine [2, 54]. A better control on particle size distribution is possible in this method. Principally the size and morphology of MNPs (monodispersity) depends on the ratios of the starting reagents including organometallic compounds, surfactants, solvents [55], reaction temperature and time etc. The stabilizers used are usually long chain fatty acid with at least one functional group. This functional group, either a carboxylic acid or an amine group, usually bound to the nanoparticle surface is not available for conjugation. Fatty acids such as oleic acid, steric acid and lauric acid have been used as stabilizer molecules. The NPs resulting from this procedure are stable in non-polar solvents (such as hexane or

cyclohexane) and capped with non-polar end-groups on their surface. The capping molecules (also called ligands) are typically long-chain alkanes with polar groups that bind to the NPs surface.

Hydrophobic Fe_3O_4 MNPs were also prepared by using high temperature thermal decomposition of iron (III) acetylacetonate, $Fe(acac)_3$, with 1,2 dodecanediol in the presence of lauric acid [56]. Dibenzyl ether was used as a solvent and dodecyl amine was used to make monodisperse and highly crystalline magnetite particles under 20 nm with high magnetization (Fig.1.5). This method can also be used for the preparation of mixed ferrite (MFe_2O_4) NPs where M is a divalent metal ion.
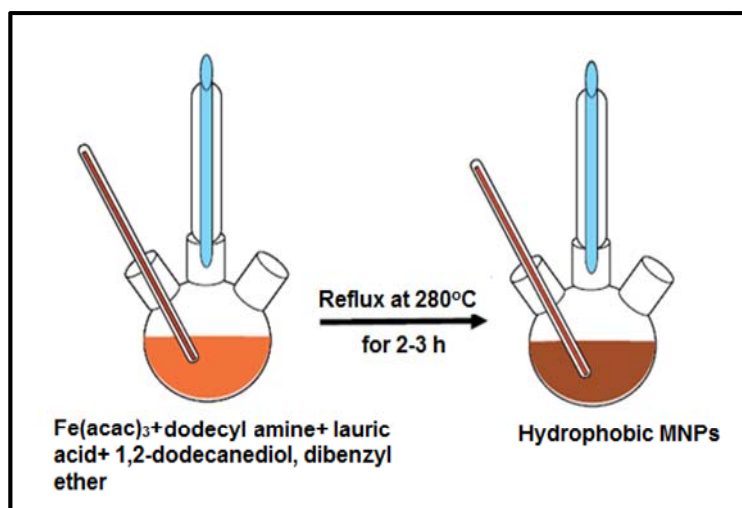
Fig. 1.5. *Synthesis of hydrophobic Fe_3O_4 by thermal decomposition method.*

Highly monodisperse particles can be obtained using this decomposition method. NPs synthesized by this method are soluble in a variety of hydrophobic or non-polar solvents. However, for use in biomedical applications, these NPs have to be subjected to surface modification techniques to convert them to hydrophilic nanoparticles.

(c) Ultrasonication

This method has been extensively used for the fabrication of novel materials with unique properties. The physiochemical effects of ultrasound waves arise from acoustic cavitation, which comes from the formation, growth and implosive collapsing of bubbles in the liquid. The implosive collapsing of the bubbles generate a localized hotspot through adiabatic compression or shock wave formation within the gas phase of the collapsing bubble. Very extreme conditions i.e. temperature of ~5000 K and pressure upto ~1800 atm were beneficial for the formation of highly monodispersive NPs [57]. Kim et al. [58] synthesized Fe_3O_4 NPs by the use of sonochemical and co-precipitation methods. The crystallinity and magnetic properties of the obtained particles by the use of the two methods were compared and it was found that magnetic particles obtained by sonochemical method had a higher crystallinity and saturation magnetization as compared to the particles obtained from the co-precipitation method.

(d) Hydrothermal synthesis

Hydrothermal processing method for the synthesis of MNPs is also called solvothermal method. It comprises aqueous reactions usually carried out by using autoclaves at high pressure over 2000 psi and at high temperature of more than 200°C. In this process, the reaction conditions of precursor material, solvent, temperature, pH and time have important effect on the product and phase purity of the nanoparticles. Wang et al. [59] used a hydrothermal method to synthesize Fe_3O_4 powder. They found that the nanoscale Fe_3O_4 powder (40 nm) can be obtained at 140°C for 6 h having a saturation magnetization of 85.8 emu g^{-1}, this is a little lower than that of the corresponding bulk Fe_3O_4 (92 emu g^{-1}). There are two main routes for the formation of ferrites via hydrothermal conditions: hydrolysis followed by oxidation and second

is neutralisation of mixed metal hydroxides. Although hydrothermal technique is very versatile, one of the main drawbacks of this method is the slow reaction kinetics. Microwave heating can be used to increase the kinetics of crystallization during the hydrothermal synthesis [60]. Such a combination is termed as microwave-hydrothermal method. The increase in the reaction kinetics (up to two orders of magnitude) is due to the localized super heating of the solution.

Other methods that exist for the controlled synthesis of Fe_3O_4 MNPs include reverse micelle method, arc discharge, mechanical grinding, sol-gel method, spray pyrolysis [61], layer–by–layer deposition [62] and laser pyrolysis [63] etc.

1.2.4. Surface functionalization of MNPs

Superparamagnetic NPs have been extensively used for numerous *in-vitro* and *in-vivo* applications. These NPs showed high magnetization values with narrow size distribution. The advantages of the NPs are mainly due to their nanoscale size and large surface area with the ability to get functionalized with targeting ligands, therapeutic moieties and biomolecules [64]. The fact that the size of the NPs is quite similar or smaller to the size range of several bio entities, makes them a natural companion in the hybrid system. Furthermore, NPs can easily gain access to various areas of the body without interfering into normal functions and has the required potential for diagnostic and therapeutic applications. Surface modification of MNPs is important to render them not only non-toxic, biocompatible, water solubility, but chemically functional, and thus allow a targetable delivery with particle localization in a specific area. Higher effective surface area of NPs facilitates easy attachment of ligands, lower sedimentation rates (high stability in colloidal suspension) and improved tissue penetration. For most of the therapeutic applications, the first

significant challenge is to avoid undesirable uptake of NPs by the reticulo-endothelial system (RES). The next step is to achieve site-specific targeting for *in-vivo* studies. Small sized NPs are having higher diffusion rates resulting in increasing the concentration of NPs at the centre of a blood vessel. Due to this, the interactions of NPs with endothelial cells get limited and blood circulation time of NPs is increased [65]. The surface functionalization and colloidal stability of NPs depend upon their zeta-potential. High positive and negative zeta-potential of NPs indicates their colloidal stability due to electrostatic interaction. After synthesis, the unmodified MNPs are stable in different pH solutions but the *in-vivo* application of these MNPs requires that their surface should be coated with biodegradable matrices. The fate of NPs depends on the type of coating material used for the surface modification. Hydrophilic coating prevents interaction of NPs with macrophages of RES, resulting in the reduction of their elimination from the blood circulation, and increase in their circulation half-life [66]. MNPs may be stabilized either during their synthesis (*in-situ*) or in a post-synthesis process. Reduced agglomeration of NPs during the synthesis is the major advantage of in situ modification [67]. These biocompatible coatings stabilize the NPs and provides accessible surface for routine conjugation of biomolecules. Various organic and inorganic molecules were used for surface functionalization of MNPs.

(a) Organic stabilizers

(i) Macromolecules:

Many polymeric molecules have been employed for steric stabilization of oxide NPs in aqueous and high ionic strength media [68]. The polymer shell enhances the stability of NPs in solution and permits the encapsulation of a therapeutic agent i.e.

drug. Surface properties of NPs such as surface charge, chemical functionality or their thermo-sensitive properties can be modified using these stabilizers. The performance of nanocarriers is influenced by the chemical nature of the polymer (i.e., hydrophilicity/ hydrophobicity, biocompatibility and biodegradation), the molecular weight of the polymer, the manner in which the polymer is grafted or attached (i.e., physically or chemically), the conformation of the polymer and the degree of particle surface coverage. Among various macromolecules, dextran, polyethylene glycol (PEG), chitosan and polyvinyl pyrollidone are known to be highly biocompatible and enhance the monodispersity of MNPs in aqueous medium. Dextran has been used for surface modification because of its favourable size (chain length) and biocompatibility, which enables optimum polar interactions (mainly chelation and hydrogen bonding). Dextran coating provides narrow size distribution along with retention of superparamagnetic behaviour of MNPs [69-70]. Pradhan et al. [71] fabricated dextran coated Fe_3O_4 NPs by co-precipitation method, and compared their *in-vitro* cytocompatibility and cellular interactions with mouse fibroblast and human cervical carcinoma cell lines with lauric acid-coated Fe_3O_4 nanoparticles. The surface modification was found to play a significant role in modulating biocompatibility and cellular interaction of MNPs.

PEG is used in targeted drug delivery system because it is non-toxic, non-immunogenic and non-antigenic. It is coated on the NPs surface to disperse it, to reduce the non-specific protein adsorption and clearance by macrophages and to render the NPs capable of crossing the cell membrane. PEG has a general structure of $HO\text{-}(CH_2CH_2O)_nH$, encompassing a polyether backbone that is chemically inert with terminal hydroxyl groups. PEG prevents the NPs from agglomeration, prevent particle

surface from oxidation and make them more biocompatible. Further, dendrimers were also used to stabilize Fe_3O_4 NPs [78]. For example, Chandra et al. [79] prepared dendrimers coated Fe_3O_4 NPs for drug delivery application.

Chitosan is a polyaminosaccharide with significant biological (biodegradable, biocompatible and bioactive) and chemical (polycationic, contains reactive groups such as –OH and –NH) properties. It can be prepared by the partial N-deacetylation of the chitin (a natural biopolymer derived from the shells of the crustaceans like crabs, lobsters etc.). It consists of repeated units of glucosamine and N-acetyl glucosamine. Chitosan shows mucoadhesive, immunostimulating, antimicrobial and wound healing properties etc. Chitosan is prone to chemical and physical modifications and it also shows pH and temperature responsive behaviour. Hence, chitosan has attracted a great deal of attention as a functional biopolymer for a wide variety of applications, especially in pharmaceutics, food and cosmetics [80]. For decades chitosan and its derivatives have been used to form polymeric NPs through electrostatic complexation with nucleic acids and various pharmaceutical formulations [81], only recently being used in combination with magnetic nanoparticles. Bhattarai et al. loaded chitosan-coated iron oxide NPs with anionic adenovirus vectors through electrostatic interactions [82-83]. These iron oxide NPs were used to enhance gene transfection. In addition to its bioadsorptive properties, chitosan possesses both amino and hydroxyl functional groups, which can be used for MNPs functionalization with targeting, imaging and therapeutic agents.

(ii) Small molecules:

The small molecules are primarily attractive for stabilizing MNPs due to their ease of preparation and simple conjugation chemistry. There is limitation of the

binding of large surfactant molecules or long polymer chains to NPs due to steric hindrances, which could be compensated by using small molecules having multiple functional groups such as carboxyl (COOH), amine (NH_2), thiol (SH), phosphate and sulfates. The presence of large number of functional groups on the surface of NPs facilitates the binding of various biomolecules as well as drugs. Thus, the stability of the bonding between functional molecules and NPs is crucial for therapeutic applications. Among various small molecules, citrate moiety having multiple carboxylate functionalities has been extensively used for the colloidal stability of nanoparticles. The functional groups are chemisorbed on the surface of NPs by coordinating via one or two of the carboxylate functionalities, depending upon size and shape of the particles and leaving at least one carboxylic acid group free exposed to the solvent. The free carboxylic group provide sufficient negative charge on the particles surface and hence, make them hydrophilic [84]. The short chain amines and aminosilanes are commonly used as stabilizing agent in fabrication of various magnetic nanoparticles. Recently, Barick et al. [85] demonstrated a single step facile approach for highly water-stable assembly of amine-functionalized Fe_3O_4 NPs using thermal decomposition of Fe-chloride precursors in ethylene glycol medium in the presence of sodium acetate and ethylenediamine for bioapplications and compared their magnetic resonance (MR) contrast behaviour. Small molecules having thiol (SH) functionality also gained great deal of attention due to their higher binding affinity towards metal and metal oxide NPs. The organosulfur compound, 2, 3-meso dimercapto succinic acid (DMSA) [56] having two carboxylic and two thiol groups have been commonly used as a stabilizing agent for inorganic oxides.

(b) Inorganic stabilizers

Silica (SiO$_2$), gold (Au) and silver (Ag) are generally used for surface engineering of the MNPs which forms core–shell structures, and provides stability to the NPs in solution and further help in binding various biological molecules and drugs to the surface of NPs through suitable functional groups. Silica has been employed as a coating material for MNPs due to their non-toxic nature, water solubility and chemical stability at high temperature. Easily functionalizable surface of silica provides protection against chemical degradation of the magnetic core and prevent the release of potentially toxic components of the core. In addition, silanol groups on the surface of silica can be easily derivatized to introduce different biomolecules. The stabilization of iron oxide NPs by silica can easily be achieved either by Stöber process or microemulsion method [86-87]. SiO$_2$ stabilized Fe$_3$O$_4$ core–shell NPs functionalized with phosphorescent iridium-complex has been used for applications in photodynamic therapy [88]. Iron oxide NPs synthesized by co-precipitation method can be directly coated with silica by mixing the NPs in water with 2-propanol, 30% aqueous ammonia, and silanization agent tetraethoxyorthosilane (TEOS). The formation of bare silica NPs can be prevented and control on thickness of silica shell can be regulated by the ratio of TEOS to water. Reverse micelle method can also be used to coat the surface of NPs with silica. This method can be used for both, simultaneous (*in-situ*) formation of silica coating on nanoparticle as it is being synthesized or form silica coating on premade nanoparticles.

There has been significant interest in stabilizing iron oxide NPs with noble metal shells such as Au and Ag. The magnetic oxide NPs with metal coating can be effectively stabilized in corrosive biological conditions and can be readily

functionalized through the well-established metal-sulfur chemistry. The magnetic core–shell NPs with tunable plasmonic properties have great potential for nanoparticle-based diagnostic and therapeutic applications. Dumbbell shaped Au–Fe_3O_4 NPs with controlled plasmonic and magnetic properties were reported to act as target-specific nanocarriers to deliver cisplatin into Her2-positive breast cancer cells with strong therapeutic effects [89-90]. The control on shell thickness allows the tuning of plasmonic properties of the core-shell NPs to be either red shifted (to 560 nm) or blue shifted (to 501 nm). When compared to conventional bare iron oxide NPs, the Au–Fe_3O_4 NPs were useful in facilitating stepwise attachment of an antibody to a plastin complex and also for serving as optical and magnetic probe for locating the drug in the cells. Zhong et al. demonstrated that the magnetically active iron oxide core and thiolate-active Au shell is a suitable candidate for exploiting the Au surface protein-binding reactivity for bioassay and the iron oxide core magnetism for magnetic bioseparation [91]. Thus, the combination of magnetism, selectivity and stability displayed in gold-coated iron oxide particles makes it very promising in applications such as magnetic separation, controlled release and targeted drug delivery. The most significant advantage of this composite system is that it provides controlled magneto-optical properties, long term stability to the magnetic core and functionality to the NPs.

1.2.5. Applications of MNPs

For biomedical applications, surface functionalized MNPs having superparamagnetic behaviour (no remanence along with a rapidly changing magnetic state) at room temperature are desirable. Biomedical applications are commonly divided into two major categories: *in-vivo* and *in-vitro* applications. *In-vivo*

applications could be further separated in therapeutic (hyperthermia and drug-delivery) and diagnostic applications (magnetic resonance imaging, MRI), while for *in-vitro* applications the main use is in diagnostic (separation/selection, and magnetorelaxometry). The most important requirement for the use of these MNPs for *in-vivo* biomedical applications is the biocompatibility and the non-toxic nature of the magnetic components with respect to biosystems. In this section, an overview of the biomedical applications of MNPs is discussed.

(a) Hyperthermia

Regarding the cancer therapy, the term "hyperthermia" is used for the treatment based on generation of heat at the tumour site and that heat will be used for the killing of the cancerous cells [92]. In this approach, the temperature of local surroundings of a tumour site is increased and due to this, the physiology and the structure of diseased cells are changed. Hyperthermia treatment is always used with other treatments including chemotherapy, radiation therapy, gene therapy, surgery and immunotherapy for cancer [93]. Hyperthermia may make some cancer cells more sensitive to radiation or harm other cancer cells that radiation cannot damage. When hyperthermia and radiation therapy are combined, they are often given within an hour of each other. It can also enhance the effects of certain anticancer drugs.

The efficacy of hyperthermia treatment significantly depends on the heat generated at the targeted site of action, duration of treatment and cell and tissue characteristics [94]. The temperature of the tumour and the surrounding tissue is monitored constantly during hyperthermia treatment by injecting small tubes with tiny thermometers into the treatment area, to ensure that the temperature of the site should not exceed the desired temperature. Imaging techniques, such as CT (computed

tomography), may be used to make sure the probes are correctly placed [93]. Hyperthermia can be categorized into local, regional and whole body hyperthermia depending on the site of application. Local hyperthermia involves application of heat only to a small area of interest such as a tumour. Regional hyperthermia involves heat subjection to larger areas such as whole tissue, body cavity, limb or organ. Whole body hyperthermia is applied to treat metastatic cancer cells that have spread throughout the body. The challenge here is to heat only the tumour cells without damaging the healthy tissues. Out of these, local hyperthermia is gaining much more attention due to intracellular heat subjection within specified region of interest [95]. Hyperthermia treatment can be administered by different techniques like ultrasound, radiofrequency, microwaves, infrared radiation, magnetically excitable thermoseeds, and tubes with hot water. Some of the challenges in traditional hyperthermia treatment are: 1) unavoidable heating of healthy tissue resulting in burns, blisters and discomfort, 2) limited penetration of heat into body tissues by microwave, laser and ultrasound energy, and 3) insufficient thermal dosage in the target region. With the possibility to convert dissipated magnetic energy into thermal energy, the application of magnetic materials for hyperthermia treatment of cancer was first proposed in 1957 [96]. MNPs based hyperthermia treatment is used for the suppression of cancer cells using AMF. When MNPs are subjected to alternating magnetic field, heat is generated through the hysteresis and relaxation loss processes. The amount of heat produced depends on the physical properties of the magnetic material and magnetic field parameters. Cancer cells are destroyed at elevated temperatures (42-43°C), whereas normal cells can survive at these temperatures. The architecture of the vasculature in solid tumours is chaotic, resulting in regions with hypoxia and low pH, which is not

found in normal tissues in undisturbed conditions. These environmental factors make cancer cells more sensitive to hyperthermia [97]. The advantage of magnetic hyperthermia is that it allows the heating to be restricted to the tumour area, i.e. localized heating is possible. Moreover, the use of subdomain magnetic particles (nm-sized) is preferred instead of multidomain (micron-sized) particles because NPs (high surface to volume ratio) absorb much more power at tolerable AC magnetic fields [98]. MNPs interact with oscillating magnetic field to generate heat through various mechanisms.

(i) Mechanism of hyperthermia by MNPs

In order to find the suitable materials for the hyperthermia, the knowledge and understanding of the heating mechanism is essential. The absorption efficiency of any material to generate heat due to AMF is measured in terms of specific absorption rate (SAR). SAR is generally used to define the transformation of magnetic energy into thermal energy (heat) [99]. For a majority of applications, it is desirable to have higher temperature enhancement rates and MNPs are good candidates for such applications due to their efficiency in conversion of magnetic energy into heat even at low concentration of particles [100].

For MNPs based hyperthermia, a general mechanism involves distribution of particles throughout the targeted tumour site, followed by generation of heat to the tumour using an AMF. The dynamic response of a dipole with its magnetic moment in a single direction due to an external AMF during the transformation of magnetic energy into heat is mainly governed by thermal fluctuations that occur in a particle. The heat generation mechanism can be attributed to two different phenomena: relaxation and hysteresis loss. The relaxation is of two types: Néel and Brownian

relaxations. Heat generation through Néel relaxation is due to rapidly occurring changes in the direction of magnetic moments relative to crystal lattice (internal dynamics). Brownian relaxation is due to physical rotation of particles within a medium in which they are placed (external dynamics) and is hindered by the viscosity that tend to counter the movement of particles in the medium [101]. The Néel and Brownian relaxation times are given by the following equations:

$$\tau_B = \frac{4\pi\eta R_H^{\ 3}}{k_B T} \qquad\qquad \text{...................... (1.4)}$$

$$\tau_N = \tau_0 e^{KV_M/k_B T} \qquad\qquad \text{...................... (1.5)}$$

$$\tau_{eff} = \frac{\tau_N \tau_B}{\tau_N + \tau_B} \qquad\qquad \text{...................... (1.6)}$$

where τ_B is the Brownian relaxation time, τ_N is the Néel relaxation time, τ_0 is the length of time which is a characteristic of material (in this case, $\tau_0 \approx 10^{-9}$ s), K is the anisotropy constant, V_M is the volume of the Fe_3O_4 nanoparticle, k_B is Boltzmann's constant, T is temperature, η is the viscosity and R_H is the hydrodynamic particle radius.

The internal (Néel) and external (Brownian) sources of friction that lead to a phase lag between applied magnetic field and the direction of the magnetic moments tends to generate thermal losses. By using linear response models with known Néel and Brownian relaxation times, SAR for MNPs can be easily calculated [102]. SAR increases with frequency of AMF and is proportional to the square of magnetic field intensity. SAR are expressed in terms of rise in temperature per unit time and per

gram of magnetic material, multiplied by calorific capacity of a sample. The SAR can be calculated as follows:

$$SAR = C \frac{dT}{dt} \frac{1}{m_{Fe}} \qquad . \qquad \text{........................ (1.7)}$$

where C is the specific heat of solvent (C = C_{water}= 4.18 J/g C), dT/dt is the initial slope of the time-dependent temperature curve and m_{Fe} is mass fraction of Fe in the sample.

Generally SAR values depend on parameters such as MNPs structure (size, shape and crystal structure), magnetic properties (magnetic anisotropy and temperature dependence of magnetizations), and amplitude (H) and frequency (f) of AMF [98, 103]. Decrease in SAR values with polydispersity of MNPs is due to the decrease in the proportion of particles contributing to total heat generation. The heating power of many MNPs also change with surrounding environment e.g. for those particles internalized within the cells. In such cases, intracellular components generally hinder the movement of the particles resulting in total heat contribution largely coming only from Néel relaxation. Therefore, for intracellular hyperthermia, Néel relaxation is the major contributor for heat release [104].

Hayashi et al. [105] synthesized cysteine-modified Fe_3O_4 MNPs (Cys-Fe_3O_4 NPs) by one-pot biofunctionalization of allyl-functionalized Fe_3O_4 NPs (allyl-Fe_3O_4) with cysteine using *in-situ* hydrolysis-condensation of iron (III) allylacetylacetonate and thiol-ene click reaction. They investigated the hyperthermic properties of Cys-Fe_3O_4 NPs (10 mg/mL) in agar phantom. The phantom was exposed to an AC magnetic field with a frequency of 230 kHz and field amplitude of 100 Oe. They found that the temperature of Cys-Fe_3O_4 NPs containing phantom increased from 37

to 44°C, by applying the field for 15 minutes (Fig. 1.6). SAR value of Cys-Fe_3O_4 NPs was found to be 156 W/g. The SAR values were 171W/g at 750 kHz and 63 Oe field amplitude and 841 W/g at 750 kHz and 126 Oe.
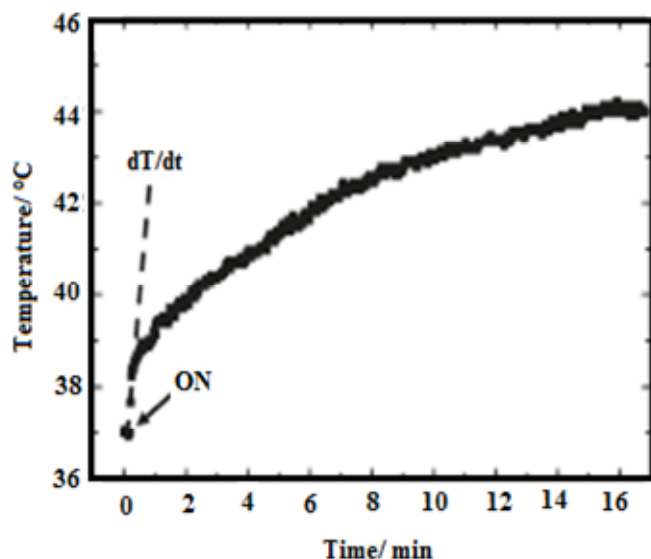
Fig. 1.6. *Temperature increase of Cys-Fe$_3$O$_4$ NPs by applying an AC magnetic field 230 kHz in frequency and 100 Oe in field amplitude [105].*

Shete et al. [106] prepared Fe_3O_4 NPs using ferrous chloride as the sole precursor. The as-prepared Fe_3O_4 NPs were further coated with amphiphilic chitosan (CH). Physically adsorbed CH was then cross-linked using glutaraldehyde (GLD). Fe_3O_4 NPs and CH-coated Fe_3O_4 NPs (Fe_3O_4–CH/GLD) were investigated for their structural, morphological and magnetic characterizations. NPs show superparamagnetic behaviour at room temperature with saturation magnetization values for bare and coated NPs were 51.68 emu/g and 48.60 emu/g, respectively. They demonstrated experimentally that the hyperthermic effect of Fe_3O_4 NPs enhances dramatically after functionalization with CH/GLD. The coating prevents the aggregation of Fe_3O_4 which makes colloidal stable suspension of CH/GLD

functionalized NPs in water as compared to bare Fe_3O_4, which increases the hyperthermic effect through Brownian and Neel's spin relaxations. Fig. 1.8 represents the temperature kinetic curves obtained after application of AC magnetic field on both samples dispersed in water with concentration of 2 mg/mL. Temperature kinetic curves (Fig. 1.7) signify that rise in temperature is dependent on the magnetic field strength for both samples.
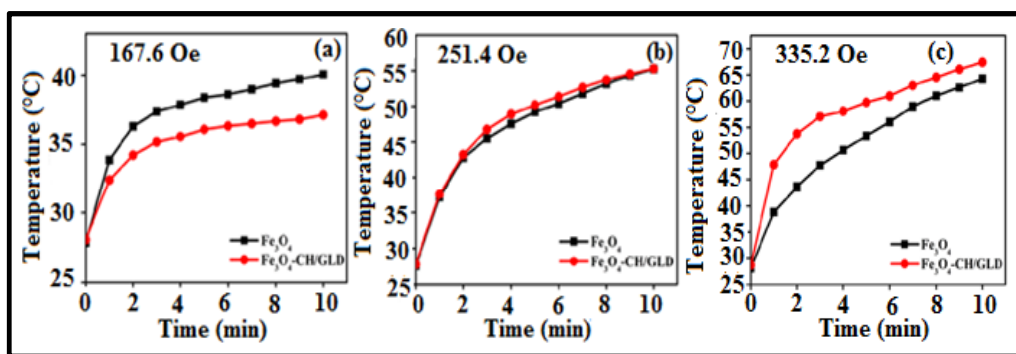
Fig. 1.7. *(a)–(c) Temperature kinetic curves obtained after application of AC magnetic field on both the samples dispersed in water with a concentration of 2 mg/mL. [106].*

(b) Nanoparticles as carrier for drug delivery

In addition to the inherent hyperthermia properties of MNPs, they offer new avenues as a carrier for other drugs. Drug delivery is the phenomenon of administering a pharmaceutical compound (or drug) to achieve a therapeutic effect in humans or animals. Drug delivery technologies modify drug release profile, absorption, distribution and elimination for the benefit of improving product efficiency, as well as patient convenience and compliance. Drug can be released via diffusion, degradation, swelling and affinity-based mechanisms. Targeted drug

delivery (sometimes called smart drug delivery) is a process of delivering drug to a patient in a manner that increases the concentration of the drug in some parts of the body relative to others. The objective of a targeted drug delivery system is to prolong, localize, target and have a protected drug interaction with the diseased tissue. The benefits to the targeted release system is the reduction in the frequency of the dosages taken by the patient, having a more uniform effect of the drug, reduction of drug side effects and reduced fluctuation in circulating drug levels.

Delivering therapeutic compound to the target site is a major problem in treatment of many diseases. A conventional drug application is characterized by limited effectiveness, poor biodistribution, and lack of selectivity [107]. These limitations and drawbacks can be overwhelmed by controlled and targeted drug delivery. In controlled drug delivery systems, the drug is transported to the place of interest and undesirable side effects can be minimized. In addition, these delivery systems protect the drug from rapid degradation or clearance and enhance drug concentration in target tissues; therefore, lower doses of drug are needed [108].

(i) Characteristics of drug delivery carriers

A successful drug delivery carrier must satisfy a number of properties so that it is compatible with the biological system and deliver the material of interest. Some of the important characteristics of an ideal drug delivery vehicle that should be considered while designing the carrier are:

- drug loading capacity
- triggered (or appropriate) release of drug according to proper kinetics
- serum/plasma stability and non-toxic in nature
- optimized biocirculation (stealth)

> ➤ targeted drug delivery, non–immunogenic

> ➤ cell uptake and non-accumulative

Cell-specific targeting can be achieved by attaching drugs to the nanocarriers. Nanocarriers with optimized physicochemical and biological properties are taken up by cells more easily than larger molecules, so they can be successfully used as delivery vehicles for currently available bioactive compounds. The way of conjugating the drug to the nanocarrier and the strategy used for its targeting is very crucial for targeted therapy.

Nanoparticulate drug delivery systems have many advantages for cancer therapy over free drug administration. With reference to cancer therapeutics, some of the demonstrated advantages of nanoparticulate delivery system are:

➤ increased drug concentration in the tumour tissue through passive and active targeting;

➤ reduction of the drug concentration and toxic side effects in normal cells;

➤ improved drug stability by reducing its degradation in the systemic circulation;

➤ improvement in the cellular internalization and organelle-specific delivery of the loaded drug that results from adoption of various surface functionalization strategies.

Liposomes, solid lipid nanoparticles, dendrimers, polymers, silicon or carbon materials, and MNPs are the examples of nanocarriers that have been tested as drug delivery systems. Amongst the various nanocarriers, MNPs display a wide variety of characteristics, which make them potential candidates for drug delivery. Attachment of a drug with MNPs may be achieved by covalent bonding [109-110], electrostatic interactions [110], adsorption [111], or encapsulation process [112].

The drug-loading efficiency of citric acid functionalized Fe_3O_4 nanoparticles (CA-MNP) was investigated by Nigam et al. [113] using doxorubicin hydrochloride (DOX) as a model drug to evaluate their potential as a carrier system. They discussed about the method for entrapment of positively charged drugs (DOX) onto the surface of negatively charged CA-MNP (negative charge is due to the presence of carboxylate ions on the surface) through electrostatic interactions and suggested that bound DOX molecules will be released in appreciable amounts in the mild acidic (pH=5) environments of the tumours. Thus, CA-MNP can be used as a potential carrier for effective magnetic drug targeting and hyperthermia treatment of cancer (Fig. 1.8) Further, the citrate groups on Fe_3O_4 surface can provide accessible surface for conjugation of biomolecules through bioconjugation chemistry for magnetic biolabeling, efficient bioseparation and contrast enhancement for MRI etc.
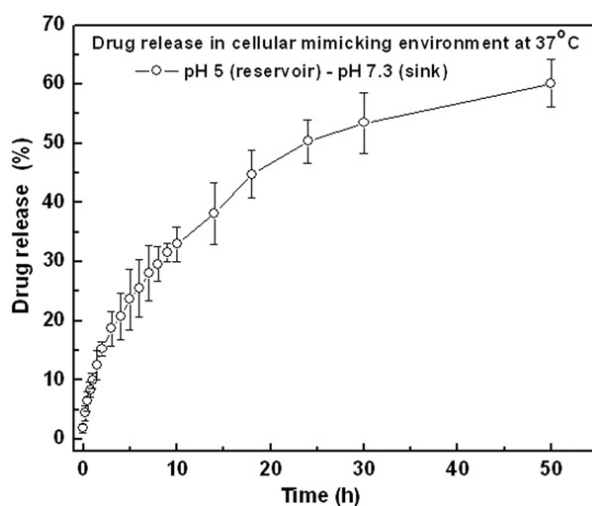
Fig. 1.8. Drug release profile of DOX loaded CA-MNP in cell mimicking environment [113].

Guo et al. [114] synthesized monodisperse superparamagnetic single crystal magnetite NPs with mesoporous structure, by solvothermal method. This method has

many advantages including simplicity of the method, high quality product, large scale production and good reproducibility. They have reported high magnetization of sample (65 emu/g) and the obtained Fe_3O_4 NPs could be easily functionalized with $-COO^-$ group and silica. Furthermore, they have investigated the drug (DOX) loading and release behaviours of this mesoporous structure. They found that DOX molecules could be stored in the mesoporous structure with an uptake efficiency of 40 mg/g (Fig. 1.9). The incorporated drugs in the MNPs get released to the solution within 12 h.
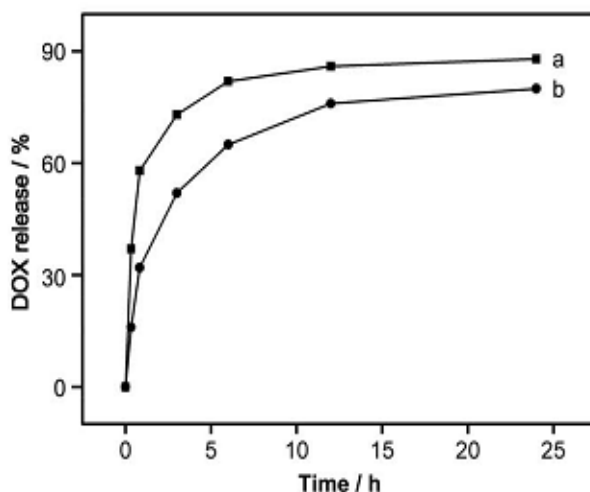
Fig. 1.9. *Drug-release profiles for DOX@Fe$_3$O$_4$ measured at (a) pH=5 in acetate buffer and at (b) pH=7.5in PBS buffer [114].*

Yang et al. [115] have designed, synthesized and characterized Cyclo (Arg-Gly-Asp) (cRGD)-functionalized, DOX-conjugated and ^{64}Cu-labeled superparamagnetic iron oxide (SPIO) nanoparticles for tumour-targeted drug delivery and PET/MR imaging. These SPIO nanocarriers had a hydrodynamic diameter of 68 ± 2 nm and exhibited pH=sensitive drug release behaviour (Fig. 1.10). Flow cytometry and CLSM analysis show that cRGD-conjugated SPIO nanocarriers exhibited higher cellular uptake leading to higher cytotoxicity. cRGD-conjugated SPIO nanocarriers also had a

much higher level of tumour accumulation compared to cRGD-free SPIO nanocarriers according to *in-vivo* PET imaging and biodistribution analyses. The MRI r_2 relaxivity of the SPIO nanocarriers were also measured which was similar to that of the Feridex, an FDA approved SPIO-based MRI contrast agent. These multifunctional SPIO nanocarriers were shown as potential for combined tumour-targeting drug delivery and PET/MR imaging thereby making cancer theranostics possible.
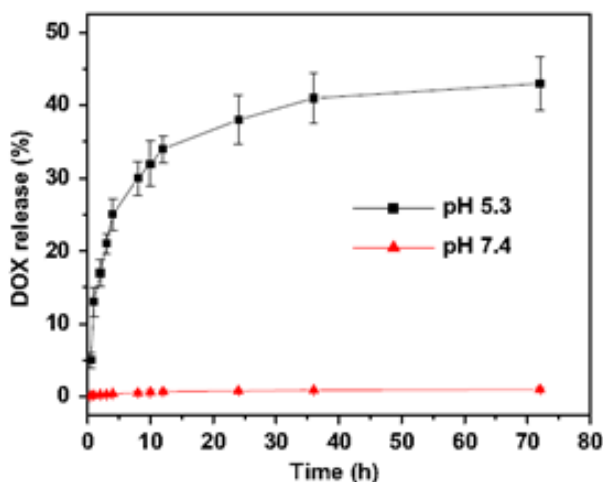
Fig. 1.10. *DOX release profile of thiol terminated-cRGD-conjugated nanocarriers at pH=5.3 and 7.4 [115].*

Cell-specific targeting with magnetic nanocarriers can be carried out by two mechanisms: active and passive targeting mechanisms. The first strategy relies on the attraction of a drug and nanocarrier conjugates to the affected site using recognition ligands which are attached to the surface of conjugates such as antibodies, low molecular weight ligands, e.g., folic acids, peptides, etc. The active strategy can also be achieved through manipulation of physical stimuli (e.g., temperature, pH, magnetism). On the other hand, passive targeting is a result of enhanced vascular permeability and retention (EPR) which is characteristic of leaky vasculature of

tumours [98]. Once drug-nanocarrier conjugates reach the diseased tissues, the therapeutic agents (i.e. drugs etc.) are released. A controlled release of drugs from nanocarriers can be achieved through changes in physiological environment such as temperature, pH, osmolality, or *via* an enzymatic activity. Both of these strategies are discussed below in detail.

(ii) Passive targeting

The clearance kinetics and *in-vivo* biodistribution of nano-drug carriers depend on the physicochemical factors like size, surface charge, and surface hydrophobicity and can be manipulated to enable passive targeting [98]. NPs injected into the living systems are rapidly coated with opsonin proteins present in the blood and form large aggregates. This phenomenon is known as opsonization. Such opsonised particles are identified by RES (Reticuloendothelial system) or MPS (Mononuclear phagocyte system) which is comprised of macrophages related to liver and spleen [116].
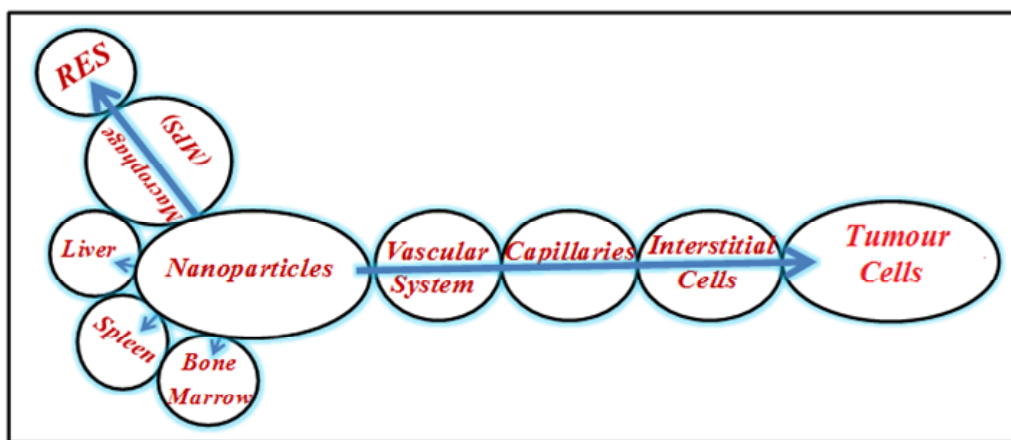
Fig. 1.11. *Distribution and routes of nanoparticles after intravenous injection.*

RES is an immune system consisting of phagocytic cells. These cells travel in the vascular system as monocytes and reside in their particular tissues. These

phagocytic cells internalize the opsonised NPs via phagocytosis and deliver them to the spleen, liver and bone marrow (Fig. 1.11). This clearance can occur within few minutes to few hours after administration, thus removing the active NPs from the circulation and prevent their access to the tumour tissue. This natural tendency of localizing in the RES gives an excellent opportunity for passive targeting of drugs to the macrophages present in the liver and spleen.

The non-specific uptake by RES acts as a major barrier in the targeting of nano-drug carriers to organs other than liver and spleen. The ability of nanocarriers to avoid RES uptake is very important for achieving prolonged circulation time in the blood which is prerequisite for efficient drug delivery. The fate of nanocarrier *in-vivo* depends on the hydrodynamic size, morphology, shape, charge and surface chemistry of the particles. The overall size of carrier must be sufficiently small to evade rapid splenic filtration but large enough to avoid renal clearance. Coating the surface of NPs and reducing their size to <100 nm can mask them that they are no longer recognized by the MPS or RES and remain in circulation for longer time [117-118]. Owing to pathophysiological differences of tumour and infracted regions from normal tissues, particles ranging from 10 to 200 nm in size can leave the vascular capillary bed and accumulate in the interstitial space of such regions [119]. In most cases, endothelial cells are tightly bounded to each other and limit the permeation of nanocarrier. NPs can passively extravasate into tumour through leaky blood vasculature and can result in significant accumulations. This phenomenon is known as enhanced permeability and retention (EPR) effect, (Fig. 1.12) which is the most accepted approach for passive tumour targeting by the nanocarrier [120-121]. When NPs are administrated via intravenous injections, adsorption of plasma proteins may promote undesired

recognition and clearance by the RES cells. Non-specific interactions with extracellular matrix and non-targeted cell membrane can also hinder the efficient delivery of NPs to targets [122]. To overcome the above mentioned problems, nanocarriers are suggested to have neutral surface charge and high colloidal stability at physiological conditions. The decoration of neutral surface ligands with hydroxyl groups, especially hydrophilic polyethylene glycol (PEG) onto the surface of NPs (PEGylation) is a well-known strategy to avoid opsonization, improve stability and remain in circulation for longer time [123-124]. Coatings of hydrophilic polymers create a cloud of chains at the particle surface which repel plasma proteins and inhibit their adsorption to the particle surface resulting in evading RES uptake.
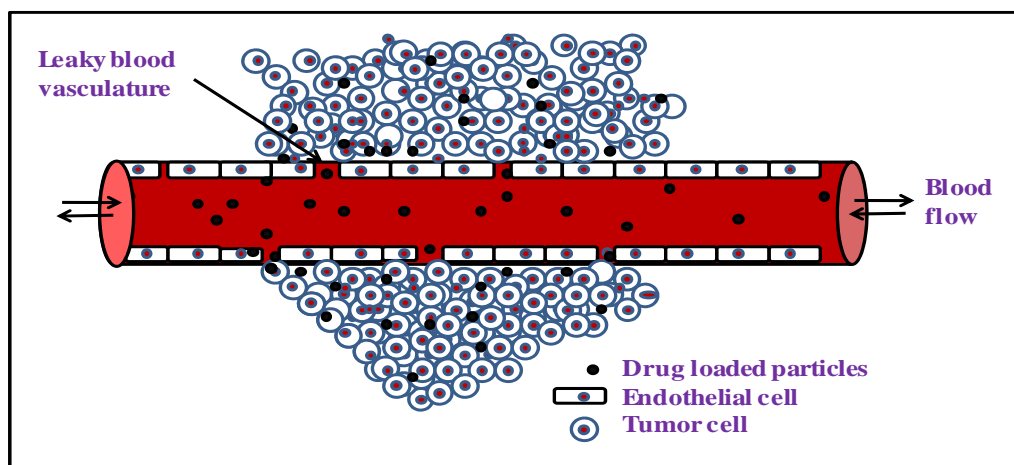
Fig. 1.12. Schematic representation of passive tumour targeting by enhanced permeation and retention effect.

As EPR effect driven passive drug delivery occurs only in tumour, the drug loaded NPs have limited penetration in normal tissues resulting in minimizing the side effects of chemotherapy [125]. The rapid uptake of MNPs in the form of Ferumoxides AMI-25 by Kupffer cells of healthy hepatic parenchyma allows for their

differentiation from diseased tissue by the contrast enhancement observed under MRI [125-126].

(iii) Active targeting

Direct administration of a drug into an affected organ or tissue may be technically difficult, or the disease site may be delocalized. Sometimes the affected area does not differ much from normal tissues in terms of vascular permeability, temperature and local pH value etc. Now-a-days, actively targeted MNPs are envisioned as a promising complementary strategy to EPR to further supplement the efficiency of cancer nanomedicines. Targeting of the nanocarriers to the site of interest is known as "active targeting or site-specific targeting" of the nanocarriers [127-130].
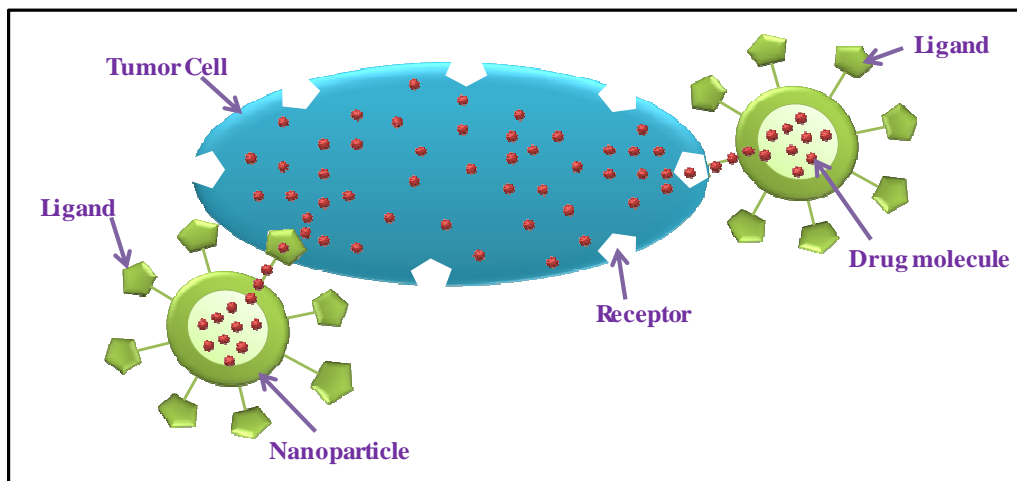
Fig. 1.13. Representation of receptor mediated active nanocarrier targeting.

There are many kinds of targeting molecules or ligands including proteins (mainly antibodies and amino acids), nucleic acids (aptamers), and other receptor ligands (transferrins, folic acids, proteins, peptides, small molecules, etc.). The receptors and surface bound antigens may be over expressed in diseased cells as

compared to the normal cells. Targeting ligands that bind to internalization prone receptors are utilized for surface modification of the nanocarriers [131]. These receptor–ligand or antigen–antibody interactions provide an effective strategy to improve the residence time in tumour tissues (Fig. 1.13). The ligand-anchored NPs bind to the tumour-specific or over expressed antigens leading to accumulation in the tumour tissue. The main requirement of this strategy is that they can recognise and interact with the tumour cells. That intrinsic characteristic is considered a major challenge to the development of actively-targeted NPs [132]. Here again, the systemic clearance of the MNPs affects the amounts available in the bloodstream supplying to the tumour. Therefore, actively-targeted NPs need to be designed to have extended blood circulation times. Similarly, because molecular targets are usually situated in the extravascular space of the tumour, NPs rely on the EPR effect to reach their targets [133-134]. Some of the examples of targeting molecules that have been frequently used for NP targeting and properties of the resultant conjugates based on the type of targeting molecule are discussed below.

There are two common approaches for the receptor-mediated NP targeting. The first approach is to target the tumour cell surface receptors. The second is to target the tumour microenvironment including the extracellular matrix or the surface receptors on the endothelial cells. Over expression of the surface receptors by tumour cells improves the cellular uptake of the nanocarriers. Therefore, the approach is aimed toward increasing interactions between NPs and tumour cells and enhancing internalization of drugs without altering the overall biodistribution. The following is an overview of receptor-mediated active tumour-targeting strategies.

Transferrin Receptors

Transferrin is a serum non-heme iron binding glycoprotein that transport iron to the cancer cells and these are endocytosed into acidic compartments where the iron dissociates. The transferrin receptor is over expressed in tumour cells due to the increased requirement of iron [135-136]. The difference in receptor binding between free ligands and ligands formulated with particles could be attributed to the multiple interactions between each ligand-modified particle and cell surface receptors. Davis et al. [137] demonstrated a novel study of small interfering RNA (siRNA) delivery in non-human primates using transferrin-conjugated liposomes. The efficacy of these transferrin-conjugated liposomes proved to be very efficient in metastatic mouse models of Ewing's sarcoma. In an interesting study, Wu et al. [138] demonstrated that transferrin-conjugated liposomes along with DOX and verapamil (Tf-L-DOX/VER) efficiently overcome multidrug resistance [138]. In DOX-resistant K562 cells, Tf-L-DOX/VER showed 5.2 and 2.8 times greater cytotoxicity (IC_{50} = 4.18 μM) than non-targeted liposomes (L-DOX/VER) (IC_{50} = 21.7 μM) and Tf-targeted liposomes loaded with DOX alone (Tf-L-DOX) (IC_{50} = 11.5 μM), respectively.

Folate Receptors

Folic acid (FA) is a small-molecule vitamin which is necessary for the human body. It is an important coenzyme in the synthesis
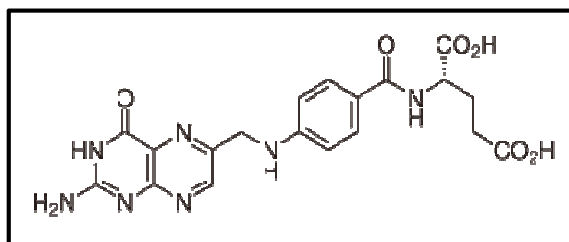
Fig. 1.14. *Structure of folic acid.*

of DNA and serves as a cofactor in the synthesis of many enzymes. Its molecular structure is shown in Fig. 1.14.

FA is a stable, low cost and non-immunogenic molecule that binds strongly to folate receptors present on the surface of cancer cells, through ligand-receptor binding. Hence, folic acid can effectively be used to target the tumour cells [139-140]. The use of folate ligands for targeting is because of their easy conjugation to carriers, retain high binding affinity, and high stability in storage and in circulation. The expression of the folate receptors is very much conserved in normal animal cells due to the lack of a key enzyme for folate biosynthesis in normal cells. However, folate receptors are over expressed in many malignant tumours such as ovarian cancer, nasopharyngeal cancer, kidney cancer, breast cancer, endometrial cancer, testicular cancer and liver cancer. Therefore, FA is of high potential as a tumour-targeting molecule. Various attempts have been undertaken to actively target nanopreparations to tumour by conjugating FA to a NP-surface [141-146].

In a recent study, a folate conjugated ternary copolymer, FA-polyethylene glycol-polyethyleneiminepoly(caprolactone) (FA-PEG-PEI-PCL) was developed for co-delivery of drug and siRNA to the ovarian tumour cells [147]. In another study, folate-polymer coated liposomes were developed by Alexiou et al. [148] for targeted chemotherapy. DOX was used as the model drug for the targeted drug delivery. In their study, FA conjugated poly-L-lysine (PLL) was used as a coating material on the surface of doxorubicin loaded anionic liposomes. FA-polymer coated liposomes demonstrated higher cellular uptake of loaded doxorubicin by folate receptor over expressing human nasopharyngeal carcinoma KB cells that resulted in two-fold higher cytotoxicity compared to PLL-coated liposomal doxorubicin.

(c) Combination Therapy

Literature reports show that hyperthermia treatment is much more effective when implemented in combination with other treatment methods like radiation, chemotherapies etc. The major drawback of chemotherapies and radiotherapies is that they are relatively non-specific. Because of non-specificity of these therapies, there is considerable toxicity to normal cells even under optimized conditions. However, if such treatments could be localised, e.g. to the infected site only, then the regular use of these therapeutic drugs will be very potent and efficient agents could be made possible. Recognition of this led researchers in the late 1970s to propose the use of magnetic nanocarriers for targeted drug delivery within the body. The objectives are two folds: first, to minimize the side-effects of the cytotoxic drug by reducing the systemic distribution of the drug to the normal and healthy tissues and second, to enhance the accumulation of NPs at the target site using an external magnetic field.

Magnetic drug targeting (MDT) is defined as the site specific delivery of chemotherapeutic agents to their target using MNPs bound to these agents, with an external magnetic field generated at the tumour site. These drug-nanocarrier conjugates (in the form of a biocompatible ferrofluid) are injected in the body via the circulatory system. When the magnetic particles entered the bloodstream, high-gradient magnetic field from outside is applied to concentrate the ferrofluid at a specific target site within the body. Once the drug-nanocarrier conjugate is concentrated at the target, the drug can be released either by the enzymatic activity or changes in physiological conditions such as pH, osmolality, or temperature and that drug can be taken up by the tumour cells. The mechanism of drug localization using magnetic delivery systems is based on the competition between forces exerted by

blood compartment on the particles and magnetic forces generated from the applied magnetic field. When the magnetic forces exceed the linear blood flow rates in capillaries, the magnetic particles are retained at the desired or targeted site and may be internalized by the endothelial cells of the target tissue [149-151]. This approach helps in the localization of the drug to the desired site and it also minimize the accumulation of drug in healthy tissues. A combination of improved target selectivity and increased duration of drug exposure to the target also reduces the overall amount of drug taken up by the RES. MDT uses much smaller doses of drug leading to several fold increased drug efficacy and reduced drug toxicity [152-154].

(i) Advantages of MDT

In addition to some of the key advantages of MDT already mentioned above, the MNPs used in MDT also offer distinct advantages:

➢ MNPs are biocompatible, non-toxic, cost effective, non-immunogenic and injectable;

➢ MNPs have controllable sizes, high magnetic susceptibility and also show increased accumulation at the targeted area;

➢ they can be made to respond resonantly to AMF, resulting in the transfer of energy from the exciting field to the nanoparticle (in case of hyperthermia);

➢ reduction of the drug required for the treatment and also the side-effects owing to the drug [154];

➢ drug incorporated MNPs can penetrate through small capillaries and accumulation at the targeted sites can be controlled by an external magnetic field;

➢ sustained drug release is possible with biocompatible MNPs;

➢ with the help of MRI, the drug uptake process can be visualized.

The effectiveness of MDT depends on several physical factors (magnetic field strength, magnetic gradient and magnetic properties of the particles), hydrodynamic factors (blood flow rate in the capillaries, concentration of nanocarrier and circulation time of the particles in the blood) and physiological factors (penetration depth and strength of the drug-carrier binding).

Hayashi et al. [155] synthesized superparamagnetic iron oxide nanoparticles (SPION) which were further modified with FA and PEG for enhanced drug accumulation in tumours. The surface modification was achieved via thiol-ene click reaction. After 24 h of intravenous injection, they observed that FA and PEG-modified SPION nanoclusters (FA-PEG-SPION NCs) were accumulated locally in the tumour site and MRI contrast get enhanced. Furthermore, 24 h after intravenous injection of the NCs, the mice were placed in AMF with H = 8 kA/m and f = 230 kHz (Hf= $1.8×10^9$ A/m·s) for 20 min. and tumours of the mice underwent local heating. After 20 minutes of heating, the temperature of the tumour tissues was found to be around 6°C higher than that of the surrounding tissues. The tumour volume of treated mice was reduced to 1/10 of the control mice after 35 days after treatment. Furthermore, the treated mice were alive after 12 weeks but control mice died up in 8 weeks after treatment.

Barick et al. [156] synthesized water dispersible, pH responsive peptide mimic shell cross-linked magnetic nanocarriers (PMNCs) using a facile soft chemical approach. The drug-loading efficiency of the nanocarriers was investigated using anticancer drug, doxorubicin hydrochloride (DOX) as a model drug to evaluate their potential as a carrier system. Their results showed high loading affinity of nanocarriers for DOX, their sustained release profile, magnetic field-induced heating,

and substantial cellular internalization. The enhanced toxicity of DOX-loaded PMNCs (DOX-PMNCs) for tumour cells under AMF suggests their potential for combination therapy involving hyperthermia and chemotherapy. They observed the combined effects of magnetic hyperthermia and chemotherapy on HeLa cells (Fig. 1.15).
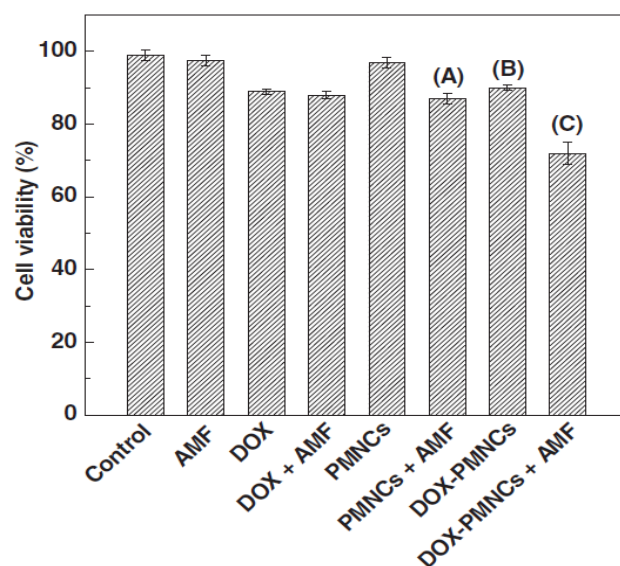
Fig. 1.15. *Effect of combination therapy (magnetic hyperthermia and chemotherapy) on HeLa cells using DOX-PMNCs with a DOX concentration of 8μM along with various control groups [156].*

The control cells with and without AMF and the PMNCs showed very little decrease (<3%) in cell viability. However, DOX-PMNCs showed about 10% decrease in cell viability. PMNCs in the presence of AMF also showed 13% decrease in cell viability as compared to the marginal decrease in the presence of PMNCs alone. As expected, no further significant decrease in cell viability is observed when DOX loaded cells were subjected to AMF. It is interesting to note that DOX-PMNCs in combination with AMF (C) showed much higher cytotoxicity (i.e. 28% decrease in

cell viability) than individual treatments of PMNCs with AMF (A) and DOX-PMNCs (B). Their study exhibits the potential of peptide mimic shell cross-linked nanocarriers for combination therapy.

(d) Magnetic Resonance Imaging (MRI)

Magnetic resonance imaging (MRI) is an imaging technique used primarily in medical settings to produce high-quality anatomical images of the human body. Based on the principles of nuclear magnetic resonance (NMR), MRI relies on the counterbalance between the exceedingly small magnetic moment on a proton and the exceedingly large number of protons present in biological tissue, which leads to a measurable effect in the presence of large magnetic fields [157-158]. In clinical practice, MRI is used to distinguish pathologic tissue (e.g., a brain tumour) from normal tissue. One advantage of an MRI scan is that it is non-invasive to the patient. It uses strong magnetic fields and non-ionizing radiation in the radio frequency range. The recent development of molecular and cellular imaging which aims for visualizing the disease-specific biomarkers at the molecular and cellular levels has led to prevalent recognition of the MNPs as MRI contrast agents.

Recently, superparamagnetic iron oxide (SPIO) nanoparticles have been widely investigated and developed as an MRI contrast agent [159]. Many other unusual MNPs also have potential application as MRI agents. Dai et al. [160-161] reported FeCo/graphitic shell nanocrystals synthesized by a scalable chemical vapour deposition method. The FeCo nanocrystals can be used as an advanced MRI agent because of its ultra-high saturation magnetization, τ_1 and τ_2 relaxivities.

1.3. Gap areas and scope of the present investigations

In view of the diverse biomedical applications of the MNPs, the main objective of the present investigations is to explore various strategies to develop surface functionalized MNPs and composite materials with a view to utilize them as carriers for drug delivery and magnetic hyperthermia applications. Though there have been some reports on synthesis and surface modification of various nanoparticles, as discussed before, there is a pressing need to develop various biocompatible coatings, in a cost effective and scalable manner. Moreover, the effect of surface modification on inherent properties of the material needs to be investigated so as to fine tune the formulation for efficacy and biodistribution. Improved colloidal stability, resistance to protein adsorption, good specific absorption rate, effective heat transport, site specific targeting, improved biodistribution etc are some of the important properties that are envisaged in a new formulation. This has stimulated the quest for new protocols and binding ligands in the preparation of MNPs. This thesis is an attempt to address some of these issues. Specifically, the following objectives are addressed in this thesis:

➢ To device new protocols for the synthesis of polyethylene glycol coated magnetic nanoparticles for the biomedical applications.

➢ To explore the use of conducting polymer such as polyaniline, as a matrix for magnetic nanoparticle impregnation and its use for heat activated killing of cancer cells.

➢ To explore synthesis and characterization of phosphate anchored magnetic nanoparticles and their application in thermal therapy.

➢ Preparation of folic acid conjugated magnetic nanocarriers for targeted drug delivery.

> ➢ To synthesize luminescent marker conjugated magnetic nanoparticles for drug
> tracking.

Chapter 2

Experimental techniques

Structural, morphological and interfacial characteristics of nanostructured materials have important implications in fine tuning the physico-chemical properties of drug delivery systems. The materials reported in the present thesis are characterized by a variety of tools for their microstructure, morphology, stability etc. Some of the characterization tools include X-ray diffraction (XRD), dynamic light scattering (DLS), Fourier transforms infrared spectroscopy (FTIR), UV-Visible spectrophotometry, zeta-potential measurements, specific absorption rate (SAR) measurements by induction heating. Other than these main techniques, there are some complementary techniques which employed for the materials characterization. The principles of these techniques are briefly described in this chapter.

2.1. X-Ray Diffraction (XRD)

X-ray diffraction analysis is one of the most widely used techniques for the characterization of crystalline materials. To understand and explain the properties of materials, the knowledge regarding its crystal structure and coordination environment around the atoms in the lattice is very crucial. XRD patterns of the samples can give valuable information on these aspects. The technique is briefly described below:

X-rays are electromagnetic radiations, discovered by Röntgen in 1895. Frequencies of X-Rays are in between ultra-violet (UV) and gamma radiations, and their wavelength (λ) range from 0.04 Å to 1000 Å. X-rays are generated when a fast moving electron collide with the metallic targets. During this phenomenon, electrons from the inner shell get knocked out and higher level electrons get transferred to the inner orbits and the difference in energy between the two orbits is emitted. These emitted rays are called as X-rays and they superimpose over a broad background. The broad background is known as white radiation or Bremsstrahlung radiation which

arises due to the deceleration occurring with the incident electron beam due to its interaction with the electric field of the target metal.

When X-rays are incident on a crystalline material, they are either coherently/incoherently scattered or absorbed. The coherent scattering of rays can interfere with each other giving rise to bright (constructive interference) and dark (destructive interference) fringes. When the wavelength is fixed, the scattered rays will become constructive only at a particular angle. This phenomenon is termed as X-ray Diffraction. Fig. 2.1 represents the crystallographic planes, and the path traversed by incident and scattered rays, indicating the path difference between the two rays.
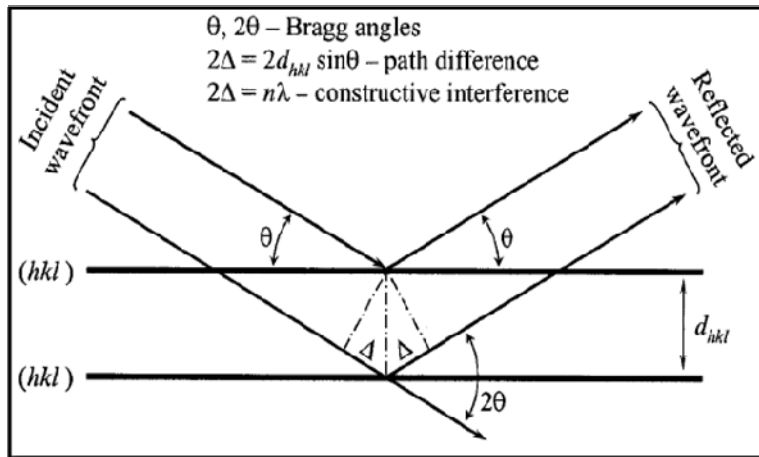
Fig. 2.1. *Schematic representation of the diffraction of X-rays from crystallographic planes.*

The necessary condition for constructive interference of X-rays and its relation to the inter-planar separations of the lattice is given by the following equation (Bragg's law of diffraction)

$$n\lambda = 2dSin\theta \qquad \text{............... (2.1)}$$

where λ is the wavelength of X-rays, θ is the glancing angle, d is interplanar separations, and n is the order of diffraction. Each plane is characterized by miller indices, hkl. If wavelength of radiation and the diffraction angle are known, the interplanar spacing can be calculated from the diffraction pattern.

2.1.1. Powder X-ray diffraction

Experimental set up for X-ray diffraction consists of X-ray source, sample holder, X-ray slits and a detector. A ray diagram of powder X-ray diffractometer is shown in the Fig. 2.2. X-ray beam pass through the Soller and divergence slits and then falls on the sample, which spread uniformly over a rectangular area of a glass slide. The scattered or diffracted X-rays from the sample again pass through receiving and Soller slits and then fall on a secondary monochromator before detection. The monochromator separates out the stray wavelength radiation and diffracted rays get passed through the detector slits and reach to the detector for the diffraction pattern of the sample.
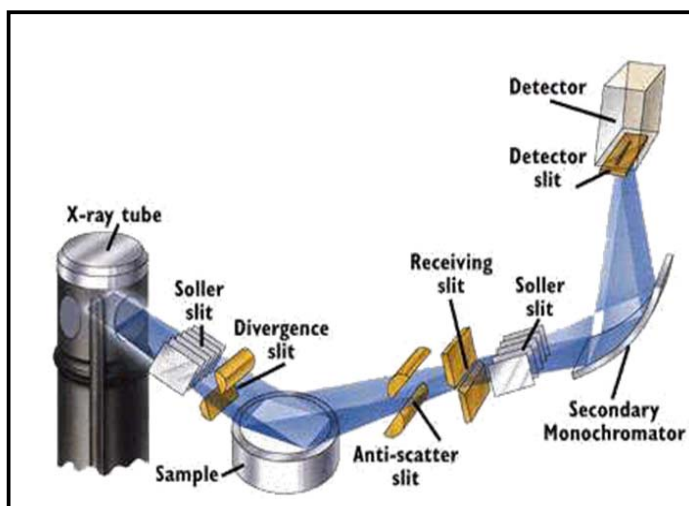
Fig. 2.2. *Ray diagram of a typical reflection mode diffractrometer (this figure is taken from www.anal.lscable.com).*

The observed diffraction patterns were compared with JCPDS (Joint Committee on Powder Diffraction Standards) for reported crystalline samples. Nanostructured materials exhibit broad diffraction peaks due to limited number of lattice planes within the grains. The line width of the diffraction peak depends on the size of the crystallites. The average crystallite size of the particles can be calculated from the full width at half maximum (FWHM) of the diffraction peaks in the XRD pattern of particle using Scherrer's formula,

$$t = \frac{0.9\lambda}{B Cos\theta_B}$$ ……….…… (2.2)

where t is the thickness of the crystal (in Å), λ is wavelength of the X-rays and θ_B is Bragg angle. The line broadening, B is measured from FWHM (Warren formula):

$$B^2 = B_M^2 - B_S^2$$ .... (2.3)

Where B_M is the measured peak width in radians at half peak height of the material and B_S is the measured peak width of a peak of a standard material (silicon).

In the present study, Philips 1710 diffractometer was used for XRD measurements. The Cu-Kα line was used as the incident beam with a Ni filter. A curved graphite single crystal was used to monochromatize the diffracted rays. A proportional counter (argon filled) was employed as a detector. The X-ray tube rating was maintained at 30 kV and 20 mA. Samples were well powdered and made in the form of a thin slide prior to mounting in the diffractometer.

2.2. Dynamic light scattering (DLS)

Dynamic light scattering (DLS) is a well-known characterization technique to obtain hydrodynamic size of nearly spherical particles. In this technique, random

intensity fluctuations arising from the Brownian motion of colloidal particles are processed by digital correlator to obtain the intensity autocorrelation function. The correlation function can be analysed to get the mean size or polydispersity (distribution width) or complete distribution data even for multimodal distributions. The correlation function yields information about the diffusion coefficient of the nanoparticles in solution which in turn is related to the hydrodynamic radius of the colloidal particle in suspension. A schematic representation of the experimental setup is as shown in Fig. 2.3.
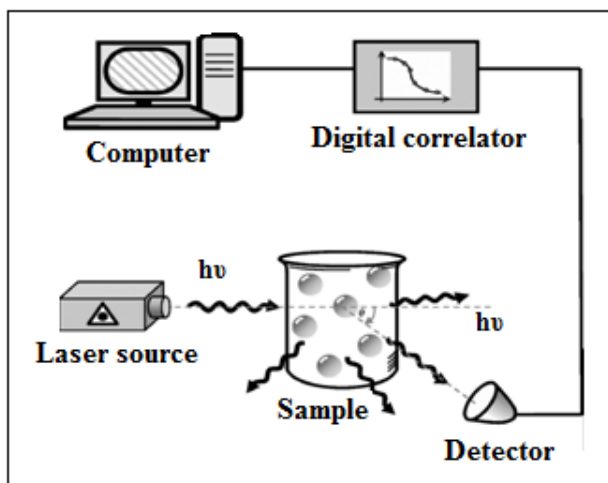
Fig. 2.3. *Schematic representation of dynamic light scattering technique.*

The principle of this technique is that the suspended particles are not stationary but they diffuse in a random walk fashion known as Brownian motion. Since the net intensity seen by the detector is a result of the superposition of all the waves scattered from the scattering volume, the intensity fluctuate randomly in time as the phases of the scattered waves fluctuate randomly due to random movement in the relative positions of the particles which scatter the light. Time scale of these fluctuations depends on the size of the diffusing particles. Small particles diffuse in the solution

relatively rapidly resulting in a rapidly fluctuating intensity signal as compared to the larger particles which diffuse slowly [162].

Fig. 2.4 shows representative time dependent scattered intensity plots for small and large sized particles as observed on the same time scales for both the particles. A mathematical procedure known as autocorrelation is used to obtain quantitative information from the fluctuations in the scattered intensity. Therefore, this technique is also known as photon correlation spectroscopy.
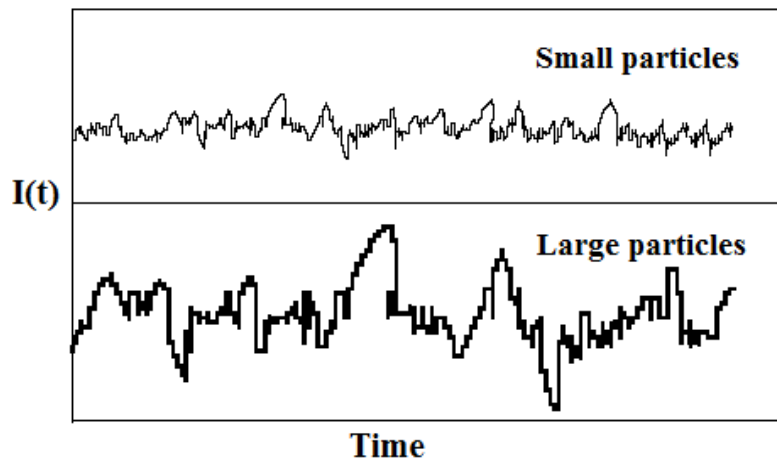
Fig. 2.4. *Typical fluctuations in scattered intensity for 'large' and 'small' particles when observed in the same time scale.*

The autocorrelation function, denoted by $C(\tau)$, represents the correlation or comparison between the values of the scattered intensity at a given time t and at a later time $(t+\tau)$. By representing intensity at an arbitrary time as $I(o)$ and those at a later time τ as $I(\tau)$, the autocorrelation function can be written as

$$C(\tau)=<I(o).I(\tau)> \qquad \text{...........…………….....(2.5)}$$

When the sampling interval τ becomes very large, there should not be any correlation between the pairs of sampled intensities and hence the above equation reduces to

$$C(\infty) = <I(o)>^2 \qquad\qquad \text{....................... (2.6)}$$

An autocorrelator accepts the digital photo counts from the detector which represents the light scattering intensity $I(t)$ and computes the second order correlation function, normalized with the long time correlation data $<I>^2$. The normalized time correlation function $g^{(2)}(\tau)$ of the scattered intensity can be written as

$$g^{(2)}(\tau) = \frac{<I(o)I(\tau)>}{<I>^2} \qquad\qquad \text{…..……...… (2.7)}$$

For photo counts obeying Gaussian statistics, the relationship between $g^{(2)}(\tau)$ and the first order correlation function of the electric field $g^{(1)}(\tau)$ is given by the Siegert relationship

$$g^{(2)}(\tau) = \beta + A \left| g^{(1)}(\tau) \right|^2 \qquad\qquad \text{………..……….(2.8)}$$

where β is the baseline and A is an adjustable parameter which is dependent on the scattering geometry and independent of τ.

For a suspension of monodisperse, rigid, spherical particles undergoing Brownian diffusion, the correlation function decays exponentially as

$$g^{(1)}(\tau) = \exp(-Dq^2\tau) \qquad\qquad \text{....………….. (2.9)}$$

where D is the translational diffusion coefficient. For small, dilute, non-interacting spheres the hydrodynamic radius R_h can be obtained from the translational diffusion coefficient using the Stokes-Einstein relationship given by

$$D= kT / (6\pi\eta R_h)$$
.......……….. (2.10)

where k is the Boltzmann constant, η is the solvent viscosity and T is the absolute temperature.

DLS measurements were performed using a Malvern 4800 Autosizer employing a 7132 ~digital correlator. The light source was a He-Ne laser operated at 632.8 nm with maximum power output of 15 mW. All measurements were carried out at $25.0\pm0.1^{\circ}C$ using a circulating water bath. Cylindrical cells of 10 mm diameter were used in all of the light scattering experiments. The intensity of scattered light was measured five times for each sample at 130° angle. The autocorrelation functions were analyzed by the method of CONTIN.

2.3. Fourier transforms infrared spectroscopy (FTIR)

Infrared (IR) spectroscopy is a popular characterization technique in which a sample is placed in the path of an IR radiation source and absorption of different IR frequencies by the sample is measured. Solid, liquid and gaseous samples can be characterized by this technique. IR photons energies are used for the transitions in vibrational energy states. These states are associated with a molecule's bonds, and consequently each molecule has its own unique signatures. Hence, IR spectroscopy may be used to find the type of bond between two or more atoms and consequently identify functional groups. IR spectroscopy is also broadly used to characterize the attachment of organic ligands to organic/inorganic nanoparticles and surfaces. The

covalent bonds between the atoms or molecules vibrate at specific frequencies corresponding to their vibrational energy levels. The vibrational frequencies depend on several factors including bond strength and the atomic mass. Chemical bonds can be distorted in different ways such as stretching (symmetrical and asymmetrical), scissoring, rocking, wagging and twisting. Absorption of IR radiation causes transitions among different vibrational energy states and the energy associated with absorbed IR radiation is converted into these types of motions. The IR absorption spectrum of a molecule can be a unique *fingerprint* for its identification. Samples can be prepared in several ways for an IR measurement. For powders, a small amount of the sample is added to potassium bromide (KBr), after which this mixture is ground into a fine powder and subsequently compressed into a small, thin, quasi-transparent disc. For liquids, a drop of sample may be sandwiched between two salt plates, such as NaCl.

FTIR technique is based on Michelson interferometer. A typical Michelson interferometer consists of two perpendicular mirrors and a beam splitter. One of the mirror is a stationary mirror and another one is a movable mirror as shown in the Fig. 2.5. Light from the polychromatic infrared source, is collimated and directed to a beam splitter. The beam splitter is designed to transmit half of the light and reflect half of the light. Subsequently, the transmitted light and the reflected light strike the stationary mirror and the movable mirror, respectively. When reflected back by the mirrors, two beams of light recombine with each other at the beam splitter. If the distances travelled by two beams are the same which means the distances between two mirrors and the beam splitter are the same, the situation is defined as zero path difference (ZPD). But imagine if the movable mirror moves away from the beam

splitter, the light beam which strikes the movable mirror will travel a longer distance than the light beam which strikes the stationary mirror. The distance which the movable mirror is away from the ZPD is defined as the mirror displacement and is represented by Δ. It is obvious that the extra distance travelled by the light which strikes the movable mirror is 2Δ. The extra distance is defined as the optical path difference (OPD) and is represented by delta. Therefore,

$$\delta = 2\Delta \qquad\qquad \text{........................ (2.11)}$$

It is well established that when OPD is the multiples of the wavelength, constructive interference occurs because crests overlap with crests, troughs with troughs. As a result, a maximum intensity signal is observed by the detector. This situation can be described by the following equation:

$$\delta = n\lambda \quad (\text{ n} = 0,1,2,3...) \qquad\qquad \text{..................... (2.12)}$$

In contrast, when OPD is the half wavelength or half wavelength add multiples of wavelength, destructive interference occurs because crests overlap with troughs. Consequently, a minimum intensity signal is observed by the detector. This situation can be described by the following equation:

$$\delta = (n+1/2)\lambda \quad (\text{n} = 0,1,2,3...) \qquad\qquad \text{........................ (2.13)}$$

These two situations are two extreme situations. If the OPD is neither n-fold wavelengths nor (n+1/2)-fold wavelengths, the interference should be between constructive and destructive. So the intensity of the signal should be between maximum and minimum. Since the mirror moves back and forth, the intensity of the signal increases and decreases which gives rise to a cosine wave. The plot is defined as an interferogram. When detecting the radiation of a broad band source rather than a

single-wavelength source, a peak at ZPD is found in the interferogram. At the other distance scanned, the signal decays quickly since the mirror moves back and forth. Because there needs to be a relative scale for the absorption intensity, a background spectrum must also be measured. This is normally a measurement with no sample in the beam. This can be compared to the measurement with the sample in the beam to determine the "percent transmittance". This technique results in a spectrum which has all of the instrumental characteristics removed. Thus, all spectral features which are present are strictly due to the sample. A single background measurement can be used for many sample measurements because this spectrum is characteristic of the instrument itself.
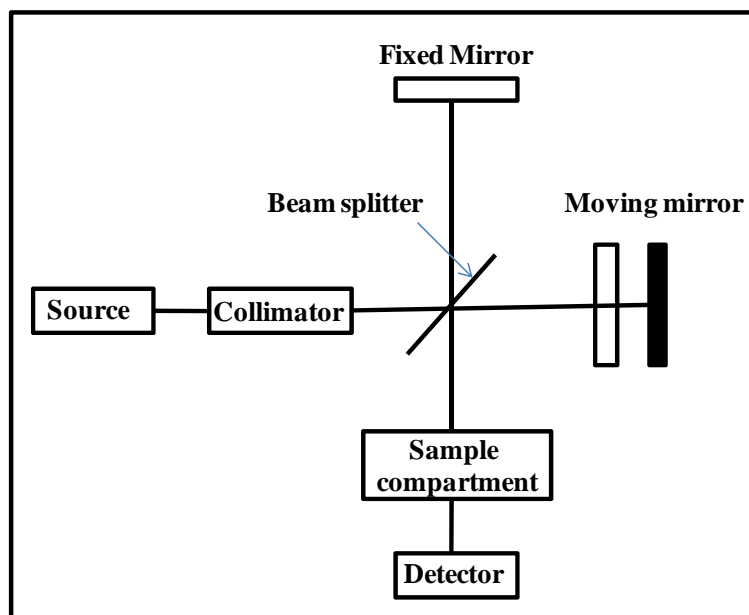
Fig. 2.5. *Schematic diagram of Michelson interferometer.*

In the present study all infrared experiments were carried out using Bomen Hartman and Braun, MB series. FTIR machine having a range of 400-4000 cm^{-1} and with a resolution of 4 cm^{-1}. IR radiation was generated from globar source (silicon

carbide rod). The instrument used CsI single crystal, as the beam splitter and deuterated triglycine sulphate (DTGS) as detector. Prior to IR measurements, the samples were ground thoroughly by mixing with dry KBr powder, made in the form of a thin pellet and introduced into the sample chamber of the instrument to record the spectra.

2.4. Zeta-potential measurements

Surface properties of a particle are very important for optimization of conjugation chemistry. Surface charge on the particles is measured by zeta (ζ) potential analysis. The surface charge of a particle can be sensitive to pH of the suspending medium. The isoelectric point, also referred to as PZC (point of zero charge), is the pH at which the particles in suspension have a net charge of zero and no mobility in the electric field. Electrophoretic mobility measurements provide information about the magnitude of charge slightly away from the particle surface. The counter ions surrounding a charged particle surface exists as two regions; an inner region (Stern layer) where the ions are strongly bound and an outer region (diffuse layer) where they are less firmly associated. Within the diffuse layer there is a notional boundary inside where the ions and the particles form a stable entity. When a particle starts to move (e.g. due to applied electric field), ions within the notional boundary also move with the particle. The ions which are beyond the boundary stay with the bulk dispersant solution. The potential at this boundary is called the zeta-potential (Fig. 2.6).

The value of zeta-potential provides an idea about the potential stability of the colloidal system. If all the particles in suspension have a large negative or positive zeta-potential then they tend to repel each other and there will be no tendency for the

particles to come together and hence is considered a stable suspension. However, if the particles have low zeta-potential values then there will be no force to prevent the particles from coming together and flocculating. The general dividing line between stable and unstable suspensions is generally taken at either +30 or -30 mV, depending on the surface charge of the particles. Particles with zeta-potentials more positive than +30 mV or more negative than -30 mV are generally considered quite stable. Zeta-potential can be estimated by electrophoresis. The basic theory related to electrophoresis is introduced in the following section.
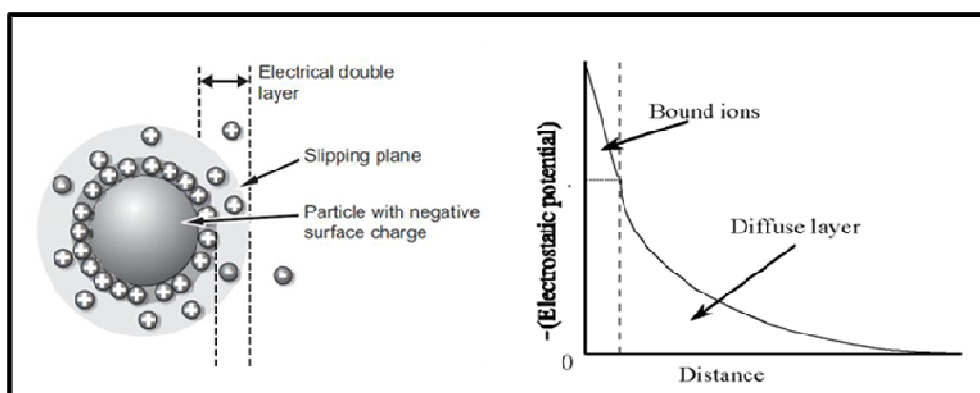
Fig. 2.6. *Schematic representation of the electrical double layer surrounding particle and electrostatic potential near a negatively charged spherical particle.*

2.4.1. Electrophoresis

When electric field is applied across the electrolyte solution, charged particles migrate towards the oppositely charged electrode. But the viscous forces acting on the particles tend to oppose this movement. After reaching equilibrium between these two opposing forces, the particles move with a constant speed. The speed of the particles depends on many factors such as the strength of the electric field or voltage gradient, dielectric constant and viscosity of the medium, and the zeta-potential. The speed of a

particle in a unit electric field is termed as the electrophoretic mobility of that particle. The relation between zeta-potential and electrophoretic mobility is given by the Henry equation

$$U_E = \frac{2\varepsilon\zeta f(\kappa a)}{3\eta}$$

………………….. (2.14)

where U_E is the electrophoretic mobility, ζ is the zeta-potential, ε is the dielectric constant of dispersing medium, η is the viscosity of medium and $f(\kappa a)$ is Henry's function. The term, 'κ' is known as Debye length and its unit is reciprocal length and κ^{-1} is often taken as a measure of the thickness of the electrical double layer. The parameter, 'a' refers to as the radius of the particle and therefore κa measures the ratio of the radius of the particle to the thickness of electrical double layer. Electrophoretic determinations of zeta-potential are most commonly determined in aqueous media and moderate electrolyte concentration. In this case, the value of f(κa) is 1.5, and this is referred to as the Smoluchowski approximation. Therefore calculation of zeta-potential from the mobility is simple for systems that fit the Smoluchowski model, i.e. particles larger than about 0.2 microns dispersed in electrolytes containing more that 10^{-3} molar salt. Also, for small particles in low dielectric constant media (e.g. non-aqueous media), f(κa) becomes 1.0 and allows an equally simple calculation and this is referred to as the Huckel approximation.

Zeta-potential measurements were made with a Zetasizer nanoseries, Malvern instruments, UK by phase analysis light scattering with applied field strength of 2.5 x 10^3 V/m. The light source was a He-Ne laser operated at 632.8 nm with a power of 4 mW. The experiment was carried out using a quartz cuvette (universal 'dip' cell) with 10 mm light pathway. The measurements were performed at 25°C. The zeta-

potential (ζ) values are calculated from the electrophoretic mobility data using Smoluchowsky approximation.

2.5. UV-Visible spectrophotometry

Ultraviolet-visible (UV-Vis) spectrophotometry is widely utilized to quantitatively characterize organic and inorganic nanosized molecules. In this technique, a sample is irradiated with electromagnetic waves in the UV and visible region and the absorbed light by the sample is analyzed through the resulting spectrum. It can be employed to identify the constituents of a substance based on the known electronic absorption spectra and to determine its concentrations. The samples can either be organic or inorganic and may exist in solid, liquid or gaseous form.

Electromagnetic radiation is absorbed or emitted only in discrete packets (photons). The energy E of the photon is defined as

$$E = h\nu \qquad\qquad \text{……………..} (2.15)$$

where h is the Planck's constant and ν is the frequency of the electromagnetic radiation. Absorption of radiation by the sample results in the allowed transition of electrons to a higher energy level. When an incident light falls on the sample, part of the light is absorbed and/or scattered and the remaining light is transmitted through the sample. Transmittance (T) is defined as the ratio of the radiant power transmitted by the sample (I) to the radiant power incident (I_o) on the sample. Thus

$$T = \frac{I}{I_0} \quad \text{…} \qquad\qquad \text{…………...} (2.16)$$

The absorbance A is defined as the negative logarithm of transmittance. The basic law underlying UV-Vis spectroscopy is the Beer-Lambert's law which relates absorbance of the sample with the concentration of the absorbing species as follows

$$A = -\log T = \varepsilon bc$$.…………….. (2.17)

where c is the concentration in moles per litre, b is the length of the path of the light beam in the sample, and ε is the molar absorptivity, which depends on the wavelength and the nature of the absorbing species.

Spectrophotometer is the instrument which measures the ratio of the incident (I_o) to the transmitted radiant power (I) as a function of spectral wavelength. The basic components of the spectrophotometer are: source, monochromator, sample compartment, detector, and recorder (Fig. 2.7). The double beam recording spectrophotometer features a continuous change in the wavelength and an automatic comparison of the light intensities of sample and the reference material. The instrument either plots the transmittance or the absorbance as a function of the wavelength of light.

The light from the source is alternatively split into two beams by a rotating mirror; one beam is passed through the sample and the other through the reference. The detector alternately sees the beam from the sample and then the reference. Its output gives the ratio of I/I_o directly i.e. the reference correction is made automatically. These spectrometers use photodiode arrays as the detector to record the transmittance at different wavelengths. The light source is a continuum source such as a tungsten lamp. All wavelengths pass through the sample. The light is dispersed by a diffraction grating after the sample and the separated wavelengths fall on different pixels of the array detector. The resolution depends on the grating, spectrometer

design, and pixel size, and is mostly fixed for a given instrument. These instruments use only a single beam light, so a reference spectrum is recorded and saved to produce transmittance or absorbance spectra after recording the sample spectrum.
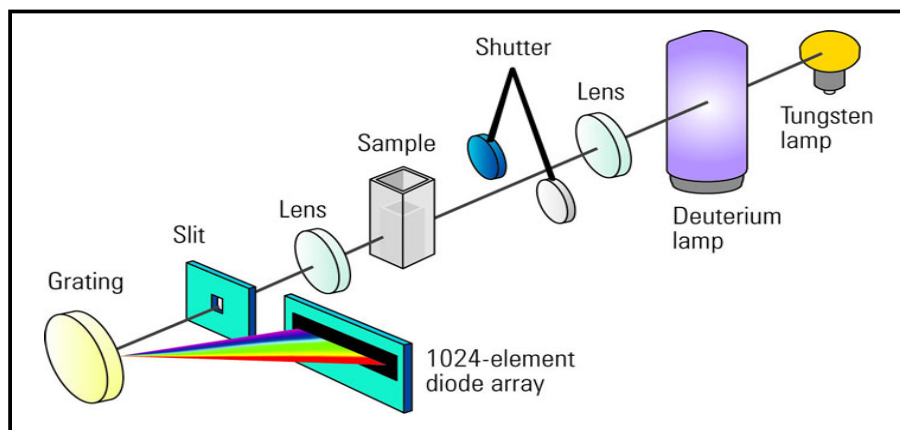
Fig. 2.7. *Schematic representation of spectrophotometric technique (this figure is taken from www. eo-miners.eu).*

In the present thesis, the colloidal stability of the particles were investigated by measuring the change in absorbance of sample suspensions (0.1 mg/mL) in different medium at a wavelength of 350 nm using JASCO V-650, UV-visible spectrophotometer. Any changes in the particle size will affect the scattering and absorption of the light at 350 nm and hence changes in the extinction of light. So the extinction of light measured by a spectrophotometer can be used as a measure of the particle stability.

2.6. Specific absorption rate (SAR) measurements by induction heating

Induction heating is the process of heating an electrically conducting object (usually a metal) by electromagnetic induction, where eddy currents are generated within the metal and resistance leads to Joule heating of the metal. An induction

heater (Fig. 2.8) consists of an electromagnet, through which a high-frequency alternating current (AC) is passed. Heat may also be generated by magnetic hysteresis losses in materials that have significant relative permeability. The frequency of AC used depends on the particle size, material type, coupling (between the work coil and the object to be heated) and penetration depth.

The heating ability of sample suspensions was obtained from the time-dependent calorimetric measurements using induction heating unit. 1 mg/mL of suspensions were taken in an eppendorf with suitable arrangements (eppendorf was kept at the centre of the induction coil with the support of thermocol) to minimize the heat loss. The AMF of 0.251, 0.335 and 0.419 kOe, and fixed frequency of 265 kHz were used to evaluate the specific absorption rate (SAR). The rise in temperature was also monitored using a high resolution infrared (IR) camera (Thermal Imager Testo 875-1), and analyzed by thermography software (Testo IR Soft Software, version 3).
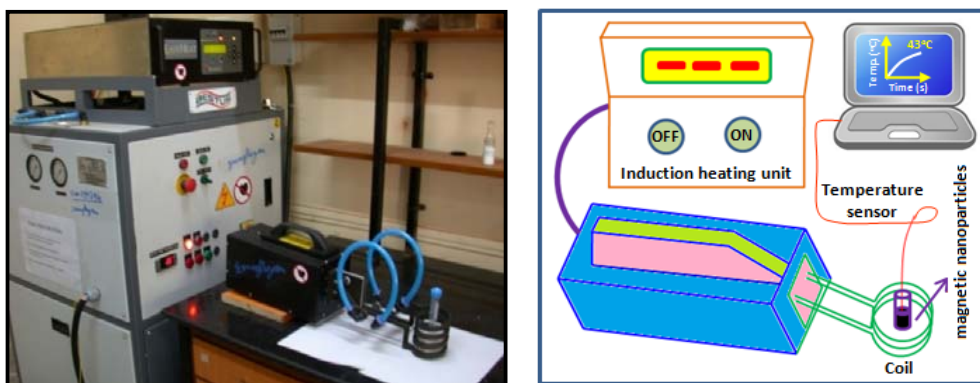
Fig. 2.8. *Photograph of induction heating unit and its schematic representation.*

2.7. Drug loading

The anticancer agent, doxorubicin hydrochloride (DOX) was used as a model drug to estimate the drug loading and release behaviour of the MNPs. In order to

investigate the interaction of drug molecules with MNPs, the fluorescence spectra of pure DOX and DOX loaded MNPs was taken. The aqueous dispersion of different amounts of MNPs (0, 20, 40, 60, 80 and 100 μg from a stock suspension of 2 mg/mL) were added to a 1ml of DOX solution (1mg/mL) and mixed thoroughly by shaking at room temperature for 15 min. The fluorescence spectra of the supernatant (obtained after magnetic sedimentation of drug loaded MNPs) were then recorded using Hitachi F4500 fluorescence spectrophotometer. The fluorescence intensities of supernatants (washed drug molecules were also taken into consideration for calculations) against that of pure DOX solution were used to determine the loading efficiency. The loading efficiency (w/w %) was calculated using the following relation:

$$\text{Loading efficiency}(\%) = \frac{(I_{DOX} - I_S - I_W)}{I_{DOX}} \times 100 \qquad \text{..............} (2.18)$$

where I_{DOX} is the fluorescence intensity of pure DOX solution, I_S the fluorescence intensity of supernatant and I_W the fluorescence intensity of washed DOX (physically adsorbed DOX molecules).

2.8. Drug release studies

The pH triggered drug release studies were carried out under reservoir–sink conditions such as (a) Acetate Buffer (AB)-pH=5 (reservoir) vs. Acetate Buffer (AB)-pH=5 (sink); (b) Phosphate Buffer Saline (PBS)-pH=7.3 (reservoir) vs. Phosphate Buffer Saline (PBS)-pH=7.3 (sink), and (c) Acetate Buffer (AB)-pH=5 (reservoir) vs. Phosphate Buffer Saline (PBS)-pH=7.3) (sink). For release study, the amount of DOX loaded MNPs was quantified according to the binding isotherm. The loading was carried out, at increased scale (to use these particles for release studies), by incubating 0.5 mL of aqueous solution of DOX (1mg/mL) with 2.5 mL of the aqueous suspension

of MNPs (5 mg) for 1h in dark (however, no decrease in fluorescence intensities was observed after 15 min of incubation). The drug-loaded MNPs (5 mg) were immersed in 5 mL of pH=5/pH=7.3 and then added into a dialysis bag. The dialysis was performed against 200 mL of the respective sink medium under continuous stirring at 37°C to mimic the cellular environment. One mL of the external medium was withdrawn and replaced with the same fresh medium at fixed intervals of time to maintain the sink conditions. The amount of doxorubicin released was determined by measuring the fluorescence emission at 585 nm (excitation wavelength-490 nm) using a plate reader (Infinite M1000, Tecan-I control, Switzerland) against the standard plot prepared under similar conditions. Each experiment was performed in triplicates and the standard deviation was also calculated.

2.9. Transmission electron microscope (TEM)

Transmission electron microscopy (TEM) is a microscopy technique in which a beam of electrons is transmitted through an ultra-thin specimen, interacting with the specimen as it passes through. An image is formed from the interaction of the electrons transmitted through the specimen; the image is magnified and focused onto an imaging device,
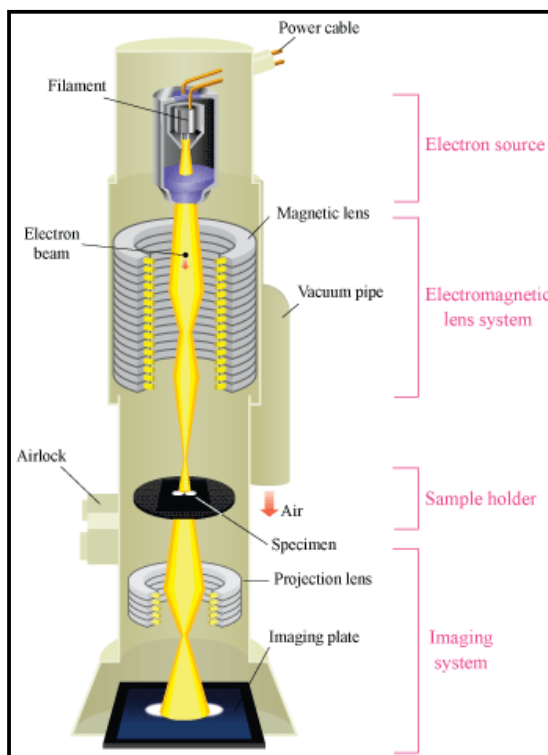
Fig. 2.9. Schematic representation of TEM (this figure is taken from www.hk-phy.org).

such as a fluorescent screen, on a layer of photographic film, or to be detected by a sensor such as a CCD camera. TEM is routinely used for the determination of particle core size.(crystalline and amorphous parts) and gives access to a number weighted mean value.

The TEM micrographs were observed by CM 200 Philips TEM. The average interfringe distances of samples were obtained by using image J software. The samples for TEM were prepared by making clear dispersion of the NPs in isopropyl alcohol using ultrasonic bath (20 kHz, 500 W) for 10 min and putting a drop of the solution on a carbon coated copper grid. The solution was allowed to evaporate under a UV lamp leaving behind the NPs on the carbon grid. In TEM, a beam of focused high-energy electrons is transmitted through the sample to form an image, which reveals information about its morphology, crystallography and particle size distribution at a spatial resolution of ~1 nm. TEM is unique as it can focus on a single nanoparticle and can determine its crystallite size. This technique is applicable to a variety of materials such as metals, ceramics, semiconductors, minerals, polymers, etc. [163-164]. TEM setup consists of an electron gun, voltage generator, vacuum system, electromagnetic lenses and recording devices and the schematic diagram of TEM is shown in Fig. 2.9. Usually thermionic gun (tungsten filament, LaB_6 crystal, etc.) or field emission gun is used as an electron source to illuminate the sample. The electrons thus produced are accelerated at chosen voltages by a voltage generator. The electron beam after passing through the condenser lens system is directed towards a thin sample. Typically TEM specimen thickness is in the range of 50 to 100 nm and should be transparent to the electron beam. The microscope column is maintained at high vacuum levels to prevent scattering of electrons by the atmosphere inside the

microscope. Information is obtained from both transmitted electrons (i.e. image mode) and diffracted electrons (i.e. diffraction mode). In TEM, contrast formation depends greatly on the mode of operation. In conventional TEM, contrast is obtained by two modes namely the mass-thickness contrast and the diffraction contrast and both are based on amplitude contrast. In high resolution transmission electron microscopy (HRTEM), image contrast is due to phase contrast. Mechanism of all these types of contrasts is briefly discussed below.
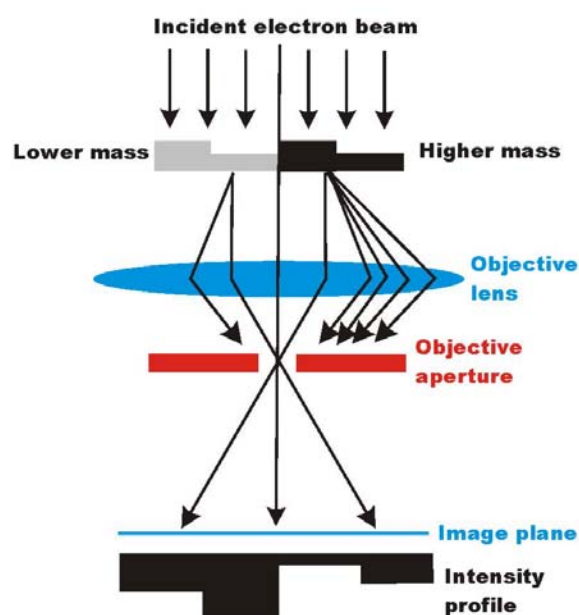
Fig. 2.10. *Schematic representation of mass-thickness contrast (this figure is taken from www.microscopy.ethz.ch).*

Mass-thickness contrast: This is the common mode of operation in TEM and the image obtained is a simple two-dimensional projection of the sample. The interaction of electrons with heavy atoms is stronger than with light atoms (Fig. 2.10). If the thickness is homogeneous, areas in which heavy atoms are concentrated appear with

darker contrast than such with light atoms (mass contrast). Of course, more electrons are scattered in thick than in thin areas; thus, thick areas appear dark (thickness contrast). However, a thick area with light elements might have the same contrast as a thinner area with heavier atoms. If the sample has crystalline areas, many electrons are strongly scattered by Bragg diffraction (especially if the crystal is oriented along a zone axis with low indices), and this area appears with dark contrast in the bright field (BF) image as well (diffraction contrast).

Diffraction contrast: In the case of a crystalline sample, the electron beam undergoes Bragg scattering and it disperses electrons into discrete locations. By the placement of apertures in these locations, i.e. the objective aperture, the desired Bragg reflections can be selected (or excluded), thus only parts of the sample that are causing the electrons to scatter to the selected reflections will end up projected onto the imaging apparatus. A region without electron (electron deficient region) will appear dark because there will be no reflections from that region. This method can be used to identify the lattice defects in crystals. By carefully selecting the orientation of the sample, it is possible to determine the position and type of defects present in the sample.

Phase contrast: Among all the techniques used to obtain structural information of materials, HRTEM has the great benefits that it gives information about the complicated structures, crystal defects, precipitates, bulk structure etc. In HRTEM, phase contrast is used for the imaging. High resolution images are formed by the interference of elastically scattered electrons, leading to a distribution of intensities that depends on the orientation of the lattice planes in the crystal relative to the electron beam. Therefore, at certain angles the electron beam is diffracted strongly

from the axis of the incoming beam, while at other angles the beam is completely transmitted. In the case of high-resolution imaging, this allows the arrangement of atoms within the crystal lattice to be deduced. For HRTEM measurements, sample should be very thin.

2.10. Thermogravimetric analysis (TGA)

The physico-chemical changes (removal of solvent and organic molecules or degradation) during thermal treatment were analyzed by Setaram Instrumentation using 10°C/min heating rate under inert (N_2) atmosphere. The change in weight (%) of sample was plotted against temperature in thermogravimetric analysis (TGA) to obtain the chemical changes occurred in the samples upon thermal treatment.

2.11. Magnetic measurements

The magnetic properties of the samples were measured by physical property measurement system (PPMS, Quantum Design). The room temperature field dependence magnetic measurements (M *vs.* H) were carried out on powder samples mounted tightly in the sample holder by varying magnetic field. The temperature dependence magnetization under zero-field cooled (ZFC) and field cooled (FC) conditions in a constant applied field were measured by PPMS. In the ZFC measurements, the samples were cooled from 280 to 5 K without applying an external field. After reaching 5 K, a field was applied and the magnetic moments were recorded as the temperature increased. For FC measurements, the samples were cooled from 305 K under an applied field; then the magnetic moments were recorded as the temperature increased.

2.12. Hemocompatibility assay

In order to determine the hemocompatibility of MNPs, percentage of hemolysis was measured. Briefly, 5 mL human blood was mixed with 2 mL sodium oxalate (2 wt.%) and 2.5 mL solution of sodium chloride (NaCl, 0.9 wt.%). Next, 2 mg of MNPs was added to 10 mL of 0.9 wt.% NaCl solution and incubated at $37^{o}C$ for 30 min. Subsequently, 0.2 mL diluted blood was added into the prepared samples and incubated at $37^{o}C$ for another 30 min. The liquid was centrifuged at 3000 rpm for 5 min. The absorbance of the supernatant (haemoglobin concentration) was measured with a UV-visible spectrophotometer at wavelength of 545 nm. The negative (in 0.9 wt.% NaCl solution) and the positive control (in Milli Q water) were also prepared. The percentage of hemolysis was calculated as follows:

$$\text{Hemolysis } (\%) = \frac{A_{s} - A_{neg}}{A_{pos} - A_{neg}} \times 100 \qquad \text{………….. (2.19)}$$

where A_{s}, A_{neg}, A_{pos} are the absorbance of the sample, the negative control and the positive control, respectively. The percentage of hemolysis was calculated based on the average of three replicates. High hemocompatibility was given for samples with <5% hemolysis, hemocompatible for samples within 10% hemolysis, and non-hemocompatible for >20% hemolysis.

2.13. Cell culture and Cell viability assay

Cells were seeded into 96-well plates at density of 1×10^{4} cells per well for 24h. Then different concentrations of NPs suspension (0, 0.0165, 0.03125, 0.0625, 0.125, 0.25, 0.5, 1.0 mg/mL) were added to cells and incubated for 24 h at $37^{o}C$ and 5% CO_2.

Thereafter, the cells were washed thrice with PBS and processed for SRB/ MTT assay to determine the cell viability.

2.13.1. Cell viability by sulphorhodamine B (SRB) assay

Sulforhodamine B (SRB) assay was performed to evaluate cytocompatibility of the MNPs with HeLa cell lines. For this, cells were fixed with a solution of 50% trichloroacetic acid and stained with 0.4% SRB dissolved in 1% acetic acid. Cell-bound dye was extracted with 10 mM unbuffered Tris buffer solution (pH=10.5) and then absorbance was measured at 560 nm using a plate reader. The cell viability was calculated using the following formula:

$$\% \, \text{Viability} = \left(\frac{\text{Absorbance of sample}}{\text{Absorbance of control}} \right) \times 100 \quad \quad \text{…………..(2.20)}$$

2.13.2. Cell viability by MTT assay

The biocompatibility of the NPs with MG63 (Osteosarcoma) cells were evaluated using the 3-(4, 5-dimethylthiazol-2-yl)-2, 5-diphenyltetrazolium bromide (MTT) assay. MG63 cells were cultured in MEM supplemented with 10% serum and antibiotic solution (100 U mL^{-1} penicillin and 100 μg mL^{-1} streptomycin). For biocompatibility study, the cells were first seeded into a 96-well plate at densities of 1×10^3 cells per well for 24 h. Then different concentrations of nanoparticle suspension (0, 1.2, 9.65, 33.45, 50, 100 and 250 μg/mL) were added to each wells and incubated for another 24 h in 5 % CO_2 at $37^{\circ}C$. The cells supernatant was discarded and thereafter, 10 μL of MTT solution (5 mg/mL) was added and incubated for 4 h. Formazan crystal was solubilized by addition of 200 μL of solubilizing buffer (20% SDS in 50% DMF). The 96-well plate was centrifuged at 2000 rpm for 5 min and kept on magnetic rack for an hour. Supernatant was transferred into a new 96-well plate

and absorbance was measured at 570 nm with reference to 630 nm in BioTek Universal Microplate Reader. The percentage of cell proliferation was calculated as ratio of optical density (OD) of treated and control cells multiplied by 100. Further, the cytotoxicity of pure DOX and DOX-loaded particles (0.125 and 1 μM DOX) were also evaluated using the MTT assay. The drug concentrations were chosen based on the 50% inhibitory concentration (IC50) value of DOX for MG63 cells. For IC_{50} value of DOX, 1×10^3 cells were incubated with different amount of DOX (0.015-5μM) for 24 h and then processed for MTT assay. The experiments were performed in triplicate.

The heat activated killing of cancer cells (mouse Fibrosarcoma cells, WEHI-164) was also evaluated under AMF with respective controls by MTT assay. Cells (0.25×10^6) were seeded overnight in petridishes (P-60) containing 4 mL culture medium (complete DMEM) followed by treatment with MNPs (0.5 and 1 mg) for 3 h under culture conditions. Then, cultures were subjected to AMF (0.335 kOe) for 10 min under sterile conditions using an induction heating unit. After AMF exposure, cells were further cultured for 48 h. Then, the media containing NPs were carefully removed and the cells were further incubated with 0.5 mL of MTT solution (0.5mg/mL) at culture conditions for 2 h. The supernatant was aspirated and 1 mL of dimethyl sulfoxide (DMSO) was added to each culture dish to solubilize the MTT crystals. The crystals were thoroughly dissolved and further diluted (1:10) with DMSO. From P-60 culture dishes, 200 μL of solution was transferred to 96 well plates and the blue colour was read in a microplate reader at 544 nm. The cell viability was calculated by comparing the absorption of treated cells to that of control, which was defined as 100%.

2.14. Confocal microscopy

Cellular uptake of DOX loaded particles were studied by confocal microscopy. For confocal microscopy imaging, cells (0.5×10^6) were seeded on glass cover slips and cultured overnight. The cells were then treated with DOX loaded particles (10 μM DOX) for 3 h under culture conditions, followed by washing with PBS. The cells were mounted on a glass slide in cell mounting medium containing DAPI for nuclear staining. These cells were then imaged by confocal laser scanning microscopy (CLSM, LS510 Meta, Carl Zeiss, Germany). The excitation source used was an Ar ion laser (488 nm for DOX and 364 nm for DAPI) and the emission window was set at 575–615 nm and 430–480 nm for DOX and DAPI, respectively.

2.15. Protein interaction measurements by zeta-potential

The interaction of protein with MNPs was investigated by using Bovine serum albumin (BSA) as a model protein. MNPs were incubated with BSA solution in PBS (0.01 M, pH=7.3) with the final concentration of MNPs and BSA was 0.20 and 0.25 mg/mL. After incubation at 37°C for required time, BSA conjugated MNPs (MNPs-BSA) were magnetically separated from reaction mixture.

2.16. Protein interaction measurements by SDS-PAGE (for PAMN)

The detection of protein corona (protein-particle interaction) formed around the nanoparticle from either plasma or cytosolic fluids were carried out according to the protocol by Lundqvist et al. [167]. Nanoparticle in 10 mM phosphate buffer pH=7.5, 0.15 M NaCl and 1mM EDTA were incubated with either plasma (200 μL) or cytosolic fluids (500 μL) for an hour. Samples were centrifuged at 16000 ×g for 5 min and washed thrice with 1 mL of 10 mM PBS pH=7.5, 0.15 M NaCl and 1 mM EDTA. Nanoparticle bound protein was mixed with 2×SDS-PAGE loading buffer and loaded

onto 12% SDS-PAGE gel to resolve the different proteins. The protein containing SDS-PAGE gel was stained in 0.25% staining solution (0.25g of Coomassie Brilliant blue R250 in 50 mL of methanol, 40 mL of water and 10 mL of acetic acid) on slowly rocking platform for 4 h at room temperature to visualize the protein bands. Destaining of gel was done with destaining solution (50 mL of methanol, 40 mL of water and 10 mL of acetic acid) on a slowly rotating platform for 24h with slight heating. Gel photograph was taken in high resolution scanner.

2.17. Materials used

Ferrous chloride tetrahydrate ($FeCl_2.4H_2O$), ferric chloride hexahydrate ($FeCl_3.6H_2O$), PEG-diacid (Poly (ethylene glycol) bis (carboxymethyl) ether, $M_n = 600$), aniline hydrochloride, NHS (N-Hydroxysuccinimide), bovine serum albumin (BSA) and thiazolyl blue tetrazolium bromide (MTT) were purchased from Sigma-Aldrich, USA. 25% ammonia solution and acetic acid were purchased from Thomas Baker Chemical Pvt. Ltd., India. Potassium peroxodisulfate and Tween-80 (Polyoxyethylene monooleate) were obtained from E. Merck (India) Ltd. Dimethyl sulfoxide (DMSO) was obtained from S. D. fine chemicals Ltd., India, respectively. 10-Undecenoic acid (Undecylenic acid) and AIBN (azobisisobutyronitrile) were obtained from Spectrochem Pvt. Ltd., Mumbai (India). L-Cysteine and EDC (Ethylcarbodiimide hydrochloride) were purchased from SRL, India. Dulbecco's modified eagle medium (DMEM) and fetal calf serum (FCS) were procured from Invitrogen, USA and Himedia Laboratories, India, respectively. Mouse Skin Fibrosarcoma (WEHI-164) and MG63 (Osteosarcoma) cells were obtained from National Centre for Cell Sciences (NCCS), Pune, India and culture medium, MEM was obtained from Sigma Inc. MO, USA. All chemicals were of analytical grade and

used without further purification. Milli Q water from a Millipore system was used to prepare aqueous solutions. The acetate buffer (AB) pH=5 and phosphate buffered saline (PBS)pH=7.3 were prepared using standard protocols.

Chapter 3

Synthesis and characterization of polyethylene glycol modified Fe_3O_4 magnetic nanoparticles for biomedical applications

3.1. Introduction

In the last decade, increasing interest has been devoted to the design of MNPs for different biomedical applications such as magnetic resonance imaging (MRI), drug delivery and heat activated killing of cancer cells (so called magnetic hyperthermia) [166-169]. Fe_3O_4 (magnetite) NPs have been widely used for *in-vitro* and *in-vivo* applications due to their non-toxicity, cytocompatibility, chemical stability over physiological conditions and significant accumulation at the target site [154]. Because of their high surface energy, MNPs show somewhat aggregation and may also interact with plasma proteins upon intravenous injection. Such interaction might bring about opsonization and immune system clearance through reticuloendothelial system (RES), resulting in dramatic loss of MNPs functions against target cells. Especially, the MNPs used for drug targeting should be chemically and colloidal stable, efficient and rapidly internalized into specific target cells. In order to achieve this, the MNPs should be modified with desired surface functionality. Various organic (surfactants, polymers) or inorganic (silica, gold) molecules are used for coating/surface functionalization of MNPs [170-174]. These coatings not only stabilize NPs but also provide accessible surface for the conjugation of biomolecules, targeting ligands and drugs. One of the most promising coating materials, poly(ethylene glycol) (PEG) a water soluble, biodegradable polymer has widely been used for PEGylation of MNPs, upon which MNPs become stealth evading the opsonization and RES [175-177]. The surfaces covered with PEG are non-immunogenic, non-antigenic and protein resistant [178-179]. Other important characteristics of PEG are its solubility in both polar and non-polar solvents and its high solubility in cell membranes. Therefore, the covalent conjugation of PEG on the surfaces of superparamagnetic nanoparticles is expected to

effectively improve their biocompatibility. The major advantage of PEG coating on Fe_3O_4 NPs is that it increases the half-life of the NPs during blood circulation because of its resistance to plasma protein deposition [180]. However, Fe_3O_4 NPs in contact with blood directly or indirectly for a long time may cause destruction of erythrocyte membrane integrity and hemolyzation [181]. In addition to protein resistant characteristic, the hemocompatibility is one of the most important issues that have to be addressed before the materials can be used for *in-vivo* applications.

In this chapter, we demonstrated the preparation of carboxyl PEGylated Fe_3O_4 magnetic nanoparticles (CPMN) by *in-situ* functionalization of Fe_3O_4 with PEG-diacid. PEG-diacid has a general structure of $HOOC-CH_2-(OCH_2CH_2)_nOCH_2-COOH$, encompassing a polyether backbone that is chemically inert with the terminal carboxyl groups. The terminal carboxyl groups may provide additional stability to the MNPs in addition to their steric stabilization achieved by PEG chain. Incorporation of anionic carboxyl groups along with PEG is highly advantageous for binding of cationic chemotherapeutic drugs. Thus, these CPMN can act as efficient candidates for targeted delivery of anticancer drug (doxorubicin), which can also be used as effective heating source for the hyperthermia therapy.

3.2. Synthesis of Carboxyl PEGylated Fe_3O_4 magnetic nanoparticles (CPMN)

The carboxyl PEGylated Fe_3O_4 magnetic nanoparticles (CPMN) were synthesized through co-precipitation of Fe^{2+} and Fe^{3+} in basic medium followed by *in-situ* coating of PEG-diacid [182]. In a typical synthesis, 1.988 g of $FeCl_2.4H_2O$ and 5.406 g of $FeCl_3.6H_2O$ were dissolved in 80 mL of water in a round bottom flask and temperature was slowly increased to 70^oC under N_2 atmosphere with constant mechanical stirring at 1000 rpm. The temperature was maintained at 70^oC for 30 min

and then 30 mL of 25% ammonia solution was added instantaneously to the reaction mixture, and kept for another 30 min at 70^oC. Then, 5 mL PEG-diacid was added and temperature was slowly raised upto 90^oC and reacted for 60 min with continuous stirring. The obtained black coloured CPMN were then thoroughly rinsed with water and separated using a permanent magnet (~2.5 kOe). The schematic representation of CPMN synthesis is shown in Fig. 3.1.
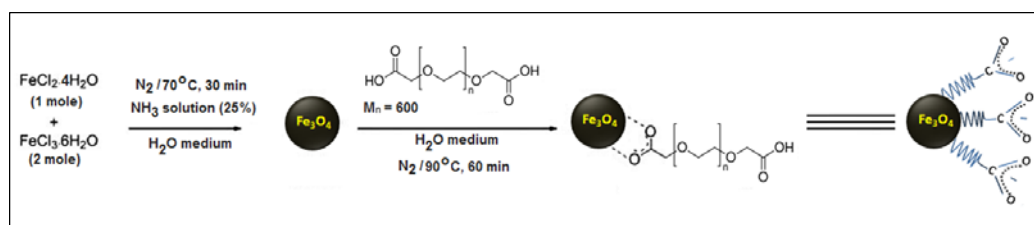
Fig. 3.1. *Schematic representation of the synthesis of CPMN.*

3.3.1. Structural Studies of CPMN

Carboxyl PEGylation was carried out by covalent coupling of PEG-diacid onto to the surface of Fe_3O_4 nanoparticles. XRD pattern of CPMN (Fig. 3.2a) showed the appearance of characteristic diffraction peaks, (220), (311), (400), (422), (511) and (440) with d-spacing of 2.968, 2.535, 2.103, 1.719, 1.614 and 1.478, respectively reveals the formation of single phase inverse spinel Fe_3O_4 structure (matched well with the reported value, JCPDS no. 65–3107). The average crystallite size of nanoparticles was found to be around 10 nm from X-ray line broadening using the Scherrer formula. Further, the presence of sharp and intense diffraction peaks confirmed the formation of highly crystalline nanoparticles. From TEM image (Fig. 3.2b), it was evident that Fe_3O_4 NPs were roughly spherical in shape with an average size of ~10 nm.
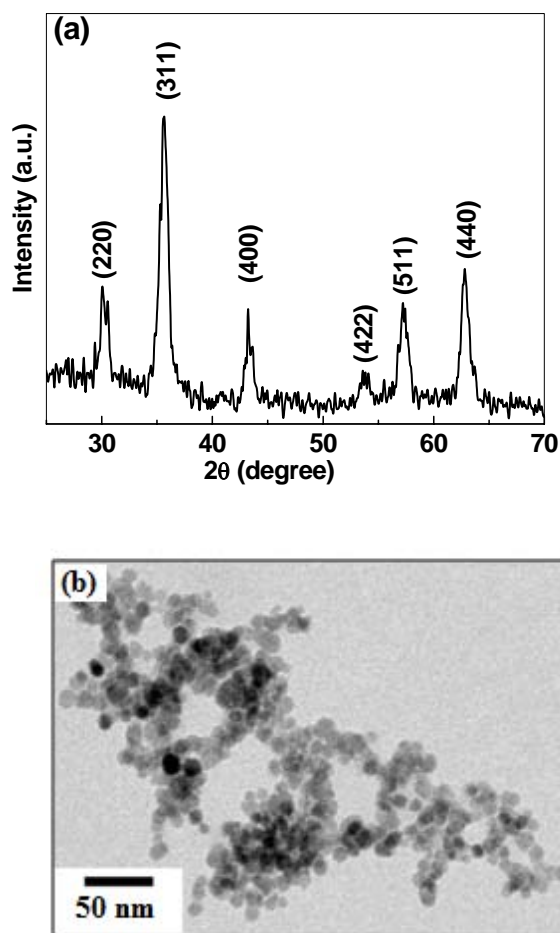
Fig. 3.2. *(a) XRD pattern, and (b) TEM micrograph of CPMN.*

FTIR spectra (Fig. 3.3) of PEG diacid and CPMN were investigated to find out the carboxyl PEGylation of Fe_3O_4 nanoparticles. The FTIR bands for the PEG-diacid are well resolved, but those of the CPMN are rather broad and few. The strong IR band observed at around 580 cm^{-1} in CPMN can be ascribed to the Fe-O stretching vibrational mode of Fe_3O_4 [183]. The characteristic C=O band of PEG-diacid at 1742 cm^{-1} is significantly reduced and an additional intense band appeared to a lower wave number, 1635 cm^{-1} in the spectra of the CPMN. This spectral change indicates the binding of some of the carboxylate group of PEG-diacid with Fe atoms on the surface

Fe_3O_4 (the binding of carboxylate group renders partial single bond character to the C=O bond, which shifts the stretching frequency to a lower value) [184]. However, the presence of weak C=O vibration at 1742 cm^{-1} in CPMN suggests the presence of free carboxyl groups on the surface of Fe_3O_4 nanoparticles. Zhang et al. [185] reported the chemisorption of polymethacrylic acid to Fe_3O_4 NPs via coordination linkages between the carboxyl groups and Fe. Occhipinti et al. [186] and Hu et al. [187] also demonstrated that one of the COOH head of PEG-diacid is preferable site for the chemical conjugation with Fe_3O_4 leaving the other one free. Further, the vibrational modes appeared at 1460 cm^{-1} (CH$_2$ scissoring) and 1025 cm^{-1} (carboxylic –OH group) in CPMN indicate the presence of PEG-diacid on the surface of Fe_3O_4 nanoparticles. The thermogravimetric analysis (TGA) of CPMN shows a weight loss of about 4% that clearly supports the organic modification on the surface of Fe_3O_4.
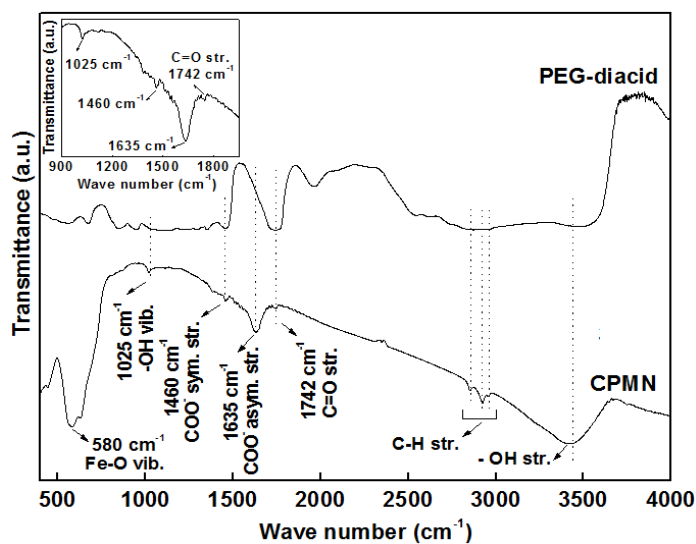
Fig. 3.3. *FTIR spectra of PEG-diacid and CPMN (inset shows the FTIR spectra of CPMN in the region of 900-1900 cm^{-1} revealing the appearance of C=O stretching vibration).*

3.3.2. Colloidal stability studies of CPMN

Colloidal stability of MNPs in aqueous and physiological medium is desired in most of the biomedical applications. From pH dependent zeta-potential measurements (Fig. 3.4), it has been found that CPMN have net positive surface charge below its isoelectric point (5.15), whereas negative surface charge above the isoelectric point. This difference in their charge properties may be attributed to the degree of ionization of functional groups at different pH values.
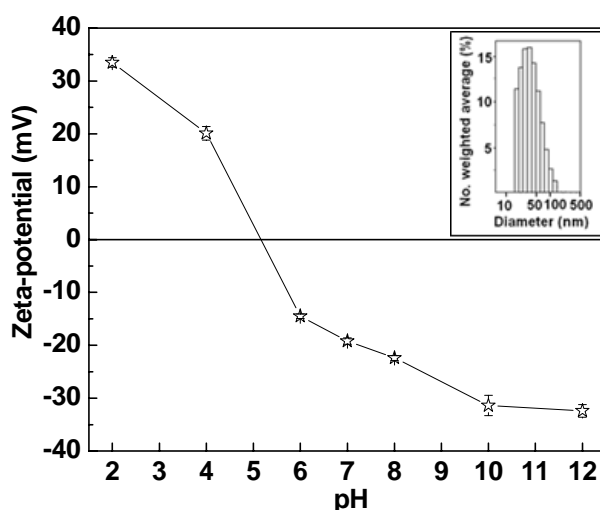
Fig. 3.4. *Zeta-potential (ζ) measurements of 0.05 mg/mL of aqueous suspension CPMN at different pH (inset shows its number weighted hydrodynamic diameter in water medium).*

Further, DLS measurements were performed in order to determine the hydrodynamic diameter of these CPMN in aqueous medium. DLS measurement (Inset of Fig. 3.4) indicates that these samples render aqueous colloidal suspension with mean intensity weighted hydrodynamic diameter of about 40 nm due to the presence of associated and hydrated organic layers [188]. The observed higher hydrodynamic diameter could also arise from the polydispersity of the particles. The surface carboxyl

groups may extend into the water medium, conferring a high degree of aqueous stability to Fe_3O_4 MNPs through hydrogen bonding. Further, the electrostatic contribution to the stabilization of MNPs is evident from the high negative zeta-potential values obtained at ambient condition in aqueous (-20 mV) and 0.01 M PBS (-28 mV) mediums.

3.3.3. Magnetic properties of CPMN

Fig. 3.5 shows the field-dependent magnetization plot of CPMN at 300 K (inset shows the photographs of CPMN in presence and absence of permanent magnet of field strength ~2.5 kOe). These NPs exhibit superparamagnetic behaviour with saturation magnetizations 67.4 emu/g at 20 kOe. The low value of magnetization of CPMN as compared to 92 emu/g of bulk Fe_3O_4 can be attributed to the combined effect of nano-sized particles and non-magnetic coating of PEG on their surface [189]. However, the retention of superparamagnetic property at room temperature with good magnetic field responsivity (inset of Fig. 3.4) makes these NPs suitable for biomedical applications.

3.3.4. Time-dependent calorimetric measurements of aqueous suspensions of CPMN

For hyperthermia applications, the temperature of cancerous tissue needs to reach 42-43°C for effective therapy. The time-dependent calorimetric measurements on aqueous suspension of CPMN to investigate their heating efficacy were performed. The temperature *vs.* time plots (Fig. 3.6a) of aqueous suspension of CPMN (1 mg/mL of Fe) showed a time-dependent gradual increase in temperature of CPMN suspension under AC magnetic fields. It has been observed that a magnetic field of 0.251 kOe at fixed frequency of 265 kHz is able to produce energy enough for raising the

temperature of the magnetic suspension of 1 mg/mL to 43°C (hyperthermia temperature) within 20 min. From Fig. 3.6b, it has been observed that SAR decreases with increasing the Fe concentration. This may be due to the decrease in Brownian contribution to hyperthermia and increase in magnetic dipole-dipole interactions between NPs in suspension as a result of increase in local concentration. At hyperthermia temperature, various cellular damaging mechanisms such as apoptosis, protein denaturation and DNA cross-linking may occur to destroy the tumour [190-191].
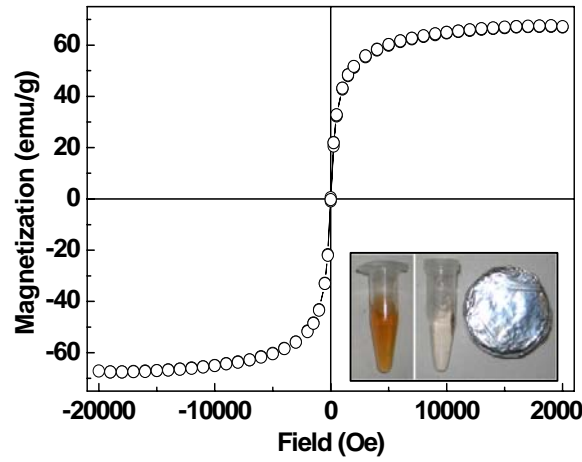
Fig. 3.5. *Field-dependent magnetization plot of CPMN at 300 K (inset shows the photographs of CPMN in presence and absence of permanent magnet of field strength ~2.5 kOe).*

Further, the time required to reach 43°C decreases with an increase in field strength, which is obvious as the heat generation/dissipation (*P*) is proportional to the square of applied AC magnetic field (inset of Fig. 3.6a) as follows [183]:

$$P = \pi \mu_0 \chi_0 H^2 f \frac{2\pi f \tau_{eff}}{1 + (2\pi f \tau_{eff})^2}$$

...…………. (3.1)

where μ_0 is the permeability of free space, χ_0 is the magnetic susceptibility, H is the magnetic field amplitude and τ_{eff} is the effective relaxation time. In thermal activation of superparamagnetic Fe_3O_4 NPs under AC magnetic field, an increase in temperature is mainly due to the combined effect of Néel and Brownian relaxations [183, 192]. The Néel and Brownian relaxation losses are associated with the magnetic moment rotations within the particles and with the entire particles, respectively.
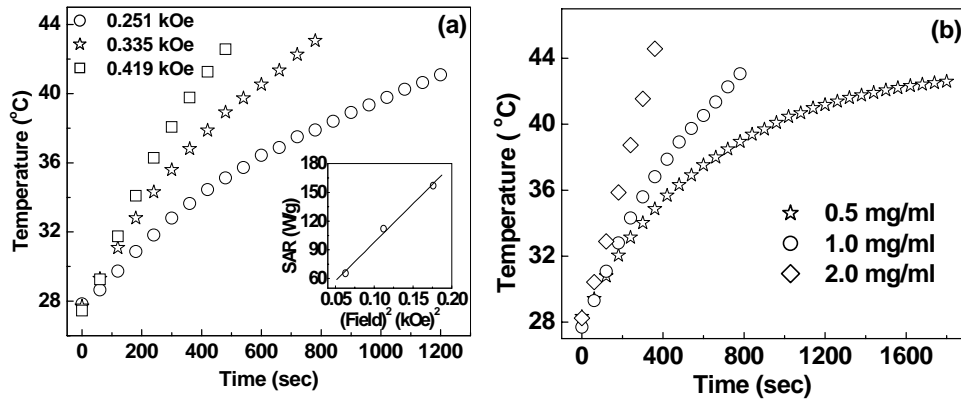
Fig. 3.6. *Temperature vs. time plots of CPMN of (a) 1 mg/mL at different applied fields (inset shows the linear relationship between SAR and square of applied AC magnetic field) and (b) different concentrations with an applied field of 0.335 kOe.*

The use of MNPs in hyperthermia therapy depends on their heating efficiency, which is expressed in terms of the specific absorption rate (SAR). SAR values of CPMN were found to be 65.5, 114 and 157 W/g of Fe with an applied field of 0.251, 0.335 and 0.419 kOe, respectively. The observed good SAR is likely to be due to a combination of their good magnetic field responsivity and aqueous colloidal stability. In addition to the applied field, SAR is also dependent on the concentration of iron in suspension, magnitude of frequency and physical properties of magnetic particles.

Therefore, the observed SAR values should not be viewed in terms of performances, but only as a demonstration that these magnetic nanoparticles are excellent heating source for hyperthermia treatment of cancer. Since SAR values are dependent on the field strength and frequency, we have calculated system-independent intrinsic loss power (*ILP*) using the following equation [193]:

$$ILP = \frac{SAR}{H^2 f}$$.…………..... (3.2)

where *SAR* is specific absorption rate, *H* is the field strength and *f* is the frequency. This equation is valid under frequencies of upto several MHz; samples with a PDI (Polydispersity index) of more than 0.1 and also provided the applied field strength is well below the saturation field of the MNPs. The AMF conditions employed during this study are expected to fulfil these requirements. The ILP values of CPMN were found to be 0.62, 0.60 and 0.56 nHm^2/Kg at applied fields of 0.251, 0.335 and 0.419 kOe, respectively. The ILP values obtained in present study are in the range of those reported for commercially available ferrofluids [193]. Therefore, these MNPs can be used as an excellent heating source for hyperthermia treatment of cancer.

3.3.5. Nanoparticle (CPMN)-Drug (DOX) Interaction

The interaction of an anticancer drug, doxorubicin hydrochloride (DOX) with CPMN was investigated by zeta-potential measurements (Fig. 3.7a). The zeta-potential of CPMN suspension (100 µg/mL) increased from -25.7 mV to -8.35 mV upon incubating with an aqueous solution of 10 µg/mL of DOX. This increase in zeta-potential arises from the binding of cationic DOX (protonated primary amine present on DOX induces a positive charge) with negatively charged CPMN by forming DOX-CPMN system through electrostatic interactions. The affinity of cationic DOX

towards negatively charged particles are well reported by various research groups [156, 184, 194, 195].

3.3.6. Drug loading and drug release profile of DOX-CPMN

A loading efficiency (w/w) of about 65% was obtained upon interacting 0.5 mL of aqueous solution of DOX (1mg/mL) with 2.5 mL of the aqueous suspension of CPMN (5 mg) for 1h in dark. The release of drug from DOX- CPMN system (Fig. 3.7b) shows a time dependent release of drug molecules. While pure DOX shows the rapid release behaviour with $t_{1/2}$ (time needed for the release of 50% of drug) about 45 min, the DOX-CPMN show sustained release profile with $t_{1/2}$ about 5 h. The initial stage of drug release is characterized by a rapid release of drug, followed by a slow, steady and controlled release of drug. It has been observed that about 90% of loaded drug molecules were released from the DOX-CPMN system at pH=5 after 48 h under reservoir-sink conditions at 37°C.

Furthermore, the short time release behaviour of DOX from DOX-CPMN (inset of Fig. 3.7b) shows a linear relationship between the drug release and square root of time ($t^{1/2}$) as anticipated from Higuchi drug release model [196]

$$Q = K_H t^{1/2}$$ ……..........…….(3.3)

where Q is the amount of drug released at time t, K_H is the Higuchi dissolution constant. This confirmed that DOX release followed a diffusion-controlled process. With the pH drop from 7.3 to 5.0, the zeta-potential of CPMN increases which means that the surface of the CPMN becomes less negative. The less negative the surface, the weaker the interactions between the CPMN and DOX. Thus, the release of DOX could be attributed to the weakening of the electrostatic interactions between cationic

DOX and partially neutralized carboxyl groups on the surface of CPMN at acidic pH. This is desirable for cancer therapy as the relatively low pH in tumours will stimulate the DOX release at the target site.
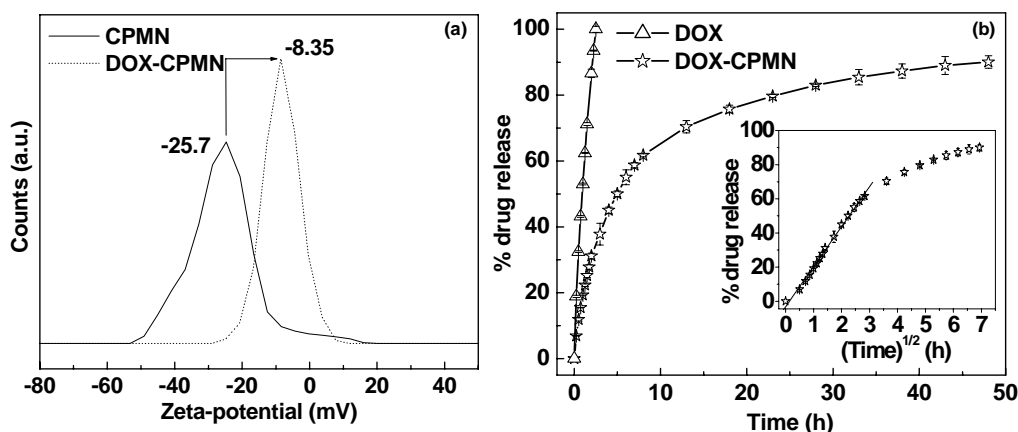
Fig. 3.7. *(a) Zeta-potential distribution plot of 1 mL aqueous suspension of CPMN (100 µg/mL) before and after interaction with 10 µg/mL of DOX and (b) drug release profile of DOX and DOX-CPMN at 37°C (reservoir: pH=5 and sink: pH=7.3).*

3.3.7. Effect of AMF on drug release from CPMN-DOX

In order to see the effect of AMF on drug release, release studies were also carried out at pH=7.3 and pH=5 in presence and absence of AMFs under sink conditions. No significant release of the drug was observed under AMFs as compared to their respective control experiments (Fig. 3.8). Recently, Oliveira et al. [197] observed a significant increase in drug release by exposing hybrid polymersomes (loaded with DOX and iron oxide nanoparticles) to magnetic field and hypothesized that local heating leads to a permeation of the polymersome membrane facilitating DOX release. However, in the present case local heating is not capable of releasing the electrostatically bound drug from the nanocarriers. Furthermore, receptor

molecules having amine-reactive groups can be conjugated to these DOX loaded CPMN for cell specific targeting.
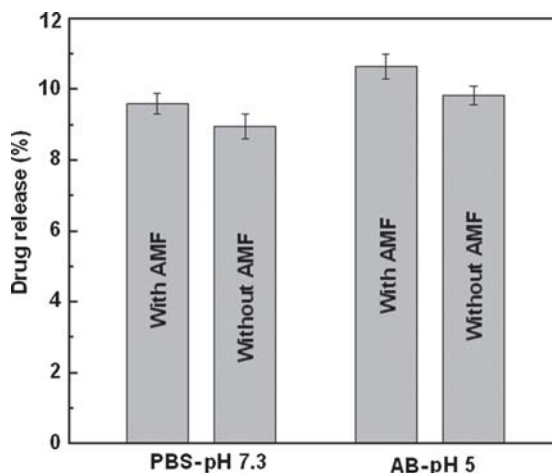
Fig. 3.8. *Release of DOX from DOX-CPMN with and without application of AMF.*

3.3.8. *In-vitro* cytotoxicity studies of CPMN

Having noted the good heating efficacy of CPMN, we had also studied their hyperthermic tumour cell killing efficiency in WEHI-164 tumour cells in presence and absence of AMF (Fig. 3.9). It has been observed that the control cells (untreated) and cells treated with particles only did not show significant change in the percentage cell viability. This indicates that CPMN have negligible cytotoxicity by itself. CPMN under AMF (+ hyperthermia) showed about 10% decreases in cell viability for 1 mg of CPMN. Specifically, this study demonstrated the potential of these Fe_3O_4 NPs for hyperthermia treatment of cancer cells.
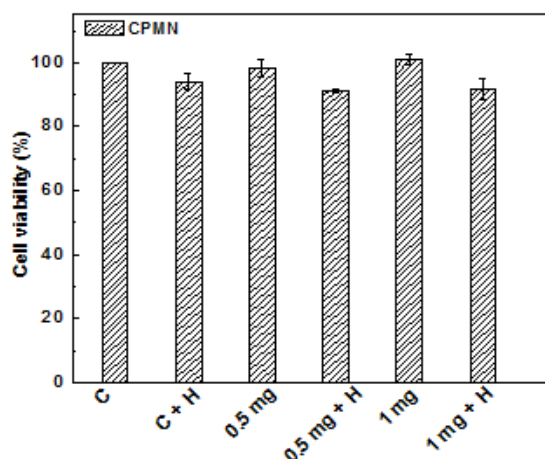
Fig. 3.9. *Effect of magnetic hyperthermia on WEHI-164 cells using different concentration of CPMN along with various control groups (C: untreated cells, C + H: untreated cells under AMF only, 0.5 and 1 mg: treated with CPMN only, 0.5 mg + H and 1 mg + H: treated with CPMN followed by AMF). The AMF of 0.335 kOe was exposed for 10 min under magnetic induction heater. Data are presented as mean ± SD, *P<0.05.*

3.3.9. Hemocompatibility and protein resistance behaviour of CPMN

The drug delivery and magnetic hyperthermia results of CPMN prompted us to explore their hemocompatibility and protein resistance characteristics for further *in-vivo* use. The hemocompatibility of CPMN was assessed by hemolysis assay and the percentage of hemolysis was found to be less than 5% upon incubation of 0.5 mg of CPMN. This low percentage of hemolysis indicates good hemocompatibility of CPMN. We also investigated the interaction of these NPs with BSA protein at physiological medium (0.01 M PBS, pH=7.3). The CPMN did not show any significant change in zeta-potential (Table 3.1) even after incubation with BSA for 2h, revealing their BSA protein resistance characteristics at physiological medium.

However, other factors such as hydrophobic interactions and specific chemical interactions between the protein and NPs also play important roles in addition to electrostatic interactions [187]. Specifically, the present study demonstrated the preparation of aqueous stable carboxyl PEGylated Fe_3O_4 magnetic NPs and investigation of their potential applications in biomedical field.

Table 3.1. *Zeta-potential values of CPMN after interaction with BSA protein.*

CPMN (0.02 mg/mL) in 1 mL of 0.01 M PBS (pH=7.3)	CPMN (0.02 mg/mL) incubated with BSA (0.025 mg/mL) in 1 mL of 0.01 M PBS (pH=7.3)		
	30 min	1 h	2 h
-27.2 mV	-26.9 mV	-26.5 mV	-26.0 mV

3.4. Summary

A soft chemical approach for the preparation of water-dispersible carboxyl PEGylated Fe_3O_4 magnetic nanoparticles (CPMN) is described. The formation of single phase inverse spinel Fe_3O_4 NPs of size about 10 nm is evident from XRD analysis and TEM micrograph. The light scattering measurements indicated the good colloidal stability of CPMN in aqueous and physiological medium. These superparamagnetic nanoparticles has excellent self-heating efficacy under AC magnetic field, thus could be used as an effective heating source for hyperthermia treatment of cancer. It is observed that the AC magnetic field of 0.251 kOe at a frequency of 265 kHz is able to produce energy enough for raising the temperature of the CPMN suspension (1 mg/mL) to hyperthermia temperature within 20 min. Further, these PEGylated nanoparticles showed high loading affinity for anticancer drug (DOX) and their pH dependent sustained release, which make them suitable for

the targeted drug delivery. The free carboxyl group present on CPMN can provide accessible surface for conjugation of various biomolecules/biolabelling for a variety of biomedical applications.

Chapter 4

Polyaniline shell cross-linked Fe$_3$O$_4$ magnetic nanoparticles for heat activated killing of cancer cells

4.1. Introduction

Recently, there has been a growing interest in the fabrication of polymer coated magnetic nanostructures as contrast agents for heat activated killing of cancer cells and targeted drug delivery [198-202]. The magnetic component is responsible for magnetic field induced heating and the polymer counterpart helps in tuning the magnetic response of particle as well as provides active sites for the conjugation of biomolecules, receptors and drugs etc. Thus, site-selective targeting and localized heating of cancer cells can be successfully achieved by using polymer shell cross-linked magnetic nanoparticles [203-209].

In view of above, the polymer coating on Fe_3O_4 nanoparticles must afford colloidal and chemical stability in cellular medium while retaining their optimal magnetic properties for higher heating efficacy. Recently, new developments appeared in designing and synthesis of conducting polymer shell cross-linked magnetic nanoparticles [210-213]. Amongst others, conducting polymers such as polypyrrole and polyaniline have received special attention due to their unique π-conjugated structures, which lead to good environmental stability and high electrical conductivity. Conducting polymers have great potential for use in batteries, electronics, bio- and chemical sensors. Polyaniline (PANI), a highly conducting polymer, has been studied for the immobilization of enzymes, antibodies and nucleic acids. It is also suitable as a substrate for cell attachment and proliferation and possesses excellent biocompatibility *in-vivo*. Bidan et al. [210] demonstrated an electrochemical method to fabricate core-shell nanostructure in which magnetic core is surrounded by anionic complexing polypyrrole shell. Deng et al. [211]

reported the preparation of Fe_3O_4-polyaniline nanoparticles having core-shell nanostructure. Even though many materials and methods are developed for fabrication of conducting polymer shell cross-linked magnetic nanoparticles, but their use in heat activated killing of cancer cells is not much studied.

Herein, we report the preparation of polyaniline impregnated shell cross-linked magnetic nanoparticles by a facile soft-chemical approach. Specifically, the excellent colloidal stability, good self-heating efficacy, high loading affinity for anticancer drug and substantial internalization in tumour cells make these novel NPs suitable for cancer therapy. It is interesting to mention that the polyaniline impregnated shell on MNPs enhances the heat activated killing of cancer cells under AMF.

4.2. Synthesis of polyaniline shell cross-linked magnetic nanoparticles (PSMN)

The polyaniline shell cross-linked magnetic nanoparticles (PSMN) were synthesized by simple and facile two step process, carboxyl PEGylation of Fe_3O_4 nanoparticles followed by cross-linking of polyaniline shell on PEGylated particles (CPMN). Carboxyl PEGylated Fe_3O_4 magnetic nanoparticles (CPMN) were synthesized through co-precipitation of Fe-chlorides precursors in aqueous medium followed by *in-situ* functionalization of PEG-diacid (as discussed in the previous chapter).

In order to provide polyaniline shell on CPMN, 12 mL of 0.1 M aniline hydrochloride was added to 20 mL aqueous suspension of CPMN (1 gm). The above reaction mixture was thoroughly mixed under ultrasonic bath for 15 min followed by mechanical stirring for 30 min. Then, 4 mL potassium peroxodisulfate (0.04 M) was added to initiate the polymerization process and reaction was allowed to proceed for 2 h

under vigorous stirring. The products were thoroughly rinsed with water and separated from the solution using a permanent magnet, and purified by dialysis against milli Q water.

Polyaniline shell was grown on PEG diacid functionalized Fe_3O_4 nanoparticles by polymerization reaction as described in the Fig. 4.1. These CPMN were chosen as the core material for further fabrication of polyaniline shell due to their high negative surface charge and good aqueous colloidal stability.
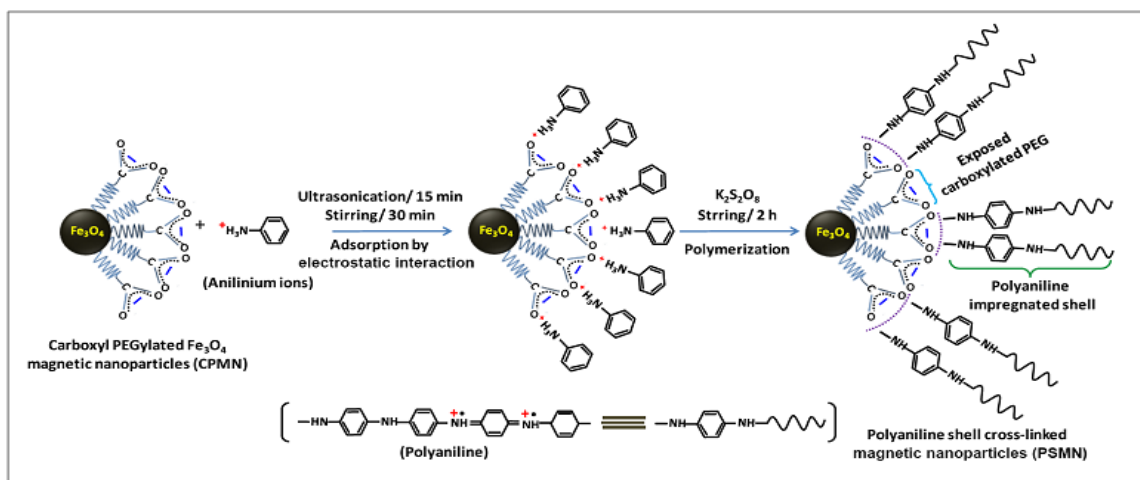
Fig. 4.1. *Schematic representation of the growth of polyaniline shell on carboxyl PEGylated Fe_3O_4 magnetic nanoparticles (CPMN) by polymerization reaction.*

4.3.1. Structural studies of PSMN

The XRD pattern of PSMN (Fig.4.2 a) reveals the formation of highly crystalline single phase cubic inverse spinel Fe_3O_4 nanostructure with an average crystallite size of about 10 nm (σ<10 %). The broad peak representing the periodicity parallel to the polymer chains of PEG and polyaniline were not clearly observed at 2θ around 25° due to

the weak intensity in comparison to the intense diffraction peaks of Fe_3O_4. The lattice constant was found to be ~8.379 Å, which is very close to the reported value of magnetite (JCPDS Card No. 88-0315, a = 8.375 Å). From TEM micrographs of PSMN (Fig. 4.2b), it is evident that Fe_3O_4 NPs are almost spherical in shape with an average size of ~10 nm.
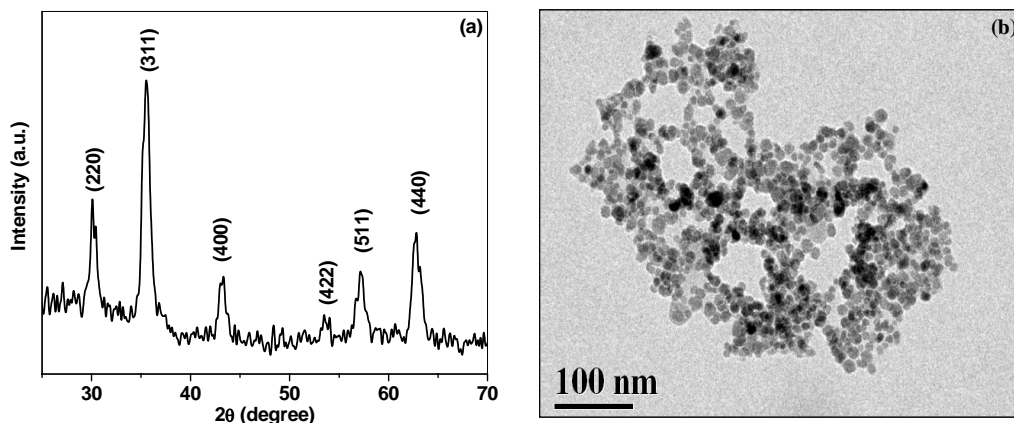
Fig. 4.2. (a) XRD pattern of PSMN, and (b) TEM image of PSMN.

The polyaniline shell cross-linking on the surface of CPMN was investigated by FTIR, DLS, zeta-potential and TGA analysis. Fig. 4.3 shows the FTIR spectra of polyaniline, CPMN and PSMN, with their peak assignments. The absorption bands for the polyaniline are well resolved, but those of the PSMN are rather broad and few. In the FTIR spectrum of PSMN, the appearance of vibrational modes of quinone ring deformation, benzene ring deformation and C-N stretching of a secondary aromatic amine at 1575, 1480 and 1293 cm^{-1}, respectively with slight shifting of band position clearly suggest the successful polymerization of polyaniline onto the surface of the CPMN [214-215]. Furthermore, the appearance of =N$^+$-H stretching mode of polyaniline at about 1120

cm^{-1} in FTIR spectra of PSMN indicate the existence of polyaniline in the form of emeraldine salt, which has high conductivity [215].

The mechanism of formation of polyaniline shell on Fe_3O_4 NPs through *in-situ* polymerization can be explained by invoking an interfacial polymerization process. First, the cationic anilinium ions are adsorbed onto the negatively charged CPMN surface in a close proximity through the formation of $-COO^-\cdots H_3N^+$ ion pairs. This adsorption results in great increase of the local concentration of aniline monomer near the Fe_3O_4 core, which is favourable for the initial polymerization of aniline under low monomer concentration. Moreover, from surface energy considerations, heterogeneous nucleation of polyaniline NPs at the CPMN surface is energetically favoured than homogenous nucleation of polyaniline in the bulk solution. Once the polyaniline nuclei are generated, the polymerization takes place preferentially and continuously on the existing polyaniline on the surface of NPs rather than in solution. Hence, the shell cross-linking via polymerization was successfully initiated, propagated and terminated on the surface of PEGylated Fe_3O_4 resulting a conducting polymer cross-linked nanostructure. In a similar type of study, Jang et al. [214] reported the synthesis of monodisperse silica-polyaniline core-shell NPs by *in-situ* polymerization of aniline monomers adsorbed on the negatively charged silica surface through electrostatic interactions.

However, in present study, one cannot negate the possibility of forming polyaniline impregnated PEG shell, rather than a well separated PEG-PANI interface. This can arise from various reasons such as conformational flexibility of PEG chains which allows penetration of PANI chains, low molecular weight oligomer formation due to low

monomer content and formation of patchy PANI particles on the surface rather than uniform coating. We believe that such composite structure of PANI and PEG could be advantageous for the effective heat transport from Fe_3O_4 core to the surrounding medium. The poor electron density contrast between PEG and PANI does not permit identification of the exact microstructure at the PEG-PANI composite surface.
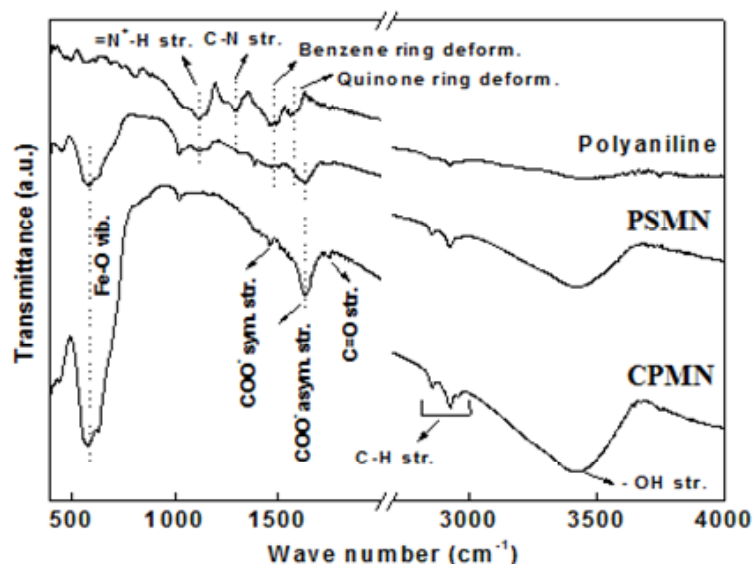
Fig. 4.3. *FTIR spectra of polyaniline, CPMN and PSMN with their peak assignments (pure polyaniline is prepared by similar method in absence of Fe_3O_4 nanoparticles for comparative purpose).*

4.3.2. Thermogravimetric analysis and particle size of PSMN

The thermogravimetric analysis (TGA) of PSMN shows a weight loss of about 7.9%, whereas that of CPMN was 4% (Fig. 4.4a). This result (higher weight loss) clearly supports the organic modification during the formation of polyaniline impregnated shell on the surface of CPMN. An increase in the molecular weight of the organic chains

attached to the Fe_3O_4 nanoparticles, during the growth of the conducting polymer shell, is also manifested from DLS (Fig. 4.4b).
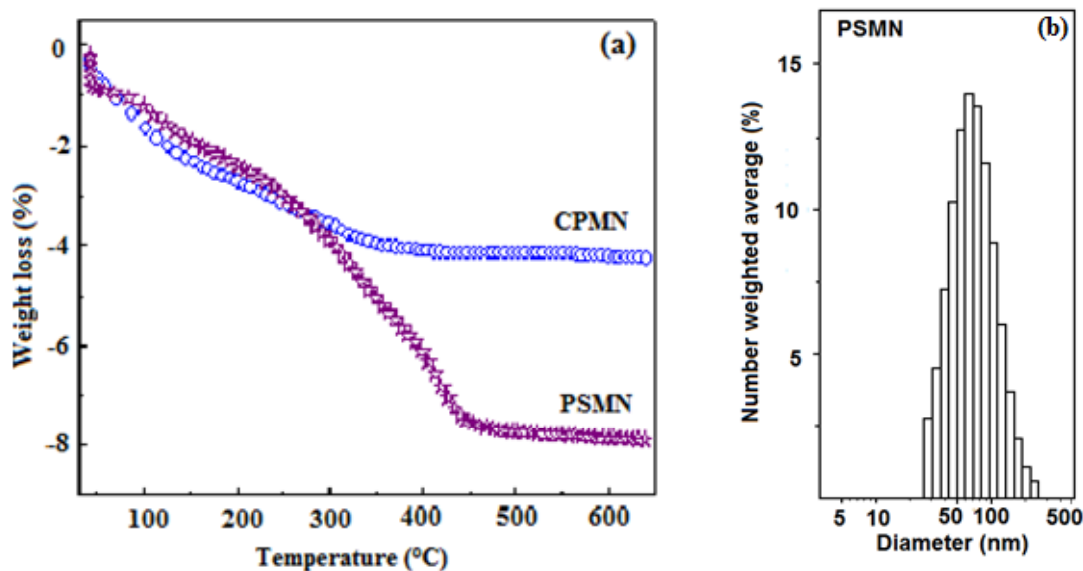
Fig. 4.4. *(a)Thermogravimetric plots of CPMN and PSMN, and (b) DLS plot of PSMN.*

DLS measurements indicate that PSMN show monomodal distribution with mean hydrodynamic diameter of 65 nm (polydispersity index~0.2). The larger hydrodynamic diameter of PSMN as compared to CPMN (40 nm) is primarily due to the presence of associated and hydrated long chain organic layers [56]. As DLS is weighted towards large sizes, the average hydrodynamic diameter could be higher than those obtained from TEM. Further, the average hydrodynamic diameter and polydispersity index hardly varies with time revealing their excellent aqueous colloidal stability.

4.3.3. Colloidal stability studies of PSMN

Fig. 4.5 shows the variation in the zeta-potential of PSMN suspensions at different pH values (0.05 mg/ml). From zeta-potential measurements, the isoelectric point (pH of zero point charge, pH_{pzc}) of PSMN was found to be around 5.46 (for CPMN pH_{pzc} = 5.15). The shifting of zero point charge in case of PSMN shows that there are some chances of surface modifications in comparison to CPMN. Thus, these NPs have net positive surface charge at pH < pH_{pzc} and negative surface charge at pH > pH_{pzc}.
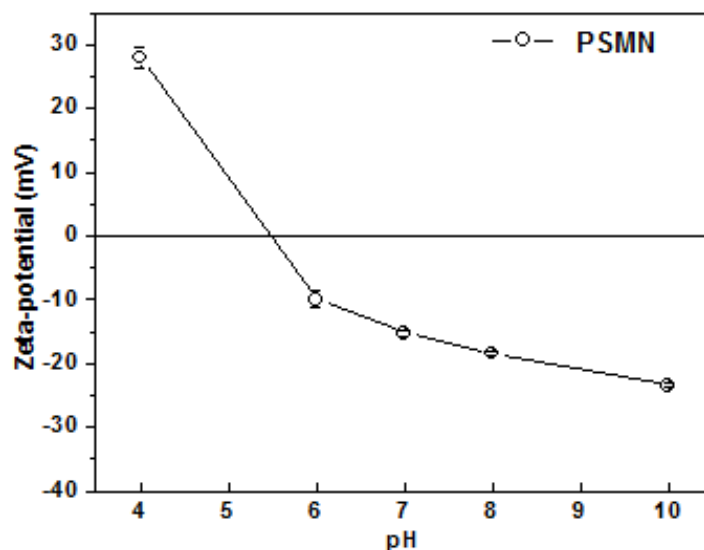
Fig. 4.5. *Variation in the zeta-potential of PSMN suspensions at different pH values (0.05 mg/mL).*

This reversal of charge property may be attributed to the different degree of ionization of functional groups at different pH values. Further, the increase in surface charge (at all measured pH) and shifting of isoelectric point towards higher pH value upon cross-linking of polyaniline shell is possibly due to the creation of positive charges

(=N$^+$-H) on the surface of CPMN [216]. These results further suggest the grafting of polyaniline shell on the surface of PEGylated particles.
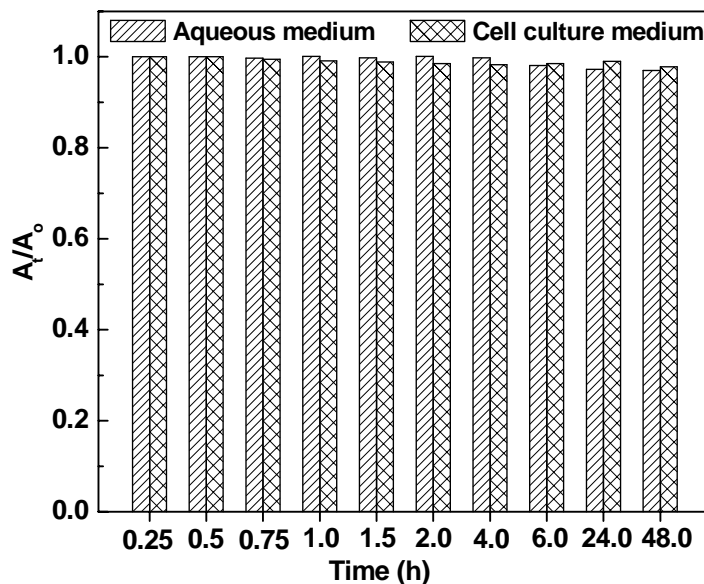
Fig. 4.6. *Normalized UV absorbance (A_t/A_0) vs. time plot of PSMN (0.1 mg/mL) at wavelength of 350 nm in aqueous and cell culture medium (A_t = absorbance at time 't' and A_0 = Absorbance at t = 0).*

The colloidal stability of the PSMN can also be assessed from the changes in light scattering intensity as well as extinction changes with time. The insignificant change in absorbance of PSMN suspensions in aqueous and cell culture (complete DMEM) media indicates their good colloidal stability (Fig. 4.6). These NPs are hydrophilic in nature possibly due to the formation of hydrogen bonds between surface functional groups and water. In addition, the electrostatic repulsive force originating from the ionization of the surface groups provide additional stability to the particles. Furthermore, the negative zeta-potential of PSMN at physiological medium could decrease the possibility of their

combination with hemoglobin, which would play an important role in improving the stability and blood compatibility.

4.3.4. Magnetic properties of PSMN

In order to assess the potential of PSMN in hyperthermia, we have investigated their magnetic and thermomagnetic properties. Fig. 4.7 shows the field dependent magnetization plots of PSMN at 300 K. These particles exhibit superparamagnetic behaviour without coercivity and remanence at 300 K. The saturation magnetization was found to be 63.5 emu/g for PSMN at 20 kOe which is lower than that of CPMN (67.5 emu/g) and it is due to the grafting of polyaniline shell, which directly affects the crystallo-chemical properties of the MNPs surface and leads to an increase in the magnetically disordered surface layer.
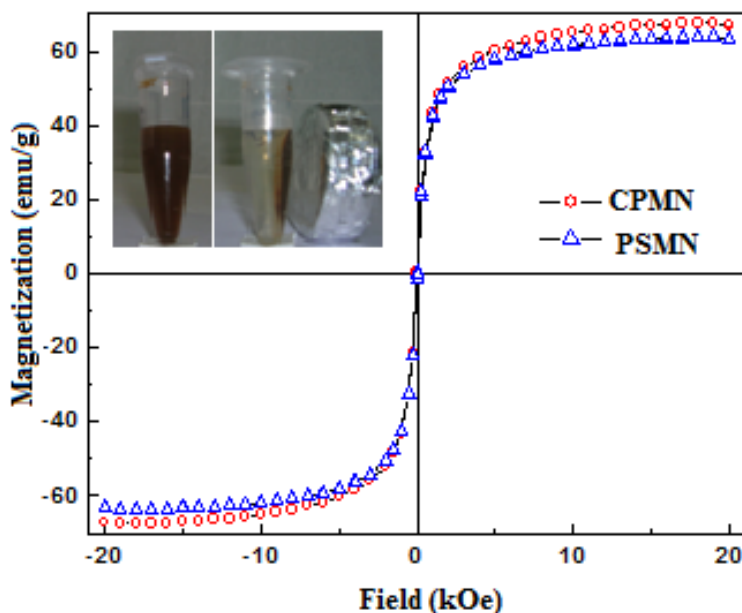
Fig. 4.7. *Field dependent magnetization plots of CPMN and PSMN at 300 K (inset shows the photographs of PSMN in presence and absence of permanent magnet).*

The low value of magnetization of PSMN as compared to bulk Fe_3O_4 (92 emu/g) can be attributed to the combined effect of nano-sized Fe_3O_4 particles (large surface to volume ratio) and robust coating of non-magnetic organic moieties on their surface (quenching of magnetic moment by electron exchange between coating and surface atoms) [23]. However, the retention of superparamagnetic property at room temperature with biocompatible organic shell makes these NPs suitable as effective heating source for hyperthermia treatment of cancer cells.

4.3.5. Thermomagnetic properties of PSMN

Fig. 4.8 shows the temperature *vs.* time plot of aqueous suspension of PSMN at an applied field of 0.335 kOe. It showed a time-dependent gradual increase in temperature of PSMN suspension. Our inductive heating experiments show that a magnetic field of 0.335 kOe at fixed frequency of 265 kHz is able to produce enough energy for raising the temperature of magnetic suspension at a concentration of 1 mg/mL of Fe to $43^{\circ}C$ (hyperthermia temperature) within 15 min. In thermal activation of superparamagnetic Fe_3O_4 NPs under AC magnetic field, an increase in temperature is mainly due to the loss processes during the reorientation of the magnetization (Néel relaxation) or frictional losses with particle rotation in low-viscous environments (Brownian relaxation) [207, 101]. The obtained SAR values of PSMN suspensions are shown in Table 4.1 along with their saturation magnetization at 20 kOe. It has been observed that SAR decreases with increasing the Fe concentration. This may be due to the decrease in Brownian contribution to hyperthermia and increase in magnetic dipole-dipole interactions between NPs in suspension as a result of increase in local concentration [207, 218]. Furthermore, it

has been observed that the SAR values of PSMN are found to be slightly lower than those of CPMN at all concentrations, which is obvious as they possess less magnetic moment.
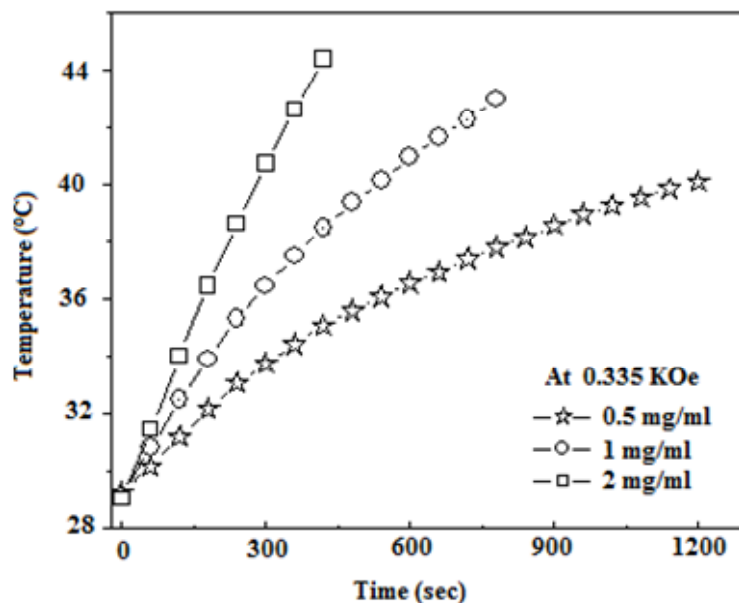
Fig. 4.8. *Temperature vs. time plots of 1ml of aqueous suspension of PSMN at an applied field of 0.335 kOe.*

The rise in temperature was also visualized by the time dependant changes in IR thermograms (Fig. 4.9a-d). The central circle represents the PSMN suspension, which was heated by induction heating unit and demonstrates that the hyperthermia induced by the AMF selectively heated the specific area where the magnetic suspension was placed. The rise in temperature is clearly evident from the changes in colour of the central region of thermograms. The temperature profiles (Fig. 4.9e and f) along the sample zone (marked dotted line in Fig. 4.9c and d) clearly show a sharp decline in temperature at the periphery indicating localized heating of the specimen. This localized heating of magnetic suspension under AMF is necessary for *in-vitro* hyperthermia treatment of cancer cells.
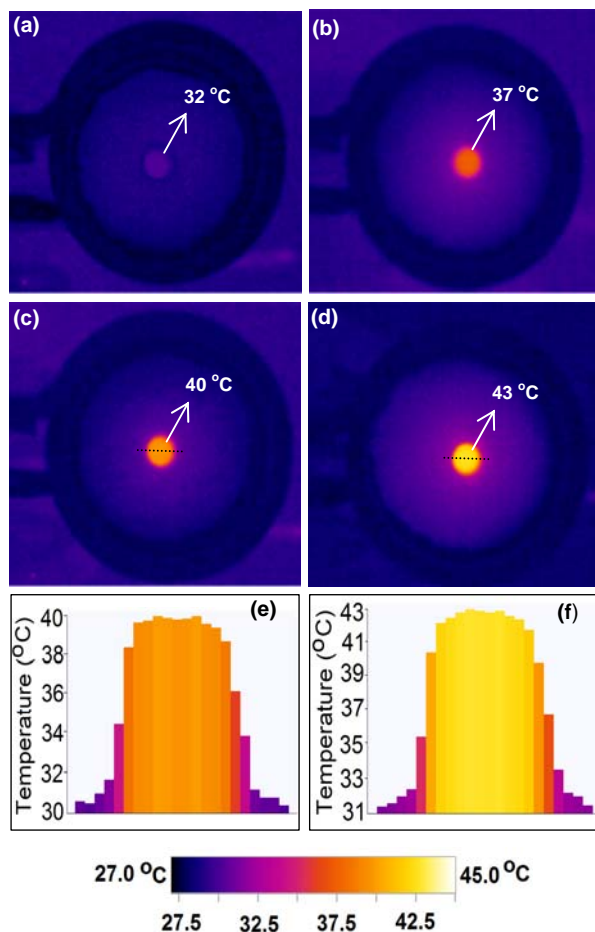
Fig. 4.9. *(a-d) IR thermograms showing the rise in temperature of PSMN suspension during the exposure of AMF of 0.335 kOe (top view of samples) and (e, f) temperature distribution in PSMN suspension along the marked dotted line in Fig. 4.9 (c) and (d), respectively.*

4.3.6. Cytotoxicity studies of PSMN

Having noted the good heating efficacy of both CPMN and PSMN, we have also studied their hyperthermic tumour cell killing efficiency in WEHI-164 tumour cells in presence and absence of AMF (Fig. 4.10). It has been observed that the control cells (untreated) and cells treated with particles only (without AMF) did not show significant

change in the percentage cell viability. This indicates that both CPMN and PSMN (CPMN is shown for the sake of comparison) have negligible cytotoxicity by itself. However, it is worth mentioning that PSMN under AMF (with AMF) showed about 22.5% decrease in cell viability for 1 mg of PSMN as compared to the marginal (~8%) decrease with CPMN under similar condition. This may be explained on the basis of the surface charge of these particles in culture medium. The zeta-potential of CPMN and PSMN in culture medium were found to be -15 and -8 mV, respectively. The PSMN having higher surface charge (less negative) may have higher affinity for WEHI-164 cells as compared to CPMN. Recently, Motskin et al. [219] studied the uptake of negatively charged hydroxyapatite (HAP) nanoparticles by human monocyte-macrophage cells and observed that the HAP nanoparticles with higher zeta-potential value (less negative) showed greater uptake. These cytotoxicity results were also supported by alterations in cellular morphology (cell detachment and circularization) and a decrease in cell number as visualized by optical microscopy (Fig. 4.11).

Table 4.1. *The obtained SAR values of PSMN suspensions at different concentrations along with their saturation magnetization (M_{max}) at 20 kOe.*

Magnetic suspensions	M_{Max} (emu/g)	SAR (W/g of Fe) at different concentrations (in terms of Fe) under AMF of 0.335 kOe		
		0.5 mg/mL	1 mg/mL	2 mg/mL
PSMN	63.5	120	100	80
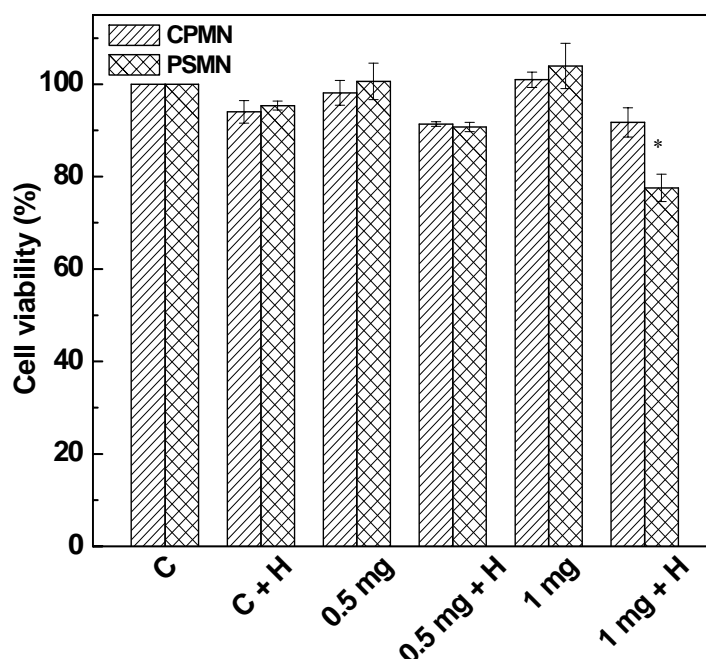
Fig. 4.10. *Effect of magnetic hyperthermia on WEHI-164 cells using different concentration of CPMN and PSMN along with various control groups (C: untreated cells, C + H: untreated cells under AMF only, 0.5 and 1 mg: treated with CPMN only, 0.5 mg + H and 1 mg + H: treated with CPMN followed by AMF). The AMF of 0.335 kOe was exposed for 10 min under magnetic induction heater. Data are presented as mean ± SD, *P<0.05.*

From the images of cancer cells treated with 1 mg of PSMN and AMF (1 mg + H), it is evident that there is significant death of cells via apoptosis. However, further investigations are required to understand the exact mechanism of cell death by PSMN under exposure of AMF. Specifically, this study demonstrates the potential of polyaniline shell cross-linked Fe_3O_4 nanoparticles for hyperthermia treatment of cancer cells.
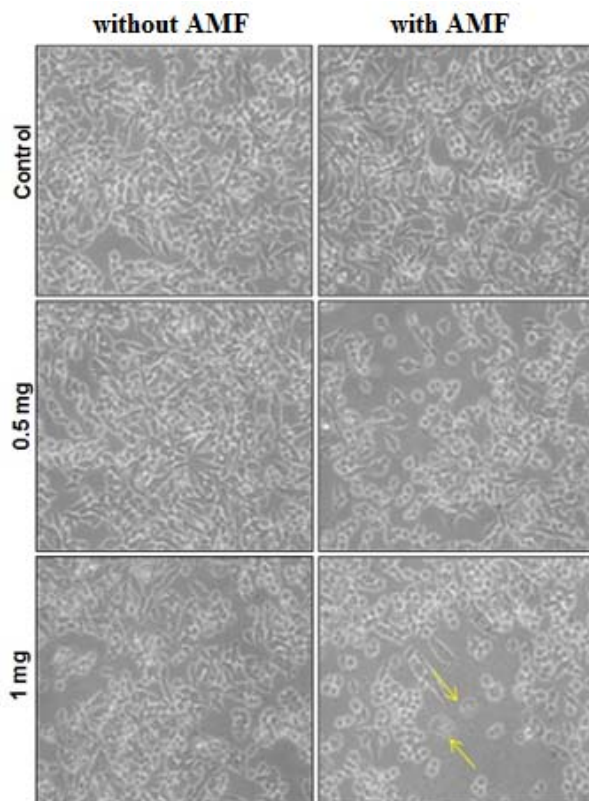
Fig. 4.11. *Optical microscopy images of WEHI-164 cells taken 48 h after the treatment of PSMN with and without exposure of AMF (Magnification: 200 X). Arrows indicate the cells undergoing apoptosis.*

4.3.7. Drug loading and drug release profile of DOX-PSMN

About 60% drug-loading efficiency (w/w) was obtained upon incubating 0.5 mL of aqueous solution of DOX (1 mg/ml) with 2.5 mL of the aqueous suspension of PSMN (5 mg) for 1h in dark at room temperature. Further, the zeta-potential of the PSMN (100 µg/mL suspension) increased from -24.0 mV to -5.0 mV upon incubating with an aqueous solution of 10 µg/mL of DOX. This increase in surface charge arises from the binding of cationic DOX (protonated primary amine present on the drug induces a positive charge)

with negatively charged nanoparticles (PSMN) predominately through electrostatic interactions. The affinity of DOX for negatively charged molecules has been the subject of numerous earlier investigations [194, 220].

The release of drug molecules from DOX-PSMN (Fig. 4.12a) follows a time dependent sustained release profile. Furthermore, the short time behaviour (Fig. 4.12b) shows a linear relationship between the drug release and square root of time ($t^{1/2}$) as expected from Higuchi drug release model confirming that the DOX release process is diffusion-controlled [196]. It is interesting to observe from the release profiles that the release rate of DOX is higher at lower pH. This is desirable for cancer therapy as the relatively low pH in tumours will specifically stimulate the DOX release in the target site. The pH triggered release of DOX could be attributed to the weakening of the electrostatic interactions between the drug and PSMN.
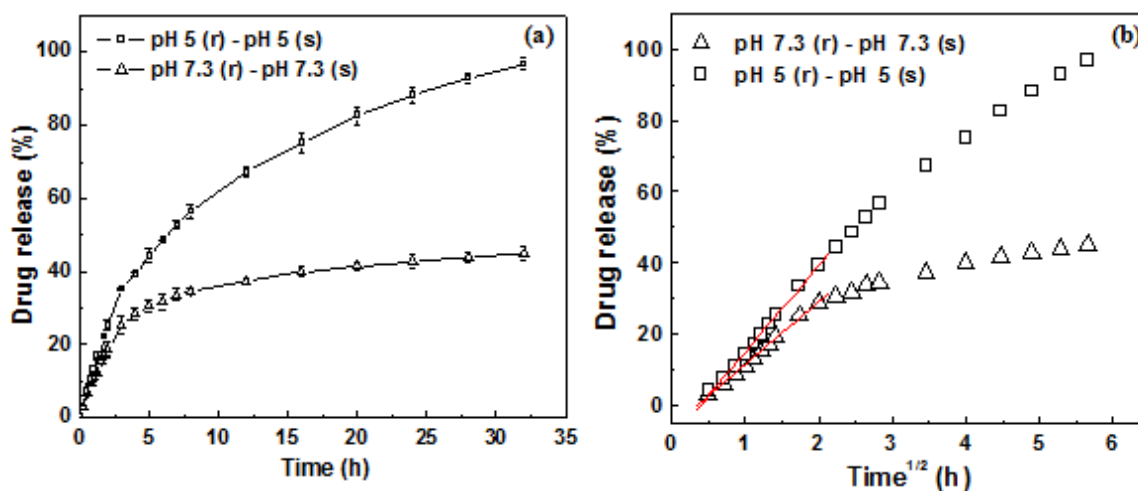
Fig. 4.12. (a) pH dependent drug release profile of DOX-PSMN in cellular mimicking environment at $37^{o}C$ and (b) their short time release behaviour showing linear relationship between the drug release and square root of time.

4.3.8. Cellular uptake studies of DOX-PSMN

The results obtained from drug release studies prompted us to explore the cellular uptake of PSMN by cancer cells. Fig. 4.13 shows the CLSM images of WEHI-164 cells after incubation with the DOX and DOX-PSMN at culture conditions. A significant uptake of DOX-PSMN was clearly observed from the red fluorescence image arising from DOX emissions, suggesting that the drug loaded NPs were internalized in the cells.
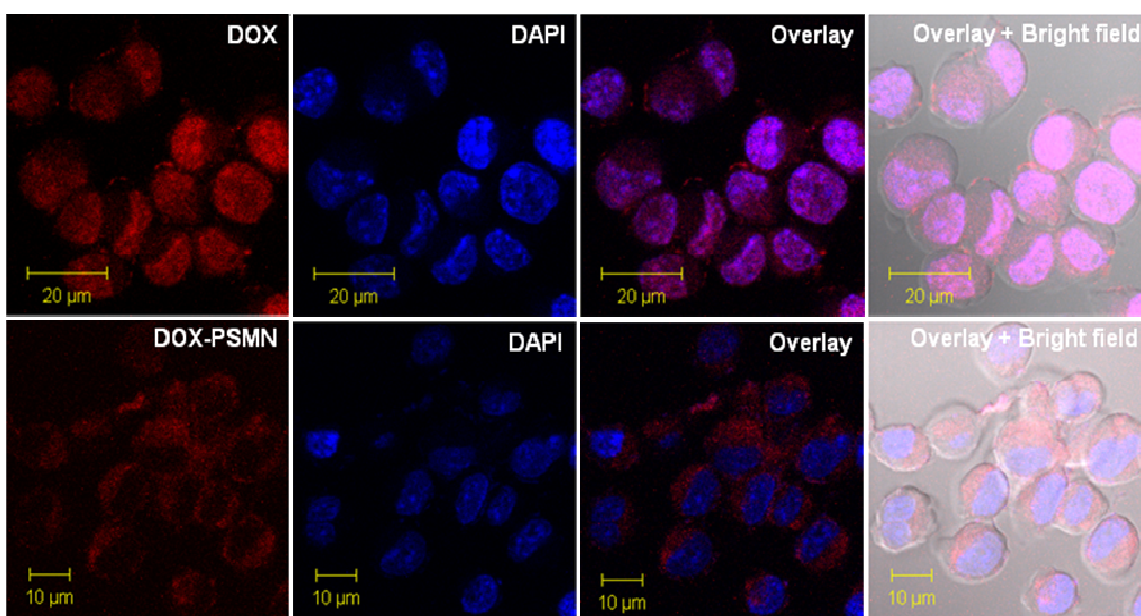
Fig. 4.13. Confocal microscopy images of WEHI-164 cells after incubation with the DOX, DOX-PSMN and DAPI at culture conditions (Top row: treated with pure DOX and DAPI, Bottom row: treated with DOX-PSMN and DAPI).

The blue fluorescence image shows emission from nucleus stained with DAPI. The merged image of DOX and DAPI fluorescence (as seen by the magenta colour) clearly indicates that pure DOX is co-localized in nucleus, whereas DOX-PSMN is mainly

localized in the cytoplasm. This study demonstrates that the use of these NPs as drug delivery vehicles could significantly enhance the accumulation of drug (DOX) in target cancer cells leading to a high therapeutic efficacy.

4.3.9. Thermo-optical studies of PSMN

The presence of polyaniline shell can improve the optical absorption of visible light of appropriate wavelength, depending on the structure of the polyaniline. The strong optical absorption of polyaniline can be exploited for laser induced heating of tumour cells as well. Towards this end, we performed thermal imaging experiments on solid PSMN after exposing to laser light of 532 nm. The infrared thermal images indicate local heating of particles by absorption of light and the temperature increases with an increase in exposure time (Fig. 4.14).
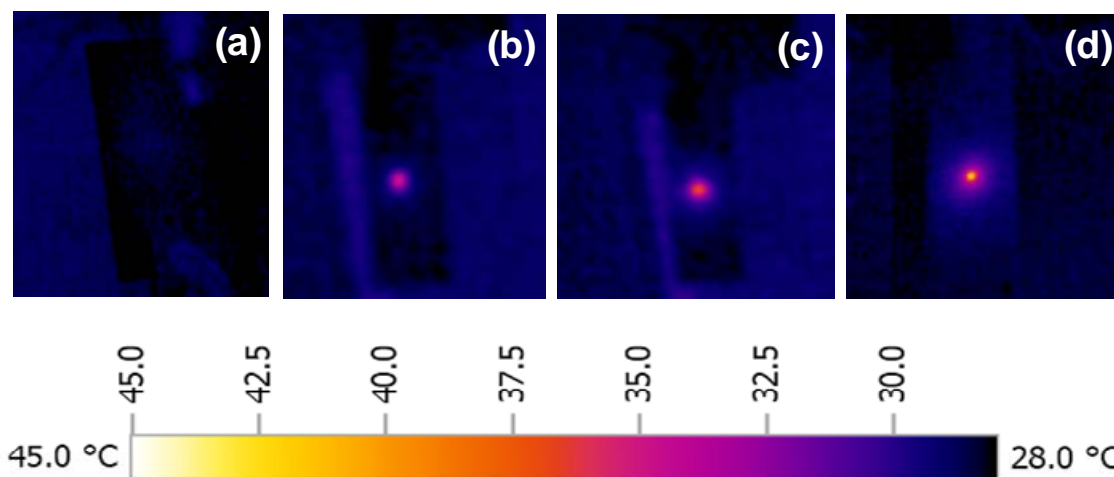
Fig. 4.14. Infrared thermal images of solid PSMN after exposing to laser light of 532 nm at different interval of time (a) 0 min, (b) 4 min, (c) 8 min and (d) 12 min (centre circle indicates the location of samples mounted on the glass slide).

4.3.10. Hemocompatibility and protein resistance behaviour of PSMN

The magnetic hyperthermia, drug delivery and cellular internalization results of PSMN prompted us to explore their hemocompatibility and protein resistance characteristics for further *in-vivo* use. The hemocompatibility of PSMN was assessed by hemolysis assay and the percentage of hemolysis was found to be 3% upon incubation of 0.5 mg of PSMN. This low percentage of hemolysis (<5%) indicates the good hemocompatibility of PSMN. We also investigated the interaction of these NPs with BSA protein at physiological medium (0.01 M PBS, pH 7.3). The PSMN do not show any significant change in zeta-potential even after incubation with BSA for 2h, revealing their protein resistance characteristics at physiological medium (Table 4.2). Specifically, our PSMN showed high drug (DOX) loading capacity, sustained drug release profile and excellent cellular internalization with good heating efficacy under AC magnetic field, which make the formulation suitable for the targeted drug delivery as well as hyperthermia treatment of cancer.

Table 4.2. Zeta-potential values of PSMN after interaction with BSA protein.

PSMN (0.02 mg/mL) in 1 mL of 0.01M PBS (pH 7.3)	PSMN (0.02 mg/mL) incubated with BSA (0.025 mg/mL) in 1 ml of 0.01 M PBS (pH 7.3)		
	30 min	1 h	2 h
-22.5 mV	-22.3 mV	-21.9 mV	-21.8 mV

4.4. Summary

Conducting polymer (polyaniline) impregnated shell cross-linked magnetic (Fe_3O_4) nanoparticles has been successfully prepared by a facile soft-chemical approach. The formation of single phase inverse spinel Fe_3O_4 NPs of size about 10 nm is observed from XRD analysis and TEM micrograph. FTIR spectra, DLS, TGA, zeta-potential and magnetic measurements clearly show the growth of polyaniline shell on the surface of carboxyl PEGylated Fe_3O_4 nanoparticles. These NPs show good colloidal stability, high loading affinity for anticancer drug, sustained drug release profile, magnetic field induced heating, and substantial cellular internalization. It is interesting to mention that the polyaniline impregnated shell on PEGylated Fe_3O_4 nanoparticles enhances the heat activated killing of cancer cells under magnetic field. Specifically, the present study highlights the effectiveness of the hyperthermia treatment mediated by the use of conducting polymer shell on magnetic nanoparticles.

Chapter 5

Biocompatible phosphate anchored Fe$_3$O$_4$ magnetic nanocarriers for drug delivery and hyperthermia

5.1. Introduction

Now-a-days, there is a growing interest in developing biocompatible magnetic nanocarriers with suitable surface functionality for intracellular drug delivery and hyperthermia [56, 106, 184, 192, 208, 221, 222]. Although many molecules such as organic ligands, surfactants, polymers, dendrimers, silica and gold coating are widely used to stabilize Fe_3O_4 suspensions [156, 183, 216, 223-225], the literature on use of bioactive phosphonates and phosphates on nanoparticle surfaces is not much reported. The phosphonates and phosphates have a strong affinity towards transition metal oxide surfaces, especially for those containing tantalum, aluminium, cerium and iron oxide [226-234]. For instance, Yee *et al.* reported the adsorption of alkanephosphonic acids on the surface of amorphous ferric oxide particles and proposed two possible bonding schemes for the phosphonate ions on Fe^{3+}, i.e., one O or two O atoms of the phosphonate group binding onto the surface [227]. Sahoo *et al.* reported the formation of strong P-O-Fe bonding on the surface of alkyl phosphonates and phosphate coated Fe_3O_4 NPs [229]. Lamanna *et al*. [234] developed dendrons having phosphonate head groups and grafted them to the surface of iron oxide nanoparticles. These dendronized iron oxide NPs were shown to have enhanced MRI contrast properties compared to polymer-coated iron oxides nanoparticles. Moreover, these functionalized phosphonate and phosphate seems to have an acceptable biocompatibility and thus, they can serve as potential alternatives to fatty acids as coating agents for metal oxide surface [229, 235]. Recently, sodium hexametaphosphate (SHMP) a food additive, is widely used as a stabilizer for generation of various nanoparticles such as Au, $BaSO_4$, ZnCdS and $ZnS:Cu^{2+}$ etc. [236-239]. The oral toxicity limit of SHMP is 3053 mg kg^{-1} and therefore, its use as a stabilizer in the generation of NPs is safe. However, there is

hardly any report on the use of SHMP as a stabilizer in preparation of aqueous-stable Fe_3O_4 nanoparticles.

Herein, we report the development of bioactive phosphate anchored Fe_3O_4 magnetic nanocarriers having good colloidal stability, magnetic responsivity and specific absorption rate. This interfacial modification of nanoparticles allows us to create functionalized exteriors with high densities of phosphate moieties for conjugation of drug molecules. Specifically, high loading affinity for doxorubicin with their sustained release profile, self-heating capacity, low toxicity and protein resistance characteristic makes these novel NPs suitable for drug delivery as well as hyperthermia treatment of cancer.

5.2. Synthesis of phosphate anchored Fe_3O_4 magnetic nanoparticles (PAMN)

PAMN were prepared by *in-situ* functionalization of Fe_3O_4 NPs with SHMP during co-precipitation of Fe^{2+} and Fe^{3+} ions in basic medium. SHMP was chosen as the coating material due to its low toxicity and immunogenicity.

To synthesize PAMN, 5.406 g of $FeCl_3.6H_2O$ and 1.988 g of $FeCl_2.4H_2O$ were dissolved in 80 mL of water in a round bottom flask and temperature was slowly increased to $70^{o}C$ under nitrogen atmosphere with constant stirring. The temperature was maintained at $70^{o}C$ for 30 min and then 30 mL of 25% ammonia solution was added instantaneously to the reaction mixture, and kept for another 30 min at $70^{o}C$. Then, 10 mL aqueous solution (0.2 gm/mL) of sodium hexametaphosphate (SHMP) was added and temperature was slowly raised upto $90^{o}C$ under reflux and reacted for 60 min with continuous stirring for functionalization of Fe_3O_4 NPs with phosphate molecules. The obtained black coloured precipitates were then thoroughly rinsed with

water and separated from the supernatant using a permanent magnet (field strength ~ 2.5 kOe).

5.3.1. Structural studies of PAMN

Fig. 5.1 shows (a) XRD pattern and (b) TEM micrograph of PAMN. The XRD pattern reveals the formation of single-phase Fe_3O_4 inverse spinel structure with lattice constant, a = 8.377 Å, which is very close to the reported value of magnetite (JCPDS Card No. 88-0315, a = 8.375 Å). The presence of sharp and intense diffraction peaks confirmed the formation of highly crystalline nanoparticles. The average crystallite size of NPs is found to be around 10 nm from X-ray line broadening using the Scherrer formula.

TEM micrograph of PAMN clearly shows the formation of roughly spherical Fe_3O_4 NPs of size about 10 nm. The selected area electron diffraction pattern (inset of Fig. 5.1b) also confirmed the high crystallinity of PAMN. It can be indexed to highly crystalline reflections, such as (220), (311), (400), (422), (511) and (440) of cubic inverse spinel Fe_3O_4 structure, which is consistent with the XRD result.

Fig. 5.2 shows the FTIR spectra of SHMP and PAMN along with their peak assignments. The IR bands for the pure SHMP are well resolved, but those of the PAMN are rather broad and a few. The strong IR band observed at around 577 cm^{-1} in PAMN can be ascribed to the Fe-O stretching vibrational mode of Fe_3O_4. The broad IR spectrum observed in the range of 800 to 1220 cm^{-1} with band at 915, 1030, 1090 and 1175 cm^{-1} in PAMN can be assigned to P-O$^-$ vibrations of SHMP [240-241]. Further, the IR bands observed at around 1400 cm^{-1} and shoulder at 710 cm^{-1} can be associated with P=O and P-O-P stretching vibrations, respectively [241]. These results clearly suggested the successful anchoring/grafting of phosphate groups of SHMP

onto the surface of Fe_3O_4 nanoparticles. The bending and stretching vibrational modes of absorbed H_2O molecules are appeared at 1630 and 3400 cm^{-1}, respectively.
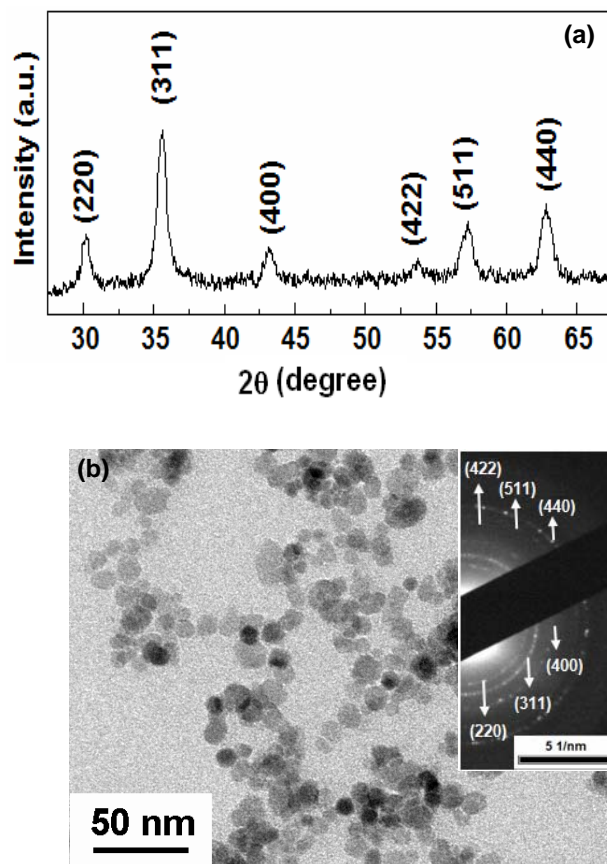
Fig. 5.1. *(a) XRD pattern, and (b) TEM micrograph of PAMN (inset of Fig. 5.1b shows its selected area electron diffraction pattern).*

5.3.2. Thermogravimetric analysis (TGA) of PAMN

Fig. 5.3 shows TGA plots of bare Fe_3O_4 MNPs and PAMN (bare Fe_3O_4 MNPs were prepared in similar method as PAMN without using SHMP as coating material). The TGA curve of bare MNPs shows weight loss over the temperature range from 40°C to 600°C is about 2.8 %. This might be due to the loss of residual water and absorbed hydroxyl groups on the surface of Fe_3O_4 NPs due to aqueous media

synthesis. The observed higher weight loss (6.0 %) in case of PAMN can be ascribed to the removal of physically attached water and chemically attached phosphate molecules on the surface of Fe_3O_4 nanoparticles. Therefore, TGA analysis confirmed the presence of organic molecules on the surface of Fe_3O_4 nanoparticles.
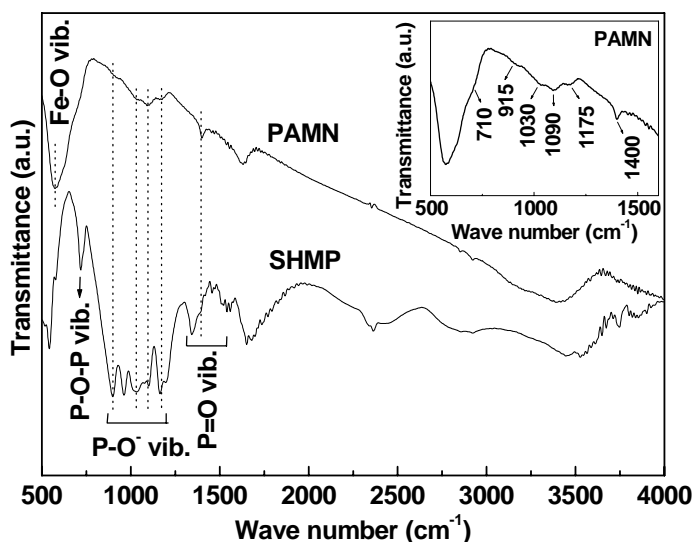
Fig. 5.2. *FTIR spectra of SHMP and PAMN along with their peaks assignment (inset shows the expanded FTIR spectrum of PAMN in the range of 500–1600 cm^{-1}).*

5.3.3. Zeta-potential measurements and stability assay of PAMN

Fig. 5.4 shows the zeta-potential (ζ) measurements of PAMN at different pH. The surface of PAMN shows negatively charged and pH of zero point charge (pH$_{PZC}$) was not observed in the measured pH range. However, the negative surface charge decreases with decrease in pH of the medium. This variation in surface charge may be attributed to the degree of ionization of functional groups (phosphate moieties) associated with Fe_3O_4 NPs at different pH.
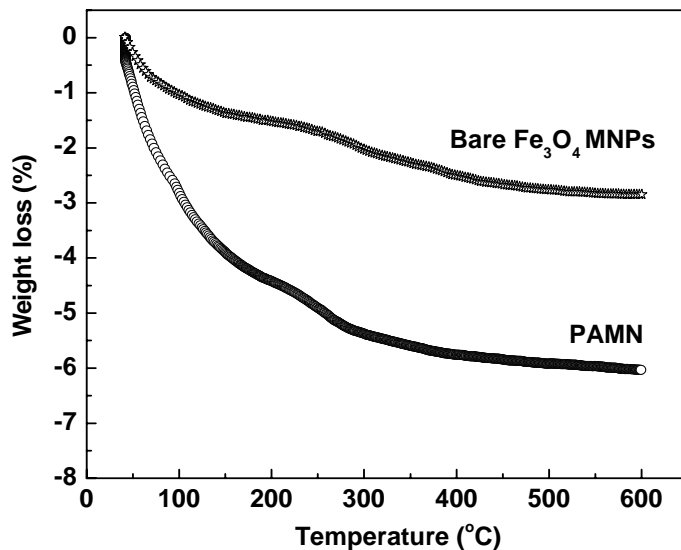
Fig. 5.3. *TGA plots of bare Fe₃O₄ MNPs and PAMN.*
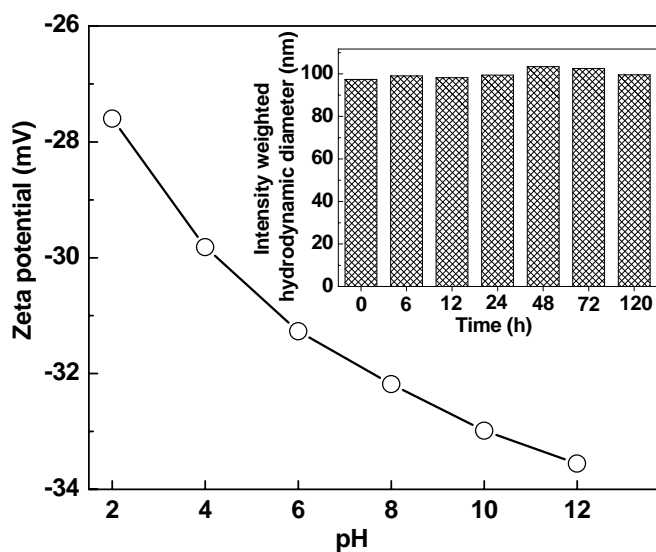
Fig. 5.4. *Zeta-potential (ζ) measurements of PAMN at different pH (inset shows the variation of intensity weighted (z-average) hydrodynamic diameter of PAMN as a function of time).*

DLS measurement (inset of Fig. 5.4) indicates that these samples render aqueous colloidal suspension with intensity weighted (z-average) hydrodynamic diameter of about 100 nm due to the presence of associated and hydrated organic layers [56, 242].

The observed higher hydrodynamic diameter could also arise from the polydispersity of the nanoparticles. As DLS is weighted towards large sizes, the average diameter could be higher than those obtained from TEM. However, the average hydrodynamic diameter hardly varies with time revealing their good aqueous colloidal stability (inset of Fig. 5.4).

The structure of SHMP consists of six phosphate anions, which are linked to each other to form a ring-like structure, with each phosphate group linked to one sodium atom outside the ring. Specifically, some of the phosphate groups of SHMP strongly coordinate to iron cations on the Fe_3O_4 surface to form a robust coating, while the remaining functionalized exteriors of PAMN extend into the water medium, conferring a high degree of aqueous colloidal stability to Fe_3O_4 nanoparticles. In addition to this, the electrostatic repulsive force originating from the ionization of the surface groups also provide stability to the nanoparticles.
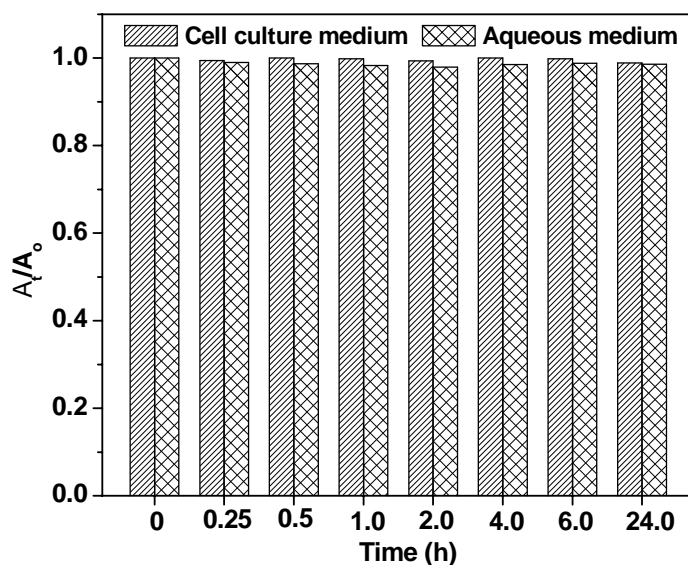
Fig. 5.5. *Variation in normalized absorbance of PAMN in aqueous and cell culture media at different time intervals.*

Furthermore, the highly negative values of zeta-potential of PAMN in 1 % NaCl (ζ = -20 mV) and 0.01 M PBS, pH 7.3 (ζ = -25 mV) indicate their excellent stability in physiological medium. The colloidal stability of the PAMN was also assessed from the changes in absorbance of PAMN suspensions. The insignificant change in absorbance of PAMN suspension (0.1 mg/mL) in aqueous and cell culture (DMEM + 10% FBS) media with time indicates their good colloidal stability (Fig. 5.5).

5.3.4. Magnetic measurements of PAMN

In order to assess the potential of PAMN in targeted drug delivery and hyperthermia, we have investigated their magnetic field responsivity and heating efficacy under AC magnetic field. Fig. 5.6 shows the field dependent magnetization (M vs. H) plots of PAMN at 5 and 280 K. At 280 K, PAMN exhibit superparamagnetic behaviour without magnetic coercivity and remanence, whereas ferromagnetic behaviour with a coercivity of about 200 Oe is observed at 5 K. This transition from superparamagnetic behaviour at high temperature to ferro or ferrimagnetic behaviour below, the so-called blocking temperature is typically observed in MNPs [12].

The ZFC–FC plot (inset of Fig. 5.6) shows that the blocking temperature (T_B) of the PAMN is 130 K at an applied field of 400 Oe. The saturation magnetizations (at an applied field of 6 kOe) of PAMN were found to be 47.8 and 55 emu/g at 280 and 5 K, respectively. It has been observed that the room temperature magnetization of PAMN was reduced to about 52 % of the bulk Fe_3O_4 (92 emu/g). This decrease in magnetization can be attributed to the combined effect of nano size of core Fe_3O_4 particles (large surface to volume ratio) and robust coating of SHMP molecules on

their surface (quenching of magnetic moment by electron exchange between coating and surface atoms) [217]. However, the retention of superparamagnetic property at room temperature with good magnetic field responsivity makes these NPs suitable for drug delivery and hyperthermia applications.
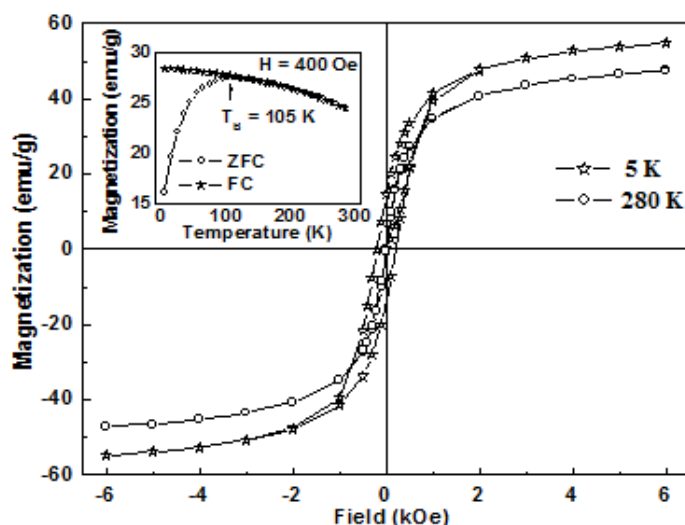
Fig. 5.6. *Field M vs. H plots of PAMN at 5 and 280 K and inset shows their ZFC-FC plot at an applied field of 400 Oe).*

5.3.5. Specific absorption rate (SAR) measurements of PAMN

The temperature *vs.* time plots of PAMN suspension showed a time-dependent gradual increase in temperature under AC magnetic fields (Fig. 5.7). It has been observed that a magnetic field of 0.251 kOe at fixed frequency of 265 kHz is able to produce energy enough for raising the temperature of the magnetic suspension of 1 mg/mL to 42-43°C within 20 min. Further, the time required to reach 43°C decreases with an increase in field strength, which is obvious as the heat generation/dissipation (*P*) is proportional to the square of applied AC magnetic field (inset of Fig. 5.7) [102, 243].
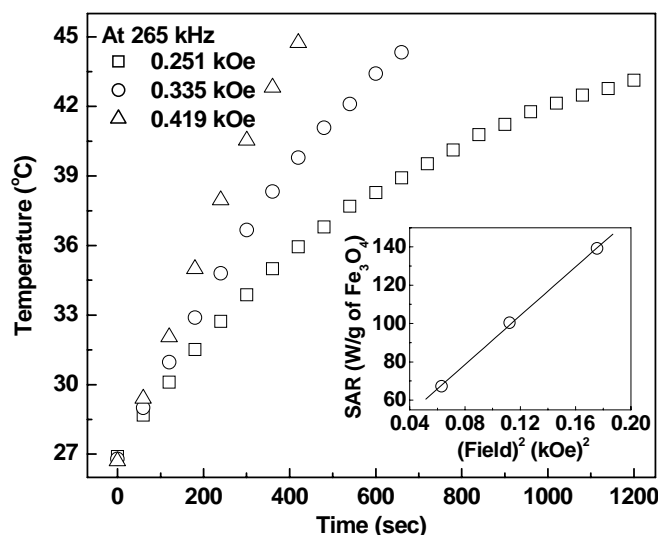
Fig. 5.7. *Temperature vs. time plots of 1 mL aqueous suspension of PAMN (1 mg/mL of Fe) at different applied field (inset shows the linear relationship between SAR and square of the applied AC magnetic field).*

In order to elucidate that the rise in temperature is mainly due to the presence of PAMN under AMF but not from applied AMF alone, we have carried out control experiments, where water solution (without PAMN) were exposed to AMF under similar conditions. It has been observed that AMF alone was not significantly heating the water .Temperature was raised only to 29.7 and 32.8^{o}C even after 20 min exposure of AMF of 0.251 and 0.335 kOe, respectively.(Fig. 5.8).

In thermal activation of Fe$_3$O$_4$ NPs under AC magnetic field, an increase in temperature is mainly due to the combined effect of Néel and Brownian relaxations [243-246]. The SAR values of PAMN were found to be 67.3, 100.5 and 139.2 W/g of Fe$_3$O$_4$ with an applied field of 0.251, 0.335 and 0.419 kOe, respectively.
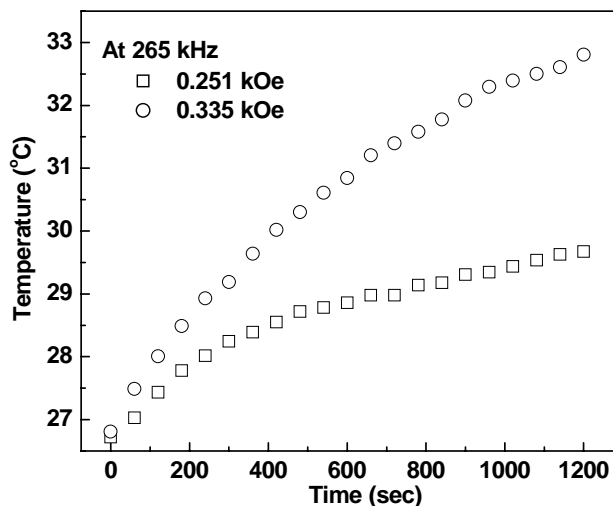
Fig. 5.8. *Temperature vs. time plots of 1 mL water at different applied field.*

5.3.6. Zeta-potential measurements and drug-particle interaction of PAMN

Fig. 5.9 shows the (a) zeta-potential of 1 mL aqueous suspension of PAMN (100 µg/mL) before and after interaction with 10 µg/mL of DOX and (b) fluorescence spectra of 1 mL aqueous solution of pure DOX (10 µg/mL) before and after interaction with different amount of PAMN. The zeta-potential of PAMN suspension (100 µg/mL) increased from -30 mV to -10 mV upon incubating with an aqueous solution of 10 µg/mL of DOX. This increase in zeta-potential arises from the binding of cationic DOX (protonated primary amine present on DOX induces a positive charge) with negatively charged PAMN by forming DOX-PAMN system predominately through electrostatic interactions. The affinity of DOX for negatively charged molecules such as carboxylate ions and phospholipids has been subject of numerous earlier investigations [156, 184, 194, 247].

The interaction of DOX molecules with PAMN was also evident from the decrease in fluorescence intensity of the supernatant liquid after removal of DOX bound PAMN through magnetic separation (Fig. 5.9b). Furthermore, the fluorescence

intensity of supernatant liquid decreases with increasing the concentration of PAMN, which is obvious due to the increase in loading efficiency of DOX onto the surface of PAMN. It has been observed that the loading efficiency (inset of Fig. 5.9b) is strongly dependent on the weight ratio of PAMN to DOX and a drug loading efficiency (w/w) of about 82% is achieved at PAMN to DOX weight ratio of 14 (no significant increase in loading efficiency is observed above this ratio). It is worth mentioning that PAMN still preserve good dispersibility after being coupled with DOX molecules (variation of intensity average diameter of DOX loaded PAMN as a function of time, Fig. 5.10).
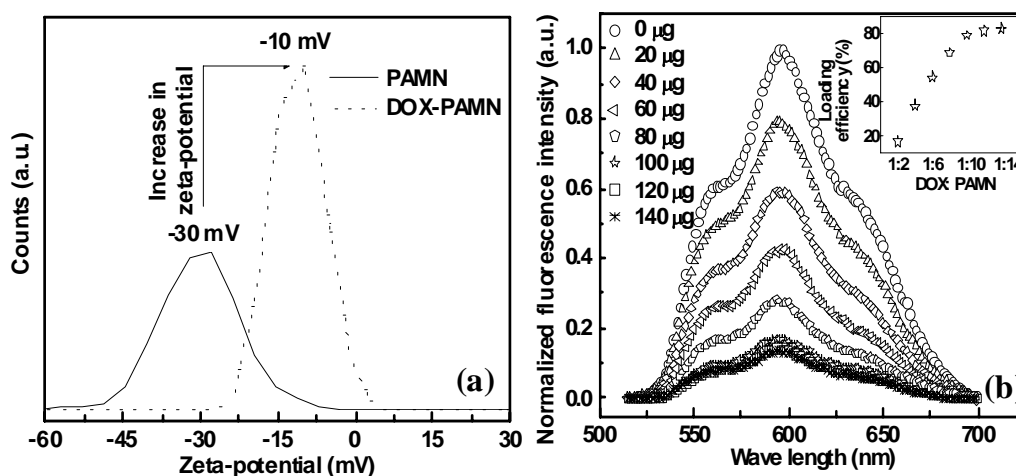
Fig. 5.9. *(a) Zeta-potential of 1 mL aqueous suspension of PAMN (100 µg/mL) before and after interaction with 10 µg/mL of DOX and (b) fluorescence spectra of 1 mL aqueous solution of pure DOX (10 µg/mL) before and after interaction with different amount of PAMN (inset of Fig. 5.9b shows the loading efficiency of DOX onto PAMN after considering the washed drug molecules for calculations).*

5.3.7. Drug loading and drug release of PAMN

Drug release profiles of pure DOX and DOX loaded PAMN were investigated under reservoir-sink condition (reservoir: pH=5 and sink: pH=7.3) at a temperature of

37°C. The release of drug molecules from DOX-PAMN (Fig. 5.11) follows a time dependent release profile. While pure DOX shows the rapid release behaviour with $t_{1/2}$ (time needed for the release of 50% of the dose) about 45 min, the DOX-PAMN show sustained release profile with $t_{1/2}$ about 6 h. It has been observed that about 90% of loaded drug molecules were released from the DOX-PAMN system at pH=5. Furthermore, the short time release behaviour of DOX from DOX-PAMN (inset of Fig. 5.11) shows a linear relationship between the drug release and square root of time ($t^{1/2}$) as expected from Higuchi drug release model confirming that the DOX release process is diffusion-controlled [196].
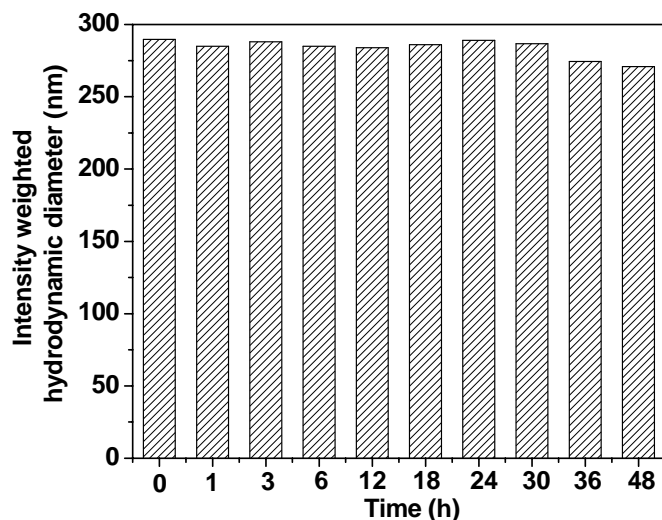
Fig. 5.10. *Variation of intensity weighted (z-average) hydrodynamic diameter of DOX loaded PAMN (DOX-PAMN) as a function of time.*

We have also carried out the drug release studies by keeping same pH for reservoir and sink (pH=5 vs. pH=5 and pH=7.3 vs. pH=7.3, Fig. 5.12) to estimate more precisely the contribution of the pH gradient on the DOX release from the DOX-PAMN system. Our release studies indicate triggered release of electrostatically bound drug molecules at acidic environment (percentage of drug release is much

higher at pH=5 vs. pH=5 and pH=5 vs. pH=7.3 than pH=7.3 vs. pH=7.3). This is desirable for cancer therapy as the relatively low pH in tumours will specifically stimulate the release of drug at the target site.
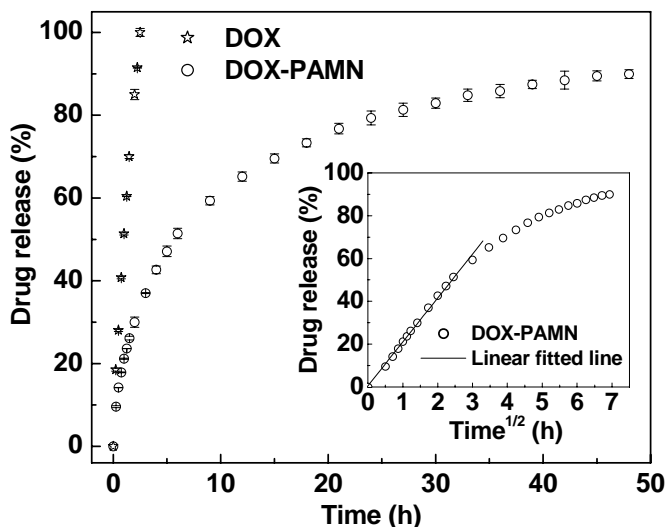
Fig. 5.11. *Drug release profile of pure DOX and DOX-PAMN in cell mimicking environment (reservoir: pH=5 and sink: pH=7.3) at 37°C.*
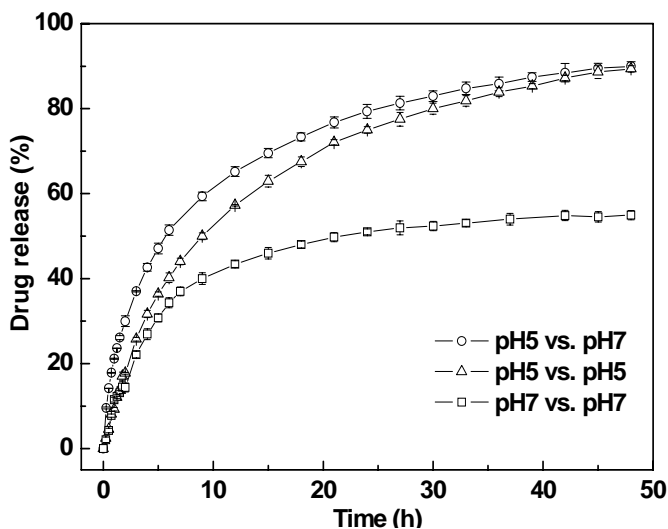
Fig. 5.12. *Drug release profile of DOX-PAMN by keeping same pH for reservoir and sink (pH=5 vs. pH=5 and pH=7.3 vs. pH=7.3). For comparison, drug release profile of pH=5 vs. pH=7.3 is also included in the figure.*

The pH triggered release of DOX could be attributed to the weakening of the electrostatic interactions between the drug and the partially neutralized phosphate groups on the nanocarrier surface. Further, drug release studies were carried out in pH=7.3 and pH=5 under AMF in sink condition. There is no significant release of drug was observed under AMF as compared to their respective control experiments. In present study, it has been observed that local heating is not capable of release electrostatically bound drug from the nanocarriers.

5.3.8. Cell viability of DOX-PAMN

Biomedical application of NPs involves their intentional exposure to the human body. Therefore, understanding the properties of NPs and their effects on the human body is crucial before they are applied clinically. Our MTT assay showed that more than 85% of MG63 cells were viable, even after 24 h incubation with 250 μg/mL of PAMN (Fig.5 13a).
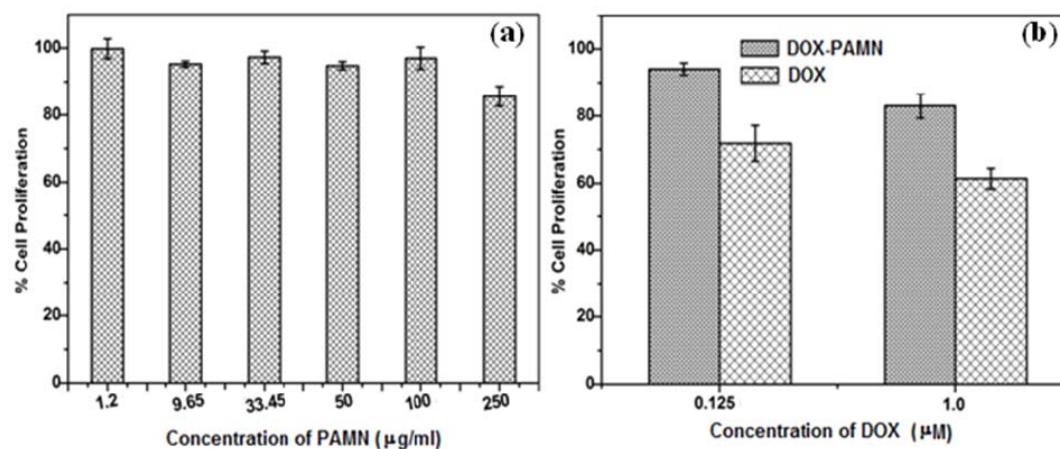
Fig. 5.13. Viabilities of MG63 cells incubated in medium containing different concentrations of (a) PAMN and (b) DOX and DOX-PAMN at 37°C for 24 h.

This result suggests that these phosphate functionalized NPs are biocompatible and do not have toxic effect for further *in-vivo* use. However, DOX and DOX-PAMN show toxicity to the proliferation of MG63 cells (Fig.5 13b). The relatively lower cytotoxicity of DOX-loaded PAMN, compared to DOX, can be attributed to the sustained release behaviour of the nanocarriers (loaded drug is expected to release slowly over the experimental period).

5.3.9. Hemocompatibility and SDS-PAGE analysis

The percentage of hemolysis was found to be around 2.5% upon incubation of 0.5 mg of PAMN, which indicates their good hemocompatibility. However, our SDS-PAGE staining studies (Fig. 5.14) with Coomassie Brilliant blue R250 showed the various protein bands ranging from 205 kDa to 6.5 kDa, in both plasma and cytosolic fluid incubated nanoparticles. This result indicates the interaction of NPs with proteins of plasma and cytosolic fluid. The dynamic layer of proteins, so called protein corona on the PAMN surface determines its ability to interact with the living system and thereby modifies the cellular uptake/response of these nanoparticles. Thus, further studies are required to evaluate the importance of protein-particle interaction in nanotoxicity and prevention of opsonization in biological environment. Specifically, present study demonstrates the preparation of highly crystalline, water dispersible, bioactive phosphate anchored Fe_3O_4 magnetic nanocarriers having excellent self-heating efficacy and their applications in drug delivery and hyperthermia.
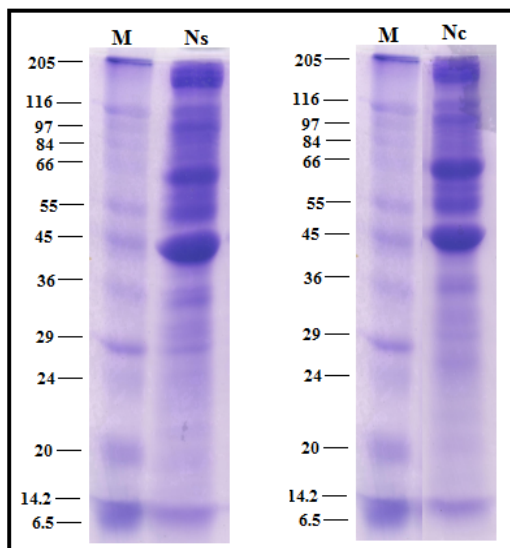
Fig. 5.14. *SDS-PAGE analysis showing interaction of PAMN with proteins from the serum and cytosolic fluid.*

5.4. Summary

A simple facile approach for the synthesis of phosphate anchored Fe_3O_4 aqueous colloidal magnetic nanocarriers of average size about 10 nm is demonstrated. XRD and TEM analysis confirmed the formation of highly crystalline single phase Fe_3O_4 nanostructures. The detailed structural analyses by FTIR, TGA, DLS and zeta-potential confirmed the successful functionalization of Fe_3O_4 NPs with phosphate molecules. These superparamagnetic nanocarriers exhibit better colloidal stability and good biocompatibility with excellent heating efficacy under AC magnetic field. Furthermore, NPs showed high loading affinity for DOX and their sustained release profile under acidic environment. This sustained release of drug is desirable for cancer therapy as the relatively low pH in tumours will specifically stimulate the release of drug at the target site. The high loading affinity for DOX with their sustained release profile and self-heating capacity makes these nanocarriers suitable for drug delivery as

well as hyperthermia treatment of cancer. Specifically, this study demonstrates a tailored approach for generating novel biocompatible magnetic probes for clinical applications.

Chapter 6

Folic acid conjugated magnetic nanoparticles for targeted cancer therapy

6.1. Introduction

MNPs with the application of targeted delivery can be recognized by functionalization or modification of the surface with amino acids, peptides and biomolecules [156, 208, 161, 245, 248-252]. It has been believed that targeted delivery is very important for anticancer drug delivery systems, as most of commonly used anticancer drugs have severe side effects due to non-specific action on the healthy cells. Moreover, targeted delivery would enhance the therapeutic efficacy [56, 253]. Further, by applying an AC magnetic field (AMF) to MNPs, once they are in the vicinity of a tumour, raises the temperature of the medium up to 42-43°C, which is the temperature required for hyperthermia treatment of cancer [254-255].

A conventional approach for conjugating targeting moieties/biomolecules to the surface of MNPs is the formation of amide linkages between amino groups on surface of MNPs and carboxylic groups of targeting moieties/biomolecules or vice versa. The reaction involves the protection and deprotection of unnecessary functional groups to prevent unintended bond formation and therefore is a multistep complex reaction. These problems can be overcome by the click-chemistry. As click-chemistry is a very simple and universal technique for the linkage of reaction partners in high yield, solvent insensitive and at moderate reaction conditions, its use for the modification of the nanoparticle surfaces has become widespread [256]. Among the others, radical addition of thiol to alkene, the thiol-ene reaction, is a click reaction [257] and is widely employed in the field of surface and polymer modification. Although this thiol-ene click reaction is extremely useful but very fewer reports are available in the literature on the modification of the nanoparticle surface with biomolecules via thiol-ene click reaction [105, 258]. Further, MNPs conjugated with receptor and fluorescent

markers can provide detailed understanding of disease-related biological process at molecular level. Moreover, multifunctional MNPs conjugated with receptor molecules can be used for the targeted drug delivery. Folate receptors (FR) are over expressed in human cancer cells but negligibly present in healthy cells [142, 259-261]. Therefore, FR could serve as an excellent tumour marker as well as a functional tumour specific receptor.

Herein, we reported the preparation of amine and carboxyl enriched bifunctional magnetic nanoparticles (BMNPs) via thiol-ene click reaction between undecenoic acid coated Fe_3O_4 nanoparticles (UMNPs) and biologically active cysteine molecules. Further, folic acid was conjugated to these BMNPs for drug delivery and hyperthermia application. These functionalized MNPs showed high colloidal stability, biocompatibility, good magnetic field responsivity and excellent self-heating efficacy. Moreover, high affinity of these folic acid conjugated NPs towards positively charged anticancer drug, DOX, their pH triggered release and substantial cellular internalization makes them suitable for drug delivery. These nanocarriers also show substantial cytotoxicity to cancer cells in association with DOX.

6.2.1. Synthesis of undecenoic acid functionalized Fe_3O_4 magnetic nanoparticles (UMNPs)

UMNPs were prepared by co-precipitation of Fe-chloride precursors in basic medium followed by *in-situ* functionalized with 10-undecenoic acid. In a typical synthesis, 5.406 g of $FeCl_3.6H_2O$ and 1.988 g of $FeCl_2.4H_2O$ in 80 mL water in a round bottom flask and temperature was slowly increased to 70°C under nitrogen atmosphere with constant stirring. The temperature was maintained at 70°C for 30 min and then 30 mL of 25% ammonia solution was added instantaneously to the reaction

mixture, and kept for another 30 min at 70°C. Then, 5 mL of 10-undecenoic acid was added and temperature was slowly raised up to 90°C and reacted for 60 min with continuous stirring for creating double bonds on the surface of Fe$_3$O$_4$ NPs with undecenoic acid molecules. The obtained black coloured hydrophobic NPs were then thoroughly rinsed with ethanol and separated from the supernatant using a permanent magnet (field strength ~ 2.5 kOe).

6.2.2. Synthesis of bifunctional Fe$_3$O$_4$ magnetic nanoparticles (BMNPs)

BMNPs were prepared by introducing cysteine molecules onto the surface of UMNPs by thiol-ene click reaction between thiol group of cysteine and double bond present on the surface of UMNPs. The aqueous solution of cysteine (0.12 g in 10 mL) was added to ethanolic dispersion of UMNPs (0.5 g in 30 mL) and sonicated for 15-20 min to obtain a homogeneous mixture. Then, Azobisisobutyronitrile (AIBN, 5 mg in 10 mL ethanol) was added in the above mixture and further sonicated for 90 min at 60°C to modify the surface of UMNPs with cysteine. The obtained hydrophilic particles were thoroughly rinsed with water and separated from the solution using a permanent magnet, and purified by dialysis against milli Q water.

6.2.3. Synthesis of folic acid conjugated BMNPs (FBMNPs)

FBMNPs were prepared by tagging of folic acid with BMNPs through EDC-NHS coupling reaction. 5 mg folic acid (0.1 mg/mL) was dispersed in water and placed in an ultrasonic bath for 15 min. 0.5 mL of N-Hydroxysuccinimide (NHS, 1 mg/mL) and 0.5 mL of Ethylcarbodiimide hydrochloride (EDC, 1 mg/mL) were added and the mixture was sonicated for 20 min for the activation of carboxylic group of the folic acid. Then, 84 mg of the hydrophilic BMNPs dispersed in 20 mL of water were added to the above mixture and reaction was allowed to take place for 3 h with

continuous mechanical stirring. The obtained particles were separated by a permanent magnet and dried for further characterizations. The schematic representations of the synthesis of BMNPs through thiol-ene click reaction followed by conjugation of folic acid are shown in Fig.6 1.

Cysteine, a water-soluble, sulphur containing amino acid, is used to convert the hydrophobic UMNPs into hydrophilic BMNPs (Fig. 6.1) and then folic acid is conjugated onto the distal end of cysteine to target cancer cells.
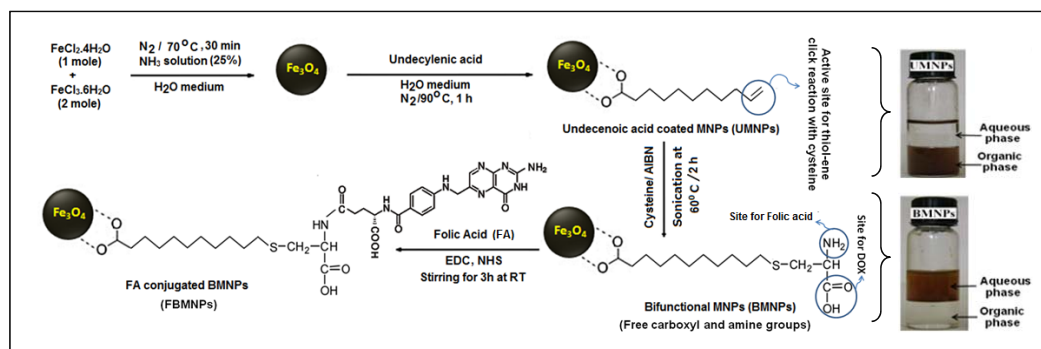
Fig. 6.1. *Schematic representations of the synthesis of UMNPs, BMNPs and FBMNPs along with the photographs of UMNPs and BMNPs solution in different medium.*

6.3.1. Structural studies of UMNPs, BMNPs and FBMNPs

Fig. 6.2 shows (a) XRD patterns of UMNPs, BMNPs and FBMNPs and (b) TEM image of FBMNPs (inset shows its HRTEM image). XRD patterns (Fig. 6.2a) exhibit peaks that are in agreement with known positions of magnetite that suggests the formation of highly crystalline single phase cubic inverse spinel Fe_3O_4 nanostructure. The average crystallite sizes were estimated about 10 nm from X-ray peak broadening. From TEM micrograph, it is also evident that the average size of Fe_3O_4 NPs is ~ 10 nm. The HRTEM image (inset of Fig. 6.2b) of FBMNPs also

confirmed the high crystallinity of their constituents. The average interfringe distance of FBMNPs was measured to be ~ 0.30 nm which corresponds to (220) plane of inverse spinel structured Fe_3O_4.
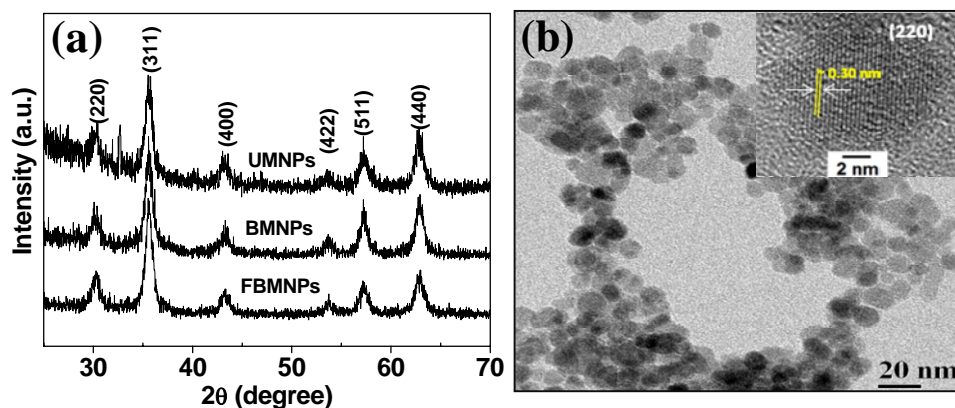
Fig. 6.2. *(a) XRD patterns of UMNPs, BMNPs and FBMNPs, and (b) TEM image of FBMNPs (inset shows its HRTEM image of FBMNPs).*

Fig. 6.3 shows the FTIR spectra of undecenoic acid, cysteine, UMNPs and BMNPs. Undecenoic acid and UMNPs show absorption bands at 1635, 990 and 950-900 cm^{-1} due to the C=C stretching mode, -CH= and =CH_2 out of plane bending vibrations, respectively. The disappearance of characteristic C=O stretching vibrational band at 1760 cm^{-1} (present in case of undecenoic acid) in UMNPs shows the conjugation of undecenoic acid with Fe_3O_4 through chemisorptions of COOH group. Most of the vibrational bands of cysteine are clearly observed in FTIR spectrum of BMNPs with slight shifting in band positions. However, the disappearance of bands attributed to the C=C and S-H in BMNPs clearly suggest that UMNPs underwent thiol-ene reaction with cysteine (thiol-ene click reaction between C=C bond of UMNPs and S-H bond of cysteine). These results demonstrated the

formation of cysteine-conjugated nanoparticles. The strong IR band observed at around 577 cm^{-1} in UMNPs and BMNPs can be ascribed to the Fe-O stretching vibrational mode of Fe$_3$O$_4$. The organic modification of UMNPs to BMNPs is also evident from TGA analysis (Fig. 6.4, the weight losses of about 12 % and 15.5 % for UMNPs and BMNPs, respectively).
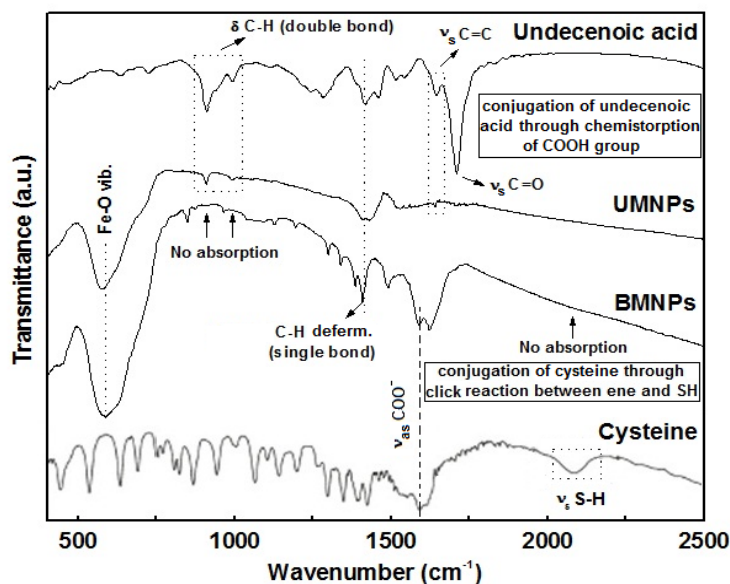
Fig. 6.3. *FTIR spectra of undecenoic acid, cysteine, UMNPs and BMNPs with their peak assignments.*

In order to achieve site-specific targeting, we have introduced folic acid (FA) onto the surface of BMNPs. FA is an essential vitamin for cell survival due to its role in the synthesis of nucleotide bases. It is also a low molecular weight targeting molecule that can be easily coated onto the surface of MNPs by simple bioconjugation chemistry, which may further couple to the folate receptor in the tumour cells. The UV-visible spectrophotometer was employed to confirm the conjugation of FA onto the surface of BMNPs. From Fig. 6.5, it can be observed that the characteristic absorption peak of FA due to $\pi \rightarrow \pi^*$ transition of its pterin ring is appeared at 283

nm [262-263]. However, a bathochromic shift could be noticed in FBMNPs compared to that of pure FA, which indicates the modification in the environment of the FA between the free and grafted states [76]. These results suggest that FA ligands have been successfully grafted onto the surface of BMNPs.
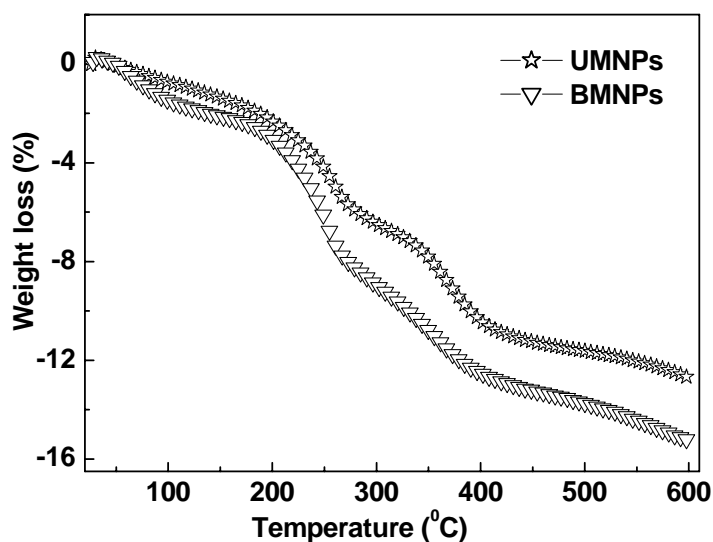
Fig. 6.4. *TGA plots of UMNPs and BMNPs.*
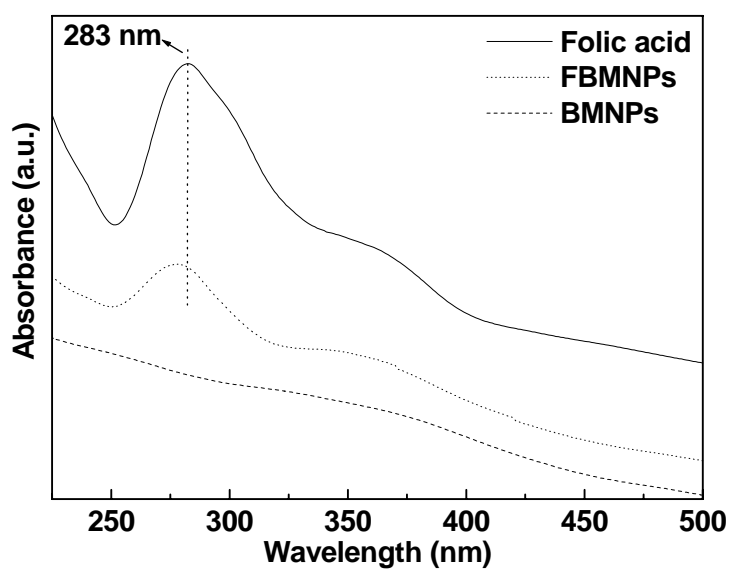
Fig. 6.5. *UV-Visible Spectra of BMNPs, FBMNPs and folic acid.*

Further, FTIR spectroscopic studies also support these results (Fig. 6.6). The characteristic IR absorption peaks at 1605, 1693 and 1485 cm^{-1} are observed in the spectrum of free folic acid due to N-H bending vibration of CONH group, C=O amide stretching of the α- carboxyl group and absorption band of phenyl ring respectively. Folic acid itself contains amide bonds. The increase and broadening of amide bands in the FTIR spectrum of FBMNPs can be attributed to linkage between BMNPs and FA via an amide bond. The bands appeared at around 1550 and 1670 cm^{-1} in FBMNPs (absent in BMNPs) correspond to the vibration of N-H (2° amide) II band and C=O (amide I band). The appearance of these modes suggests the conjugation of folic acid onto the surface of BMNPs.
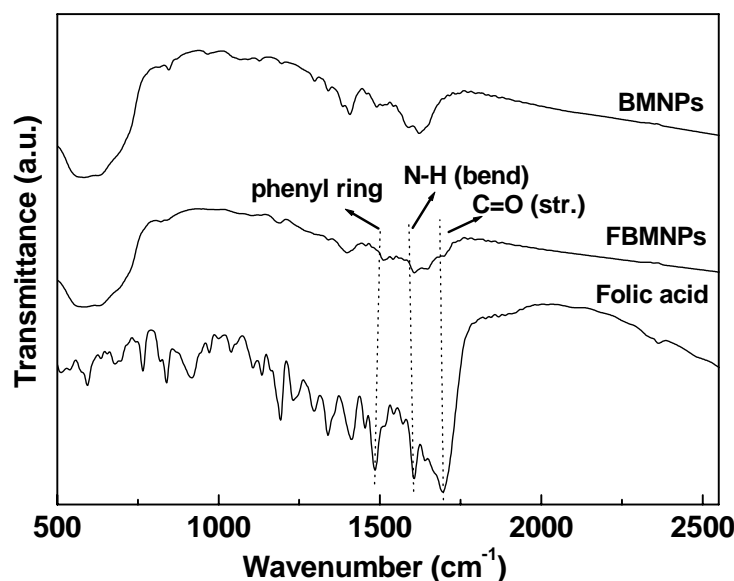
Fig. 6.6. FTIR spectra of folic acid, BMNPs and FBMNPs.

6.3.2. Zeta-potential and colloidal stability of BMNPs and FBMNPs

The colloidal stability of BMNPs and folic acid conjugated BMNPs (FBMNPs) were investigated from light scattering and UV-visible absorption studies. Fig. 6.7 shows the pH dependent zeta-potential of aqueous suspension of BMNPs and

FBMNPs. From zeta-potential measurements, the isoelectric point (pH_{pzc}) of BMNPs and FBMNPs were found to be around 4.3 and 5.3, respectively. The increase in surface charge and shifting of isoelectric point to higher pH further confirms the successful conjugation of folic acid with BMNPs. Thus, these NPs have net positive surface charge at $pH<pH_{pzc}$ and negative surface charge at $pH>pH_{pzc}$. Further, the insignificant change in absorbance of BMNPs and FBMNPs suspensions in aqueous and cell culture media (DMEM+10% FBS) indicates their good colloidal stability (Fig. 6.8).
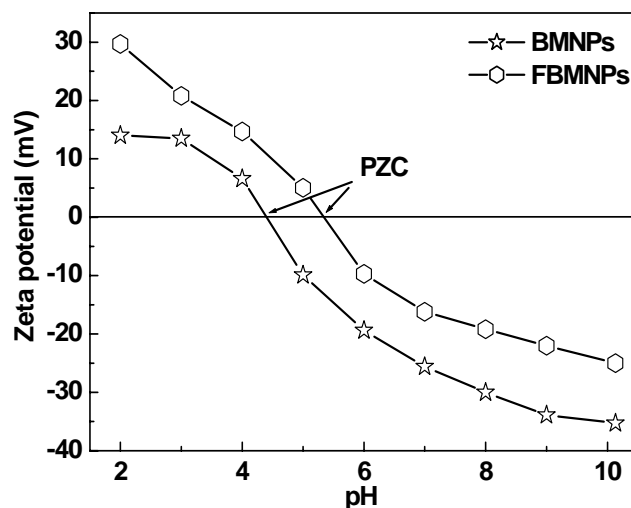
Fig. 6.7. *Variation of zeta-potential of BMNPs and FBMNPs as a function of pH.*

DLS measurement also reveals that BMNPs and FBMNPs render aqueous dispersion with mean hydrodynamic diameter of 40 and 70 nm (Fig. 6.9). The larger hydrodynamic diameter observed by DLS, as compared to TEM arises from the presence of hydrated organic layer and polydispersity in distribution of particles [242]. Specifically, the functionalized exterior provides colloidal stabilization to particles via hydrogen bonding with water. Additionally, the electrostatic repulsive force originating from the ionization of the surface groups also provide stability to these

particles. It is worth mentioning that the negative surface charge of FBMNPs at physiological medium could decrease the possibility of its further interaction with haemoglobin, which would play an important role in improving the stability and blood compatibility.
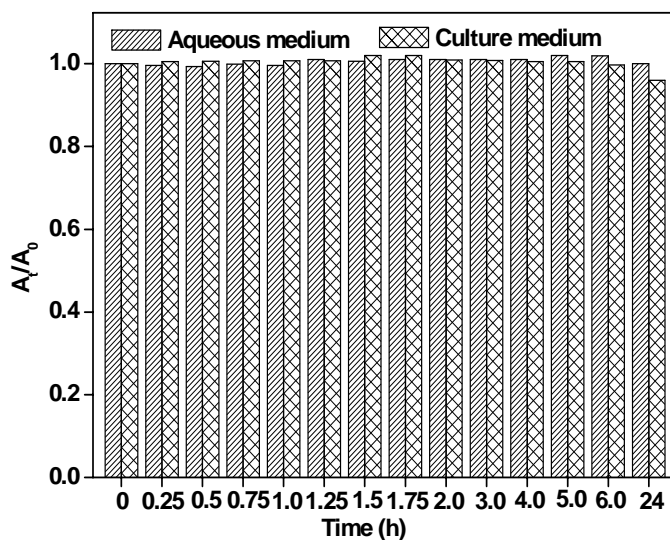
Fig. 6.8. *Normalized UV absorbance (A_t/A_0) vs. time plots of FBMNPs in aqueous and culture medium at a wavelength of 350 nm in different mediums (A_t = absorbance at time 't' and A_0 = absorbance at t=0).*
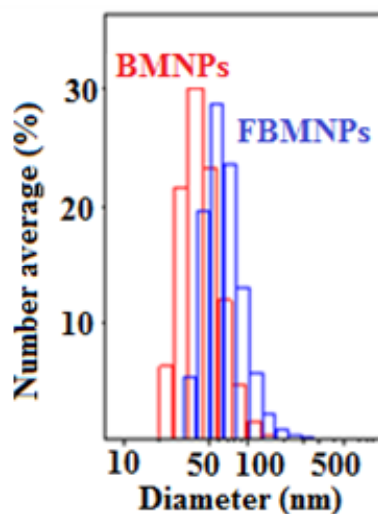
Fig. 6.9. *Number weighted hydrodynamic diameter of BMNPs and FBMNPs.*

6.3.3. Field dependent magnetic measurements of FBMNPs

Fig. 6.10 shows the field dependent magnetization plots of FBMNPs at 5 K and 280 K. FBMNPs exhibit superparamagnetic behaviour without magnetic coercivity and remanence at 280 K and they transform into ferrimagnetic material at low temperature (5 K). This transformation is usually observed below blocking temperature (TB) in MNPs [217]. The ZFC-FC plot (inset of Fig. 6.10) shows that the TB of FBMNPs is 105 K at an applied field of 400 Oe.
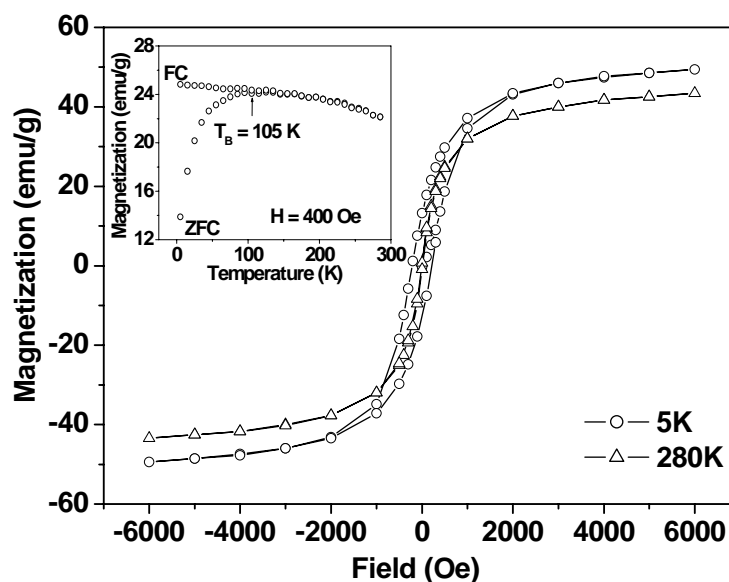
Fig. 6.10. *Field M vs. H plots of FBMNPs at 5 and 280 K and (inset shows their ZFC-FC plot at an applied field of 400 Oe.*

Further, the saturation magnetizations were found to be 49.4 and 43.5 emu/g at 5 K and 280 K respectively. The lower value of magnetization of FBMNPs as compared to the bulk Fe_3O_4 (92 emu/g) can be ascribed to the combined effect of nano-sized Fe_3O_4 particles and presence of robust coating of non-magnetic organic moiety on the particle surface [195]. However, the room temperature

superparamagnetic characteristic with substantial magnetic moment make these FBMNPs efficient candidate for drug delivery and hyperthermia therapy.

6.3.4. Time-dependent calorimetric measurements of aqueous suspension of FBMNPs

Fig. 6.11 shows the temperature vs. time plots of FBMNPs at different AC magnetic field. The plot showed a time-dependent gradual increase in temperature of FBMNPs suspension at a fixed frequency of 265 kHz. The SAR values were found to be 37, 52 and 80 W/g of Fe at magnetic fields of 0.251, 0.335 and 0.419 kOe, respectively. The rise in temperature for our superparamagnetic FBMNPs is mainly associated with the combined effect of Néel and Brownian relaxation losses [185, 192].
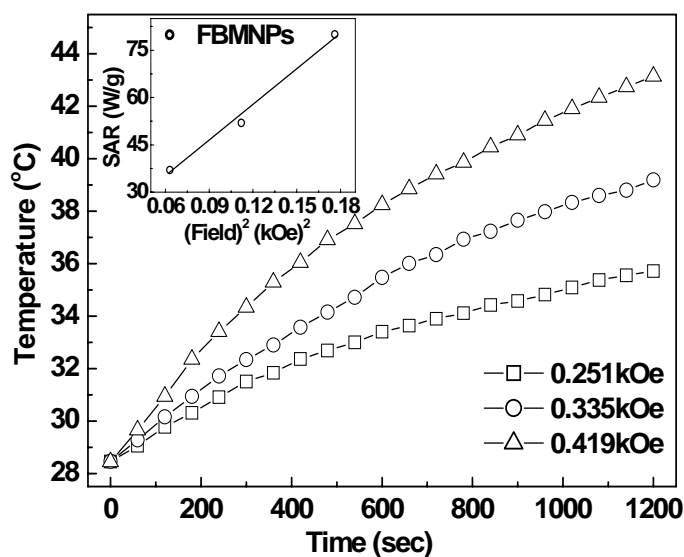
Fig. 6.11. *Temperature vs. time plots of 1 mg/mL aqueous suspension of FBMNPs at different field strength (inset shows the linear relationship between SAR and square of applied field strength).*

Further, SAR values slightly decrease with increase in Fe concentration in the suspension. The SAR values were found to be 55.6, 52 and 42.3 W/g of Fe at 0.75, 1.0

and 1.5 mg/mL of Fe, respectively (field of 0.335 kOe). This may be due to the decrease in Brownian contribution to heating and increase in magnetic dipole-dipole interactions between NPs in suspension as a result of the increase in local concentration of particles [182].

6.3.5. Drug loading and drug release profile of DOX-FBMNPs

In order to explore the use of FBMNPs as drug carrier, we have investigated drug loading and release behaviour using DOX as a model drug. The interaction of DOX with FBMNPs was apparent from the decrease in fluorescence intensity of the supernatant liquid after removal of DOX loaded FBMNPs through magnetic separation (Fig. 6.12).
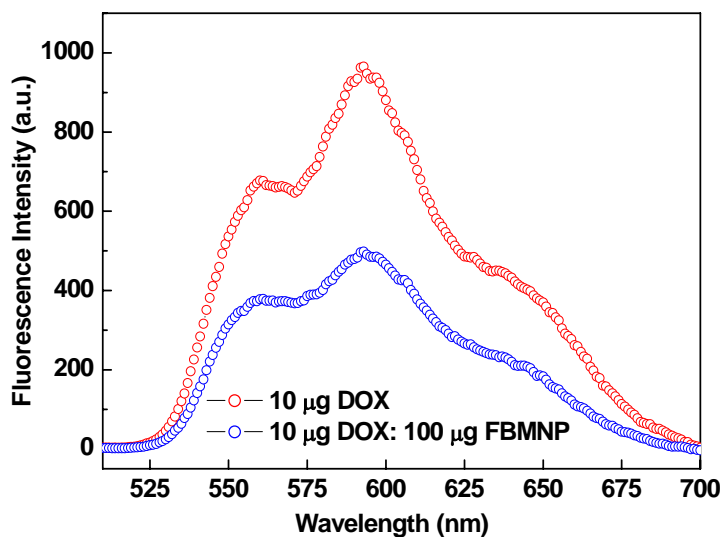
Fig. 6.12. *Normalized fluorescence spectra of 1 mL of pure DOX (10 μg) and after its reaction with 100 μg of FBMNPs (fluorescence was taken after magnetic separation of DOX-FBMNPs).*

About 50% drug encapsulation efficiency (w/w) was obtained with DOX to particles ratio of 1:10. The observed low value of encapsulation efficiency is possibly due to the presence of bulky FA molecules on the surface, which sterically hinder the conjugation of DOX onto the surface of particles.

The drug release profiles of DOX loaded FBMNPs were investigated under reservoir-sink condition (reservoir: pH=4 or 5, sink: pH=7.3) at a temperature of 37°C. The release of drug molecules from DOX-FBMNPs (Fig. 6.13) follows a time dependent release profile. It has been noticed that there is an initial burst release of DOX from FBMNPs and then DOX is released gradually over a period of time. Further, about 93.5% of DOX was released from the DOX-FBMNPs system at pH=4, while 83% of DOX was released at pH=5 after 48 h. However, less than 20 % of DOX release was observed at physiological medium (pH=7.3).
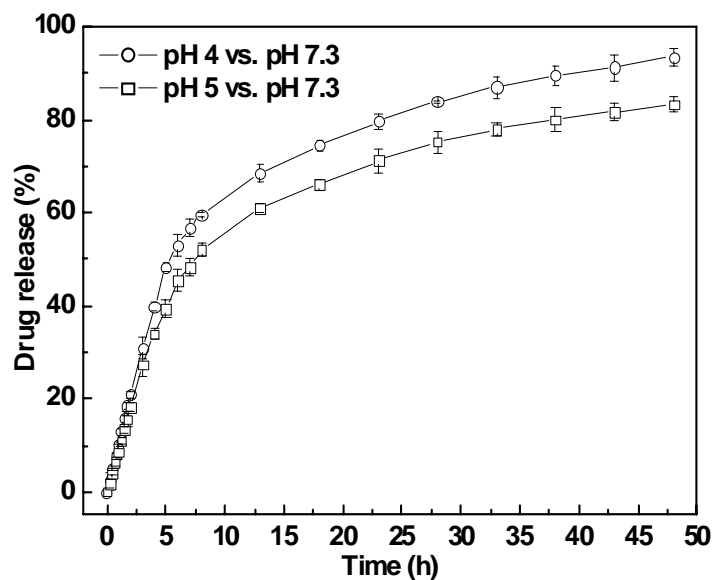
Fig. 6.13. *pH dependent drug release profile of DOX-FBMNPs in cellular mimicking environment (reservoir: pH=4 or 5 and sink: pH=7.3) at 37°C.*

This phenomenon strongly demonstrated the pH sensitive nature of DOX-FBMNPs system. This is desirable for cancer therapy as the relatively low pH in tumours will trigger the release of DOX at the target site. We have attributed this pH triggered release of drug to the weakening of the electrostatic interactions between the positively charged DOX and negatively charged FBMNPs [156, 184]. The electrostatic interaction among them is also confirmed from decrease in absolute value of zeta-potential of FBMNPs upon conjugation with DOX.

6.3.6. Cell viabilities of DOX and DOX-FBMNPs

Fig. 6.14 shows viabilities of WEHI-164 cells incubated in medium containing (a) FBMNPs and (b) DOX-FBMNPs for 48 h. Our MTT assay showed that about 80% of WEHI-164 cells are viable even after incubation with 1 mg/mL of FBMNPs for 48 h. This result suggests that FBMNPs are biocompatible. However, DOX-FBMNPs show substantial toxicity to WEHI-164 cells indicating their good therapeutic efficacy.
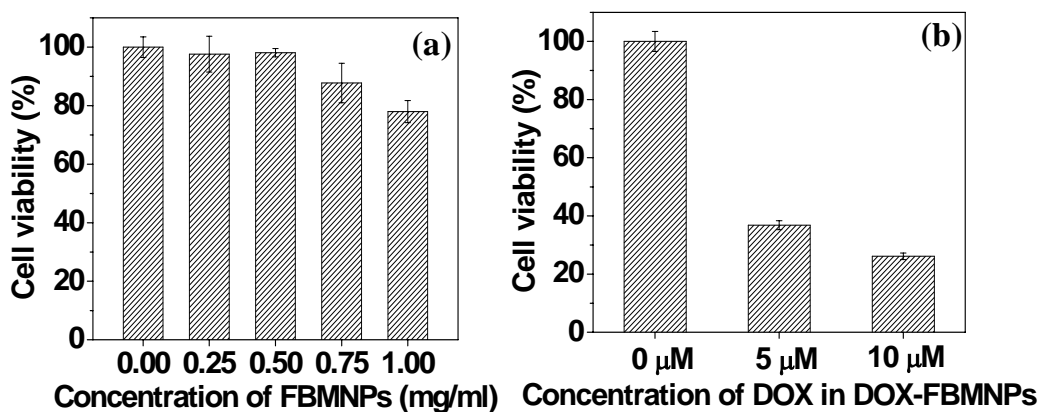
Fig. 6.14. *Viabilities of WEHI-164 cells incubated in medium containing (a) FBMNPs and (b) DOX-FBMNPs for 48 h.*

6.3.7. Hemocompatibility and protein resistance behaviour of FBMNPs

For biological applications, we have explored hemocompatibility, and protein resistance behaviour of FBMNPs. The percentage of hemolysis was found to be 3% upon incubation of 0.5 mg of FBMNPs. This low value of hemolysis (<5%) indicates their good hemocompatibility. In addition, FBMNPs do not show significant change in zeta-potential (Table 6.1) even after incubation with BSA for 2 h, revealing their protein resistance nature in physiological medium.

Table 6.1. Zeta-potential (in mV) of FBMNPs incubated with BSA.

Time (h)	0.02 mg/mL FBMNPs in 0.025 mg/mL BSA in 0.01 M PBS
0	-34.7
0.5	-34.4
1.0	-34.2
2.0	-32.4

6.3.8. Intracellular activity of DOX-FBMNPs with WEHI-164 cells

Since DOX is a fluorophore, its fluorescence emission could be used to evaluate the intracellular activity of DOX loaded FBMNPs with cell lines. Fig. 6.15 shows the CLSM images of WEHI-164 cells after incubation with DOX-FBMNPs and DAPI at culture conditions. A significant uptake of DOX–FBMNPs was clearly observed from the red fluorescence image arising from DOX emissions, suggesting that the drug-loaded particles were internalized in the cells. The blue fluorescence image shows emission from nuclei stained with DAPI. The merged and bright field imaged of DOX and DAPI emission clearly indicates that DOX-FBMNPs are primarily localized in the

cytoplasm. Our observations of MTT assay and CLSM studies demonstrate that the use of these folic acid conjugated magnetic nanocarrier as a drug delivery vehicles could significantly enhance the accumulation of DOX in target cancer cells. Further, these they may have higher internalizing ability in folate receptors over expressed cancer cells.
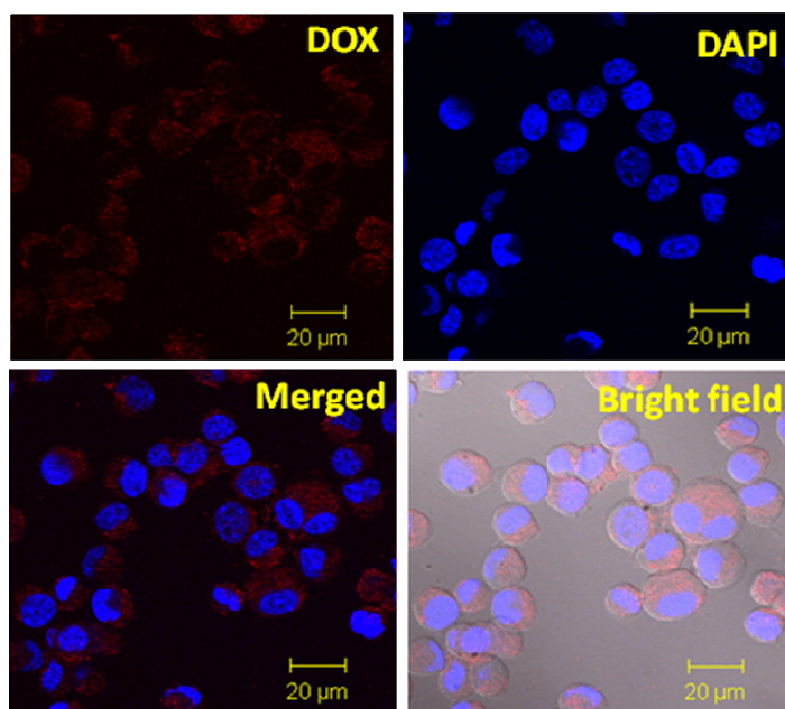
Fig. 6.15. CLSM images of WEHI-164 cells after incubation with the DOX-FBMNPs and DAPI at culture conditions.

6.4. Summary

Bifunctional magnetic nanoparticles (BMNPs) were prepared by coating of cysteine molecules onto the surface of undecenoic acid coated Fe_3O_4 MNPs via thiol-ene click reaction. Structural analysis by XRD and TEM reveal the formation of highly crystalline single-phase Fe_3O_4 nanostructures. These nanocarriers are of

average size 10 nm and resistant to protein adsorption under physiological medium. To achieve site specific targeting to cancer cells, the BMNPs were conjugated with folic acid via amide linkage. FTIR, TGA, light scattering and UV-visible spectroscopic studies confirmed the successful organic modification of nanoparticles. Our induction heating experiments suggest that these folic acid conjugated particles have excellent heating ability under external AC magnetic field. Further, these nanocarrier show high loading affinity for DOX, their pH dependent release and substantial cellular internalization. In association with DOX, they also possess good therapeutic efficacy. Specifically, the surface modification of Fe_3O_4 MNPs with both cysteine and folic acid could be used to resist the protein adsorption and simultaneously facilitate their uptake to specific cancer cells.

Chapter 7

Luminescent marker loaded magnetic nanoparticles for drug tracking

7.1. Introduction

Multifunctional MNPs afford the opportunity not only for diagnostic studies but also for targeted drug delivery. Combining molecular imaging with targeted drug delivery permits verification and quantification of treatment and can serve as a platform technology for many diseases [56, 192, 218, 246, 264-265]. Polymers and surfactants containing functional groups such as carboxylic acids, phosphates and sulfates can effectively bind to the surface of magnetite [55]. It is envisaged that amino acids can be attractive candidates for passivation of metal oxide NPs due to the strong binding affinity of their carboxylate groups towards metal oxides. Furthermore, the presence of high densities of biocompatible amino acid layer with free functional groups ($-NH_2$) on the surface not only stabilizes the Fe_3O_4 nanoparticles, but also provides accessible surface for routine conjugation of biomolecules/luminescent markers (FITC, lanthanides) and targeting receptors (FA, peptides) etc. MNPs coated with specific fluorescent markers or targeting ligands can provide detailed understanding of disease-related biological processes at the molecular level. Amongst the others, folate receptor and FITC marker have relatively simple and well-defined conjugation chemistry. Luminescent markers are used to track the MNPs location in the body from the fluorescence images.

Therefore, we explored the use of short chain amino acid, glycine to functionalize the surface of Fe_3O_4 nanoparticles, which provide the sites for conjugation of biomolecules as well as luminescent markers. Specifically, a facile method for the preparation of folate-conjugated luminescent iron oxide nanoparticles (FLIONs) is developed and their potential application in magnetic hyperthermia. The

excellent aqueous colloidal stability, low toxicity and good self-heating capacity make these novel NPs suitable for hyperthermia treatment of cancer.

7.2.1. Synthesis of amine functionalized iron oxide nanoparticles (AIONs)

Amine functionalized iron oxide nanoparticles (AIONs) were prepared through co-precipitation of Fe^{2+} and Fe^{3+} followed by *in-situ* grafting of glycine molecules [185] (Fig. 7.1). For the synthesis of AIONs, 5.406 g of $FeCl_3.6H_2O$ and 1.988 g of $FeCl_2.4H_2O$ were dissolved in 80 mL of water in a round bottom flask and temperature was slowly increased to 70^oC under nitrogen atmosphere with constant mechanical stirring at 1000 rpm. The temperature was maintained at 80^oC for 30 min and then 30 mL of 25% ammonia solution was added instantaneously to the reaction mixture, and kept for another 30 min at 80^oC. Then, 4 mL aqueous solution (0.3 gm/mL) of glycine was added and temperature was slowly raised up to 90^oC and reacted for 60 min with continuous stirring. The obtained black coloured precipitates were then thoroughly rinsed with water and separated from the supernatant using a permanent magnet (field strength ~ 2.5 kOe).
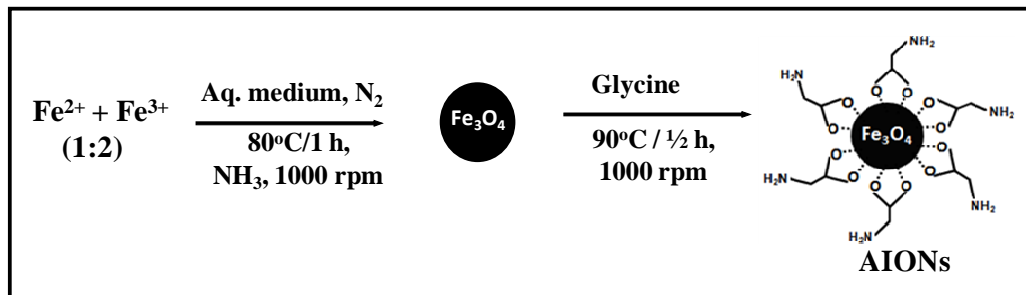
Fig. 7.1. *Schematic representation of the synthesis of amine functionalized iron oxide nanoparticles (AIONs) by co-precipitation method.*

7.2.2. Synthesis of folate-conjugated iron oxide nanoparticles (FIONs) and folate-conjugated luminescent iron oxide nanoparticles (FLIONs)

In order to conjugate the folate receptor, 80 mL aqueous solution of folic acid (FA, 5 mg) was activated by 1 mL of 1-ethyl-3-(3-dimethylaminopropyl)carbodiimide (EDC, 1 mg/mL) and 1 mL of N-hydroxysuccinimide (NHS, 1 mg/mL) under sonication for 30 min. Then, 20 mL aqueous dispersion of AIONs (80 mg) were added to the activated FA solution and reacted for 2 h under stirring at room temperature (RT). Then, folate-conjugated iron oxide nanoparticles (FIONs) were magnetically separated and thoroughly washed with milli Q water. These FIONs (20 mg) were redispersed in water (8 mL) and then 2 mL aqueous solution of FITC (0.5 mg) was added. This reaction mixture was kept under shaking for 1 h at RT and then separated, and thoroughly washed to obtain folate-conjugated luminescent iron oxide nanoparticles (FLIONs) (Fig. 7.2).
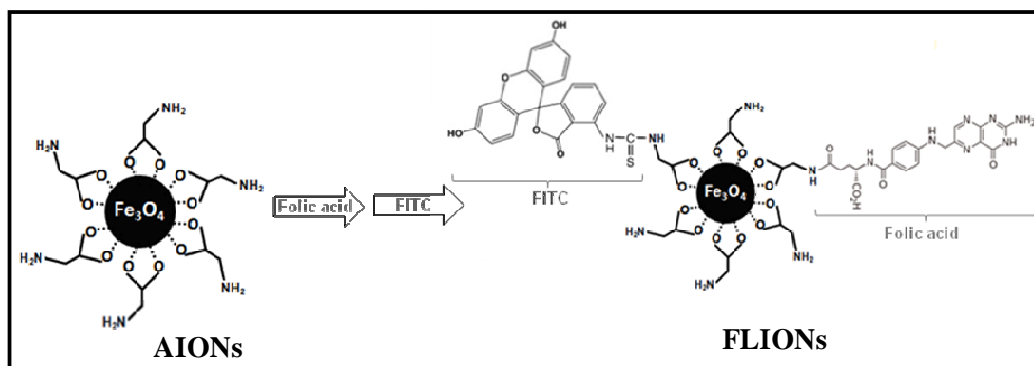
Fig. 7.2. *Schematic representation of the synthesis of folate conjugated luminescent iron oxide nanoparticles (FLIONs).*

7.3.1. Structural studies of AIONs

Fig. 7.3 shows (a) XRD pattern, (b) TEM and (c) high resolution TEM micrographs of AIONs. XRD analysis revealed the formation of highly crystalline

single phase cubic inverse spinel Fe_3O_4 structure with lattice constant, a ~8.378 Å, which is very close to the reported value of magnetite (JCPDS Card No. 88-0315, a = 8.375 Å). The presence of six characteristic sharp and intense peaks confirmed the formation of highly crystalline nanoparticles. The average crystallite size of AIONs is found to be ~10 nm (r < 10%) from X-ray line broadening using the Scherrer formula.
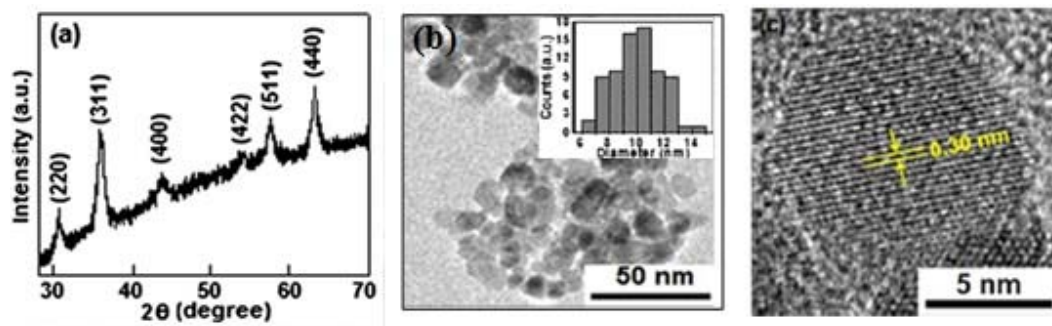
Fig. 7.3. *(a) XRD pattern, (b) TEM and (c) high resolution TEM micrographs of AIONs. Inset of fig. 7.3b shows their particles size distribution.*

From TEM micrograph, it is also evident that the average size of Fe_3O_4 NPs is ~10 nm (the particle size distribution plot is shown in inset of Fig. 7.3b). HRTEM image (Fig. 7.3c) of AIONs also confirmed the high crystallinity of their constituents. From HRTEM, the average interfringe distance of AIONs was measured to be ~0.30 nm which corresponds to (220) plane of inverse spinel structured Fe_3O_4.

Fig. 7.4 (a) shows the FTIR spectra of glycine and AIONs with their corresponding peak assignments in the wave number ranging from 500–3500 cm^{-1}. The absorption bands for the pure glycine (zwitter ionic forms) are well resolved, but those of the AIONs are rather broad and a few. The IR bands observed at around 588 cm^{-1} in AIONs can be ascribed to the Fe–O vibrational mode of Fe_3O_4. Most of the vibrational modes correspond to pure glycine (COO^-, NH_3^+, CH_2, CO and CN) are

also observed in the FTIR spectrum of AIONs [185]. Interestingly, the symmetric (υ_s) and asymmetric (υ_{as}) stretching bands of COO group of glycine are shifted from 1414 to 1400 cm^{-1} and 1600 to 1586 cm^{-1} upon functionalizing the Fe_3O_4 NPs with glycine moiety. Furthermore, the wave number separation ($\Delta = 186$ cm^{-1}) between υ_s COO$^-$ and υ_{as} COO$^-$ indicates the bridging bidentate type of covalent bonding [266]. This suggests that glycine is chemisorbed onto the surface of Fe_3O_4 NPs through the carboxylate group, leaving freely exposed amine (–NH$_2$) groups. Earlier investigation on interaction of Fe_3O_4 NPs with 3-chloropropionic acid and amino acids also suggested that carboxylate head is the preferable site for chemical conjugation with Fe_3O_4 [267-268].
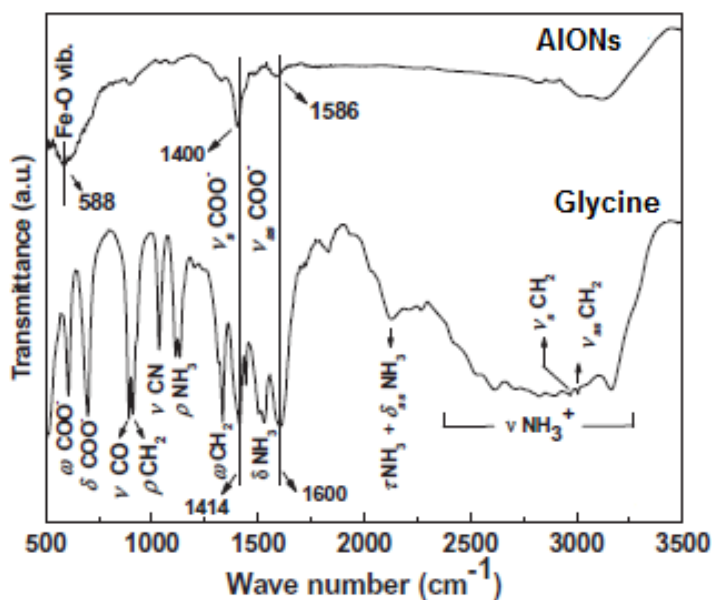
Fig. 7.4. *FTIR spectra of glycine and AIONs with their corresponding peak assignments in the wave number ranging from 500-3500 cm^{-1}.*

The thermogravimetric analysis also supports the presence of organic components on the surface of Fe_3O_4 NPs (a weight loss of about 4.8% is observed up

to 600°C). Thus, FTIR and TGA analyses confirmed the successful functionalization of Fe_3O_4 NPs with glycine during the course of synthesis.

7.3.2. Light scattering measurements

Light scattering measurements such as zeta-potential and DLS are additional characterization methods that are in favour of the complete functionalization of the MNPs by organic molecules. Fig. 7.5 shows the zeta-potential (ζ) measurements of AIONs at different pH. From zeta-potential measurements, pH_{pzc} of AIONs was found to be around 5.3. Thus, the AIONs have net positive surface charge at $pH < pH_{pzc}$ and negative surface charge at $pH > pH_{pzc}$. This difference in their charge properties may be attributed to the degree of ionization of functional groups at different pH. It has been observed that the pH_{pzc} of Fe_3O_4 decreases upon binding of glycine onto the surface of Fe_3O_4 NPs (pH_{pzc} of bare Fe_3O_4 NPs is 6.7 [269]).
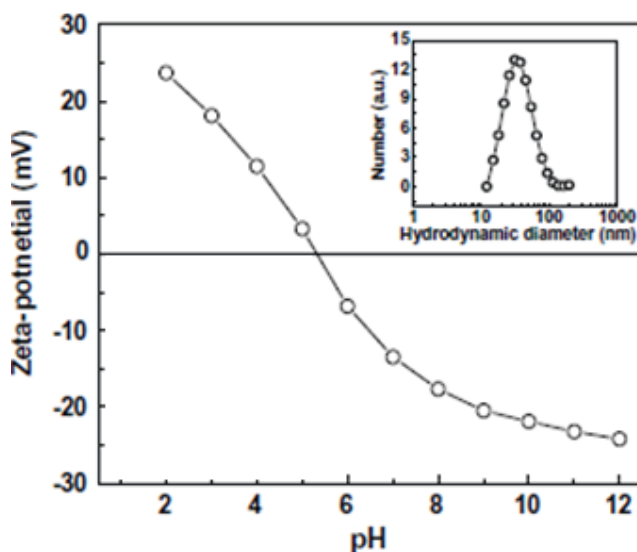
Fig. 7.5. *Zeta-potential (ζ) measurements of AIONs at different pH. Inset shows the DLS plot indicating the number average hydrodynamic diameter of AIONs.*

DLS measurement of AIONs (inset of Fig. 7.5) indicates that these samples render aqueous colloidal suspension with mean hydrodynamic diameter of about 30 nm (σ<10%) due to the presence of associated and hydrated organic layers [270]. The observed higher hydrodynamic diameter could also arise from the polydispersity of the particles. As DLS is weighted towards large sizes, the average diameter could be higher than those obtained from TEM. However, the average hydrodynamic diameter and polydispersity index hardly varies with time revealing their excellent aqueous colloidal stability. The colloidal stability of the particles were assessed from the changes in absorbance of AIONs suspensions as a function of time (Fig. 7.6). The insignificant change in absorbance of AIONs suspension (0.1 mg/mL) in water and cell culture medium (DMEM + 10% FBS) with time (even after 48 h) indicates their good colloidal stability. Further, the absorbance of AIONs suspension hardly varies with (0.1, 0.15, 0.2 and 0.3 M) NaCl concentration.

Specifically, the carboxylate groups of glycine strongly coordinate to iron cations on the Fe_3O_4 surface to form a robust coating [267-268], while the functionalized exteriors ($-NH_2$ groups) of AIONs extend into the water medium, conferring a high degree of water stability to Fe_3O_4 NPs by forming hydrogen bonds between NH_2 groups and water [271]. In addition to this, the electrostatic repulsive force originating from the ionization of the surface groups also provide stability to the particles. The highly negative value of zeta-potential of these functionalized AIONs in 0.01 M PBS, pH=7.3 (ζ = -20 mV) indicate their good stability in physiological medium. The absolute zeta-potential value of more than 25 mV is ideal for good kinetic stability at RT, when the particles are stabilized through purely electrostatic repulsion. However, in the presence of other forces such as steric and hydrogen

bonding interactions, the stability can be achieved even at low surface potentials. Our zeta-potential values are consistent with those reported earlier [272-273].
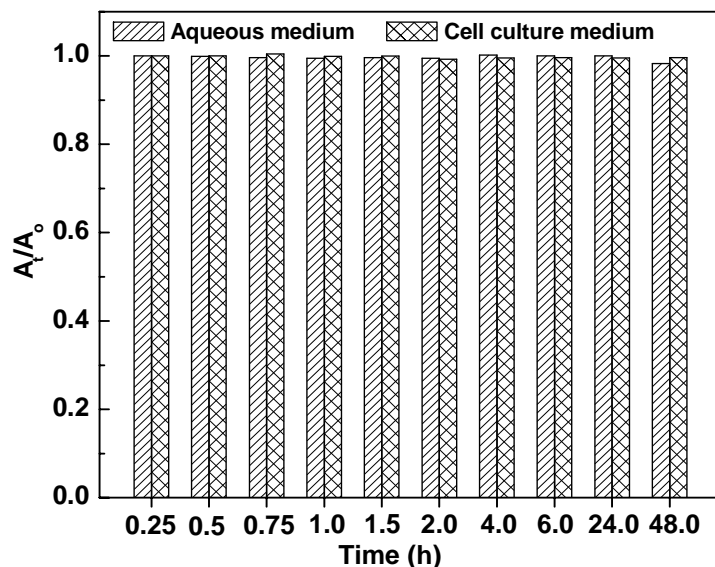
Fig. 7.6. *Normalized UV absorbance (A_t/A_0) vs. time plot of PSMN (0.1 mg/mL) at wavelength of 350 nm in aqueous and cell culture medium (A_t = absorbance at time 't' and A_0 = Absorbance at t = 0).*

7.3.3. Field dependent magnetic measurements of AIONs

Fig. 7.7 shows the field dependent magnetization plots of AIONs at 5 K and 300 K. The AIONs exhibit superparamagnetic behaviour without magnetic coercivity and remanence at 300 K, whereas ferromagnetic behaviour with a coercivity of about 230 Oe is observed at 5 K (inset of Fig. 7.7). This transition from superparamagnetic behaviour at room temperature to ferro or ferrimagnetic behaviour below the so-called blocking temperature is typically observed in MNPs [85]. The saturation magnetizations of AIONs (at an applied field of 20 kOe) were found to be 65.2 and 70.8 emu/g at 300 and 5 K, respectively. It has been observed that the room temperature magnetization of AIONs was reduced to about 70% of the bulk Fe_3O_4 (92

emu/g). The decrease in magnetization can be attributed to the combined effect of nano size of core Fe_3O_4 particles (large surface to volume ratio) and robust coating of glycine molecules on their surface (quenching of magnetic moment by electron exchange between coating and surface atoms) [221]. However, the retention of superparamagnetic property at room temperature with such a reasonably high (optimal) magnetic moment and biocompatible amino acid shell makes these NPs suitable for various biomedical applications such as magnetic hyperthermia, site-specific magnetic drug targeting and MRI etc.
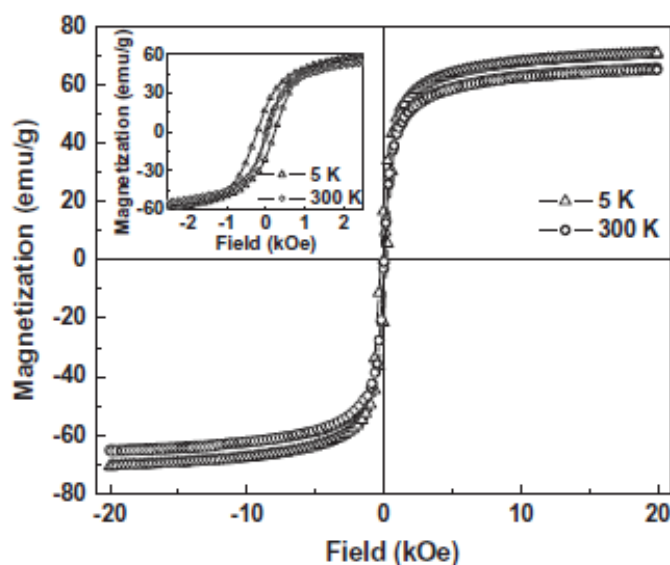
Fig. 7.7. *Field dependent magnetization plots of AIONs at 5K and 300 K (inset shows its expanded M vs. H plot at the low- field region showing coercivity).*

The detailed structural analyses of AIONs by XRD, FTIR, TGA, light scattering techniques and magnetization measurements confirmed the successful passivation/ functionalization of Fe_3O_4 NPs with glycine molecules. The amine groups present on Fe_3O_4 NPs in AIONs can provide accessible surface for conjugation of many biomolecules for drug delivery, drug targeting and drug tracking etc.

In order to achieve the targeted drug delivery, folate-conjugated iron oxide NPs (FIONs) has been synthesized. For this, we conjugated the folate receptor with AIONs via EDC-NHS coupling. Then, the obtained magnetic FIONs were thoroughly washed with water. The above formed FIONs were further conjugated with FITC to obtain folate-conjugated luminescent iron oxide nanoparticles (FLIONs) to achieve drug tracking in the body. The structural, interfacial and magnetic properties of FLIONs were investigated.

7.3.4. Structural studies of FIONs and FLIONs

The surface chemical structure of FLIONs was studied by FTIR and UV-Vis absorption spectroscopy. Fig. 7.8 shows the FTIR spectra of AIONs, FA, FIONs, FITC and FLIONs in the range of 500-2500 cm^{-1} with their peak assignments. The band observed at 588 cm^{-1} can be ascribed to the Fe-O vibrational mode of Fe_3O_4. The bands appeared at 1530 and 1635 cm^{-1} in FIONs (absent in AIONs) correspond to the vibration of N-H (2°-amide) II band and C=O (amide I band). Appearance of these modes suggests the formation of amide linkages due to the conjugation of folic acid (FA). Further, the disappearance of characteristic band of isothiocyanate (–N=C=S) at 2040 cm^{-1} in FLIONs indicates the tagging of FITC by conjugation of amine groups of AIONs with –N=C=S of FITC [20]. The presence of these characteristic vibrational bands in FIONs and FLIONs confirmed the successful conjugation of FA and FITC on the surface of AIONs.

The UV-Vis absorption peaks of FA and FITC are also observed in the spectrum of FLIONs (Fig. 7.9) at slight shifting in their peak positions, which further confirmed the successful grafting of FA and FITC [274-275]. The presence of absorption peaks at 270 and 375 nm in FIONs (absent in AIONs) confirmed the successful conjugation

of folic acid on the surface of AIONs. Further, the grafting of FITC on FIONs was confirmed from absorption peak at 485 nm which is due to the presence of conjugated FITC on the surface of FIONs (Fig. 7.9).
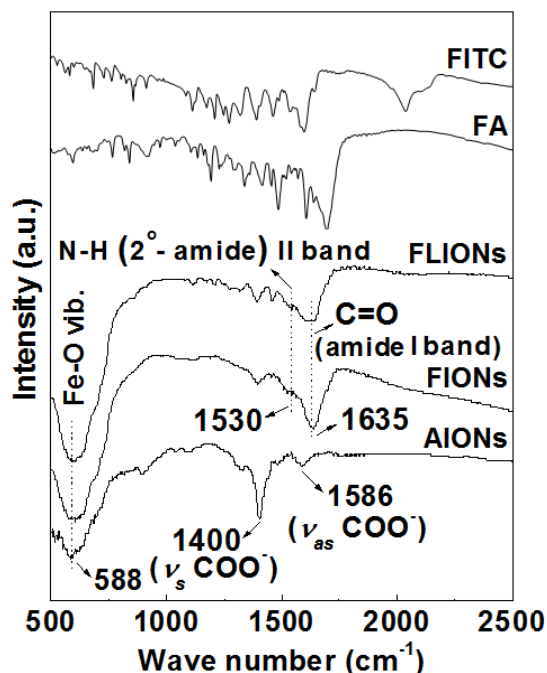
Fig. 7.8. *FTIR Spectra of AIONs, FA, FIONs, FITC and FLIONs in the range of 500-2500 cm^{-1} with their peak assignments.*

Dynamic light scattering (DLS) measurements indicate that the size distribution of FLIONs is monomodal with mean hydrodynamic diameter (D_h) of ~60 nm ($\sigma <$ 10%) due to the presence of associated and hydrated organic layers [270]. In the present case, we believe that the organic shell (including free amine groups on surface) can provide colloidal stabilization to FLIONs via hydrogen bonding. In addition to this, the electrostatic force originating from ionization of the surface groups also provide stability to FLIONs (zeta-potential of -20 mV in water).
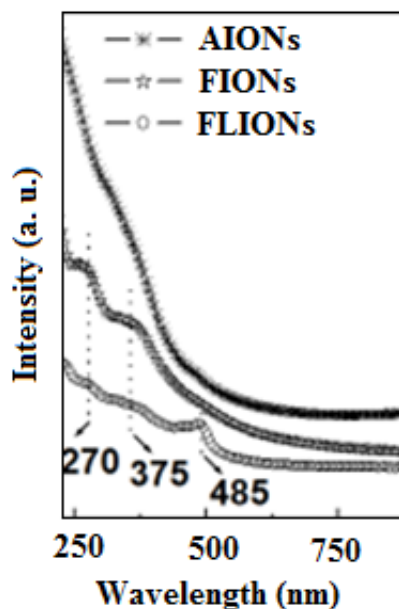
Fig. 7.9. *UV-Vis Spectra of AIONs, FIONs and FLIONs.*

7.3.5. Time-dependent calorimetric measurements of FLIONs

FLIONs exhibit RT superparamagnetic behaviour with a saturation magnetization of 50 emu/g of sample at an applied field of 20 kOe (Fig. 7.10a). The retention of strong magnetic field responsivity indicates that FLIONs could reach the targeted locations under an external magnetic field. The calorimetric measurements of FLIONs showed a time-dependent gradual increase in temperature (Fig. 7.10b). The SAR values of FLIONs were found to be 64.8, 77.9 and 104.0 W/g of Fe at AMF of 335, 376 and 419 Oe, respectively. The observed high SAR values of FLIONs is possibly due to their good colloidal stability and magnetic field responsivity (as heating of superparamagnetic nanoparticles under AMF is due to Néel and Brownian relaxation loss processes) [185]. Further, the time required to reach 42-43°C (hyperthermia temperature) decreases with an increase in field strength as SAR is proportional to the square of AMF (inset of Fig. 7.10b) [8]. The rise in temperature is

also visualized from the IR thermogram (centre bright circle) and it further demonstrates the localized heating of MNPs (Fig. 7.10c and 7.10d). This is highly advantageous for the *in-vitro* hyperthermia treatment of cancer.
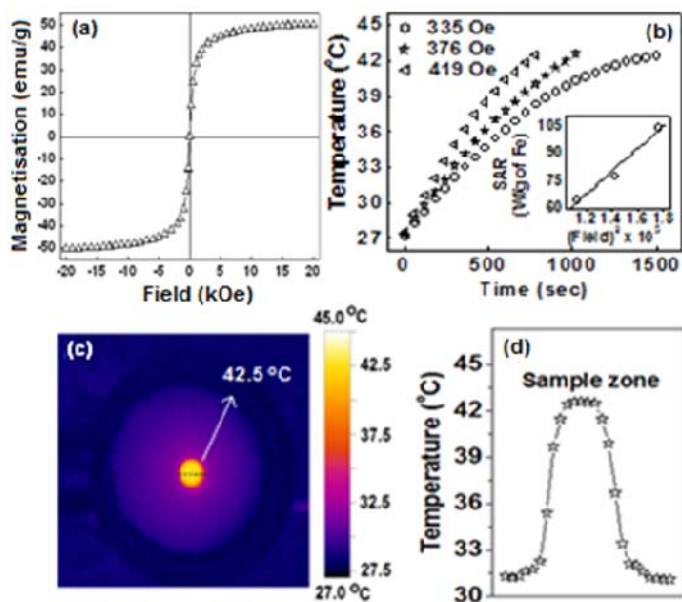
Fig. 7.10. *(a) M vs. H plot (b) Temperature vs. time plot (inset: SAR vs. field^2 plot), (b) IR thermogram and (c) temperature profile (along dotted line of fig. 7.10 c) of FLIONs.*

7.3.6. Hemocompatibility and protein resistance behaviour of FLIONs

The colloidal stability, magnetization and magnetic hyperthermia results of FLIONs prompted us to investigate their hemocompatibility and protein resistance characteristics for further *in-vivo* use. The hemocompatibility of FLIONs was assessed by the hemolysis assay and the percentage of hemolysis was found to be 3% upon incubation of 0.5 mg of FLIONs. This low percentage of hemolysis (<5%) indicates the good hemocompatibility of FLIONs. We also investigated the interaction of these nanoparticles with BSA protein in physiological medium (0.01 M PBS, pH 7.3). The

FLIONs do not show any significant change in the zeta-potential even after incubation with BSA for 2 h, revealing their protein resistance characteristics in physiological medium.

7.4. Summary

A simple facile approach for the preparation of amino acid passivated Fe_3O_4 aqueous colloidal NPs of average size about 10 nm by a soft chemical approach is described. The detailed structural analyses by FTIR, TGA, light scattering techniques, magnetic measurements and induction heating experiments confirmed the successful passivation/ functionalization of Fe_3O_4 NPs with glycine molecules. The free NH_2 groups on the surface of AIONs were used for the conjugation of folic acid and luminescent (FITC) molecules to achieve drug targeting and drug tracking respectively. These folate-conjugated luminescent iron oxide nanoparticles show good colloidal stability, optimal magnetization, biocompatibility with good specific absorption rate (under external AC magnetic field). The above features are highly conducive for application of these MNPs for hyperthermia treatment of cancer.

Chapter 8

Conclusion and future scope

Colloidal NPs of uniform-sized and well-defined morphology have attracted much attention because of their unique physico-chemical properties, as compared with those of their bulk counterparts. Among the others, MNPs have received a great deal of attention and extensively used for various biomedical applications, such as contrast enhancement agents in magnetic resonance imaging, magnetic carriers for drug delivery systems, biological labeling, and hyperthermia. The present thesis demonstrated the facile synthesis, characterization and applications of multifunctional MNPs for cancer treatment. As magnetic properties are size and chemical composition dependent, the first objective was the synthesis of MNPs with tunable size and narrow particle size distribution. Co-precipitation method has been employed as low-temperature synthetic strategy, as the solvent used in this strategy is environmental friendly (water) and the yield is high and scalable.

The carboxyl PEGylated Fe_3O_4 magnetic nanoparticles (CPMN) were synthesized through co-precipitation of Fe^{2+} and Fe^{3+} in basic medium followed by *in-situ* coating of PEG-diacid. The free carboxyl group present on CPMN can provide accessible surface for conjugation of various biomolecules/ biolabelling for a variety of biomedical applications. These CPMN are biocompatible and show good heating ability under AC magnetic field. They also show high loading affinity for anticancer drug (DOX) and their pH dependent sustained release. Further, the effective transfer of heat from the magnetic core to the surrounding medium is one of the key requirements of thermal therapy. Conducting polymer shell is important for the easy transport of heat from the core of MNPs to the medium for the killing of the cancer cells. Due to the presence of negative surface charge on CPMN, the surface of these particles gets modified with conducting polyaniline. XRD and TEM revealed the

formation of inverse spinel Fe_3O_4 NPs of size 10 nm. In order to assess the potential of polyaniline shell cross-linked magnetic nanoparticles (PSMN) in hyperthermia, their magnetic and thermomagnetic properties were investigated. PSMN exhibit superparamagnetic behaviour at 300 K. The maximum magnetization was found to be 63.5 emu/g at 20 kOe. Additionally, the time-dependent calorimetric measurements show good specific absorption rate (SAR) of PSMN suspension, which indicate that these NPs can also be used as effective heating source for hyperthermia treatment of cancer. The MTT assay with WEHI-164 cells clearly shows that PSMN suspension is highly cytocompatible and does not have toxic effect for further *in vivo* use. The presence of PANI and PEG moiety in PSMN could be advantageous for the effective heat transport from the Fe_3O_4 core to the surrounding medium. Thus, superparamagnetism and cytocompatibility make these particles as an ideal material for various biomedical applications, such as hyperthermia treatment of cancer cells.

Phosphate anchored Fe_3O_4 magnetic nanocarriers (PAMN) of average size about 10 nm are synthesized by facile soft-chemical approach. The formation of highly crystalline single phase Fe_3O_4 nanostructures is revealed by XRD and TEM measurements. The functionalization of MNPs with phosphate moiety is evident from FTIR, TGA, DLS and zeta-potential measurements. These superparamagnetic nanocarriers exhibit better colloidal stability and good biocompatibility with excellent heating efficacy under AC magnetic field. These NPs showed sustained release profile of anticancerous drug, DOX under acidic environment. This sustained release of drug is desirable for cancer therapy as the relatively low pH in tumours will specifically stimulate the release of drug at the target site.

In order to achieve site specific targeted drug delivery, bifunctional magnetic nanoparticles (BMNPs) were investigated. BMNPs contain two free functional groups i.e. carboxylic group for drug binding and folate receptor for drug targeting. BMNPs were prepared by introducing bioactive cysteine molecules onto the surface of undecenoic acid coated Fe_3O_4 magnetic nanoparticles (UMNPs) via thiol-ene click reaction. The XRD and TEM analysis reveal the formation of highly crystalline single-phase Fe_3O_4 nanostructures. These nanocarriers are of average size 10 nm and resistant to protein adsorption under physiological medium. FTIR spectra clearly suggest that cysteine molecules were successfully conjugated to the surface of UMNPs. The changes in the interfacial characteristics of the particles and the presence of organic coating were confirmed from dynamic light scattering, zeta-potential, thermogravimetric and field-dependent magnetic measurements. Induction heating experiments suggest that these nanocarriers possess excellent self-heating efficiency under external AC magnetic field. The efficacy of the carriers in heat activated killing of cancer cells is expressed in terms of the specific absorption rate (SAR). The SAR values of BMNC (1 mg/ml of Fe) were found to be 41.2, 64.0 and 88.0 W/g of Fe with an applied field of 0.251, 0.335 and 0.419 kOe, respectively (at a fixed frequency of 265 kHz). This indicates superior heating ability of these particles. Further, the infrared thermal imaging indicates that the temperature rise can be localized to the region of interest. To achieve site specific targeting of the carrier to cancer cells, the cysteine functionalized particles were conjugated with folic acid via amide linkage. This leads to the formation of bifunctional particles with free carboxyl group on cysteine for binding of cationic drugs like doxorubicin. These folate conjugated

nanoparticle (FBMNPs) show high loading affinity for doxorubicin and pH dependent release profile.

MNPs conjugated with specific luminescent markers (FITC, lanthanides) are used to track the MNP location in the body from the fluorescence images. The synthesis of folate-conjugated luminescent iron oxide nanoparticles (FLIONs) and their application has been explored. XRD and TEM analyses reveal the formation of highly crystalline single-phase Fe_3O_4 NPs of size about 10 nm. The conjugation of folate receptor (folic acid, FA) and luminescent molecule (fluorescein isothiocyanate, FITC) onto the surface of NPs was evident from FTIR and UV-visible spectroscopy. These FLIONs show good colloidal stability, high magnetic field responsivity and excellent self-heating efficacy. Specifically, present thesis demonstrated different methods for preparation and surface functionalization of Fe_3O_4 magnetic nanoparticles, and their potential applications in hyperthermia and drug delivery.

Future Scope

Nanoparticles have incredible potential as an efficient drug delivery system. Especially, the uses of NPs as drug delivery vehicles show a significant improvement in cancer therapy. Nanoparticle based drug delivery systems offer unique advantages for cancer therapy over free drug administration. The targeted delivery can reduce the systemic side-effects that appear during traditional chemotherapy. Further, nanoparticle based drug delivery systems have strong potential to overcome some of the barriers to efficient targeting of cancer cells. Some of the future directions that can explore the use of MNPs are:

1. *In-vivo* studies of Fe_3O_4NPsfor biomedical applications such as MRI, hyperthermia and targeted drug delivery.

2. Incorporation of MNPs in lipid based delivery systems and to explore their biomedical applications.

Lipids being naturally occuring and biocompatible in nature, it offers excellent opportunity to incorporate magnetic and luminescent functionalities in lipid particles. Recently, there have been efforts to use photostable fluorescent organic molecules that display aggregation induced emission properties for non-invasive cellular tracking. (Ref: Kai Li1, Wei Qin, Dan Ding, Nikodem Tomczak, Junlong Geng, Rongrong Liu, Jianzhao Liu, Xinhai Zhang, Hongwei Liu, Bin Liu and Ben Zhong Tang. Photostable fluorescent organic dots with aggregation-induced emission (AIE dots) for non-invasive long-term cell tracing DOI: 10.1038/srep01150 (2013)). The high emission efficiency, large absorptivity, excellent biocompatibility, and strong photo bleaching resistance of the particles functionalized with cell penetrating peptides ensured outstanding long-term non-invasive *in-vitro* and *in-vivo* cell tracing. This opens new avenues in the development of fluorescent probes for following biological processes such as carcinogenesis. With this perspective, preliminary exploratory studies were carried out to incorporate organic luminescent additives in lipid particles and is included in this thesis as an Annexure.

PEG functionalized luminescent lipid particles for cellular imaging

A 1.1. Introduction

Surface functionalized particles are gaining increasing attention in biomedical research owing to their potential applications in areas such as cellular imaging and drug delivery etc. [276-277]. Delivery of active ingredients to the right place at right amount is important for effective therapy and reduced side effects. Interfacial modification of materials with specific functional groups offers attractive ways of targeting active ingredients to the site of interest and hence reduces drug toxicity [278]. Polyethylene glycol (PEG) grafted liposomal carriers have been employed for the passive targeting of anticancer drug, doxorubicin [279]. Some of the shortcomings of liposomal carriers include limited stability in biological fluids, electrolytes, effect of pH, temperature etc. Recently, efforts have been made for the development of alternate nanoparticulate drug delivery carriers formed by solid lipids or lecithins [280-282]. The use of solid lipids instead of liquid lipids is advantageous for the controlled release of drug molecules as drug mobility in a solid lipid is considerably slow. The physical and chemical stability of solid lipid particles in biological fluids are superior to those of liposomes, and at the same time maintains excellent biocompatibility offered by lipids. These particles have a tendency to incorporate both hydrophilic as well as hydrophobic drugs.

Recently, lecithin NPs have been prepared and explored for intravenous injection of docetaxel, a potent anticancer drug [282]. The drug loaded NPs showed enhanced accumulation in tumours of mice. Positively charged lecithin particles were also prepared by using cationic surfactant as a stabilizer for oil in water emulsions [283]. These particles showed excellent biocompatibility and are amenable for binding

of DNA and vaccine delivery [283]. Thus, engineered lecithin or solid lipid particles are emerging as new biocompatible materials for drug delivery. Adding luminescent functionality to the drug delivery carrier is important for cellular imaging, identify location of target carriers in the tissue and in-vivo monitoring of biomolecular interactions [284]. Impregnating phospholipids with fluorescent organic molecules could provide multiple functionalities to these NPs such as imaging and therapy [285]. Recently, highly stable luminescent vesicles have been prepared via spontaneous assembly of dimyristoylphosphatidylcholine and a fluorescent amphiphile [286].

Size selective preparation of biocompatible particles is another important aspect to achieve selective permeation and accumulation of cancer drugs in tumours [287]. Liposomal and polymeric carriers with sizes less than 100 nm are shown to be highly effective for treating permeable tumours [287-289]. In particular, polymeric micelles of diameter 30 nm could effectively penetrate pancreatic tumours which are otherwise poorly permeable to other sizes [288]. With this objective, we explored the possibility of using lipid solubilized microemulsions as a means to produce multifunctional drug carriers. Here, we report the preparation, characterization and cellular internalization of luminescent phospholipid (lecithin) particles which are surface functionalized with the hydrophilic PEG chains of a non-ionic surfactant. The prepared particles are of sub 100 nm size with narrow polydispersity, resistant to protein adsorption and shows good cellular uptake.

A 1.2. Synthesis of lipid particles (LPs) and luminescent lipid particles (LLPs)

Lipid particles were prepared by vacuum evaporation of lipid solubilized microemulsions (LSM) [290]. LSMs (oil-in-water) were prepared by solubilizing equal weights of FDA approved oil, isopropyl myristate (IPM) and a biocompatible

lipid (Phospholipon 90G) in a surfactant solution (Tween-80). First, equal weights (1.13 wt. %) of phospholipon 90G and IPM were mixed together by vortexing and then, LSM was obtained by microemulsifying the above mixture in 1 % aqueous tween-80 solution (5 ml), such that the lipid to surfactant mass ratio is 0.075. During solvent evaporation of LSMs under vacuum, the phospholipid is encapsulated with a protective shell of surfactants to form lipid particles (LPs).

To add luminescent functionality to these LPs, SHNC was incorporated into the lipid via pH induced partitioning. Briefly, 3.5 mM of SHNC was first added to 5 ml of LSM having 1 % of tween-80. Then, this microemulsion was evaporated at pH 1 to obtain the luminescent lipid particles (LLPs). These LLPs were redispersed in 2 ml of water and pH was adjusted to ~5 by dialysis against milli Q water for further use.

A 1.3.1. Size measurements of lipid solubilized microemulsion and lipid particles by SANS and DLS

The size distributions of the microemulsion droplets and the phospholipid particles formed by solvent evaporation-reconstitution procedure were monitored by dynamic light scattering and small angle neuron scattering. Fig. A 1.1 shows the SANS spectra of lipid solubilized microemulsion and a dilute dispersion of lipid particles prepared from the above microemulsion with a lipid to oil mass ratio of 1. The SANS spectra from micelles and the corresponding particles could be fitted well using spherical core-shell particle model (solid lines in Fig. A 1.1). The shift of the SANS spectra of lipid particles to lower Q values indicate an increase in the size of the particles, as compared to the microemulsion. From quantitative analysis of the SANS data, the core radius and shell thickness of the employed microemulsions are

found to be 3.2 nm and 2.4 nm respectively. The corresponding dimensions for the phospholipid particles prepared from the above microemulsion are 9.1 nm and 4.8 nm.
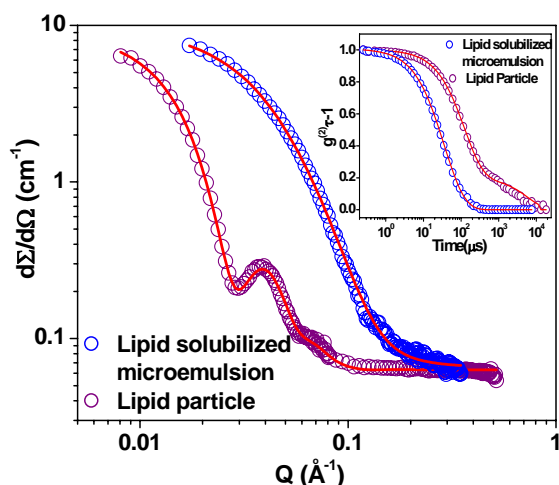
Fig. A 1.1. *SANS spectra of lipid solubilized microemulsion and lipid particles. Inset shows their autocorrelation function plots. The solid lines are fit to the experimental data.*

These results are consistent with the hydrodynamic diameter obtained from DLS. The autocorrelation function of the microemulsion and the corresponding lipid particles are included as inset of Fig. A 1.1. The autocorrelation function shows unimodal size distribution of lipid solubilized microemulsion. However, the autocorrelation function of lipid particles show a shoulder at long times indicating small fraction of aggregates. The shift of the correlation function for lipid particles to long time is consistent with SANS results. CONTIN analysis of the autocorrelation function of lipid particles indicate that the major contribution arises from stable phospholipid particles with an average diameter of about 26 nm while the average size of the lipid solubilized microemulsion is 9.7 nm (Fig. A 1.2).

It may be noted that the average size and distribution of the lipid particles formed is significantly larger than the size of microemulsions. This suggests initial agglomeration of the microemulsion droplets to produce large droplets during solvent evaporation. However, the absence of any phase separation in the reconstituted particles indicates that the phospholipid is not expelled from the core of the micelle-like particles. The steric stabilization provided by the self assembly of PEG chains of the surfactant on particle surface prevents agglomeration of the phospholipid particles after reconstitution. The hydrophobic chains of the surfactant are entrapped in the solid lipid core leaving an outer shell formed by the PEG part of the surfactant. This leads to excellent water dispersibility, stability and narrow polydispersity to the particles. Further, it is also observed that with an increase in oil to surfactant ratio, the average diameter of the particles increases. This is consistent with the expected behaviour of microemulsions in which the droplet radius can be controlled by varying the molar ratio of dispersed phase to surfactant.
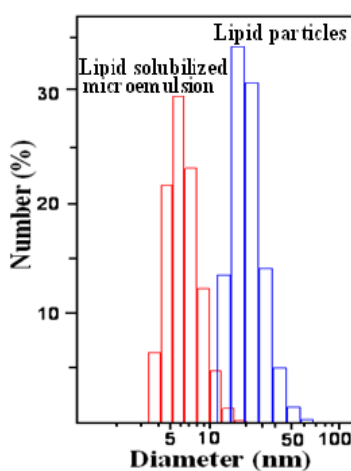
Fig. A 1.2. *DLS plots of lipid solubilized microemulsion (red) and lipid particles (blue).*

A 1.3.2. Zeta-potential measurements of lipid particles

Electrophoretic mobility measurements using phase analysis light scattering indicate the particles posses a zeta-potential of -6.1 mV (Fig. A 1.3). The excellent stability of these particles, inspite of the low surface potential, indicates the grafting of PEG chains on particle surface via self assembly.
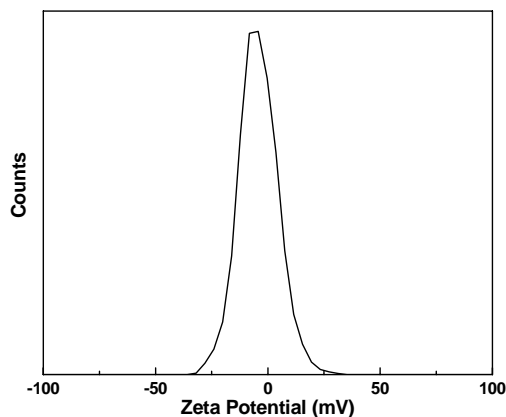
Fig. A 1.3. *Zeta-potential plot of lipid particles.*

A 1.3.3. Differential Scanning Calorimetric (DSC) measurements

In order to understand the melting of phospholipid chains in these particles, DSC experiments were performed at different lipid-surfactant ratios, keeping the surfactant concentration constant (Fig. A 1.4).The heating scans at different lipid-surfactant ratios showed an endothermic peak at $57.8^{o}C$ indicating the chain melting transition of the lipid. A crystalline core of the micelle is advantageous for slow transport of oxygen across the particle surface. This can limit the oxidative degradation of bioactive compounds [289].

A 1.3.4. Incorporation of luminescent moiety into lipid particles

To add luminescent functionality to these particles, an organic luminescent molecule is incorporated into the lipid via pH induced partitioning. As a model system

for pH induced loading of luminescent probes, we employed, 3-hydroxynaphthalene-2-carboxylic acid (HNC), commonly known as Bon acid, which is naphthalene based dye intermediate with good luminescence characteristics. The sodium salt of Bon acid (SHNC) is highly soluble in water while the protonated form is soluble in organic solvents. Luminescent lipid particles were obtained when the above microemulsions were evaporated in the presence of 0.075% of SHNC at a pH of 1. The NPs were dialyzed using dialysis membrane against nanopure water. DLS experiments confirmed that the average hydrodynamic diameter and polydispersity index show no significant changes upon incorporation of the luminescent probe. Fig. A 1.5 shows the emission and excitation spectra of luminescent lipid particles (λ_{ex} = 364 nm and λ_{em} = 530 nm). The inset shows photographs of lipid particles with and without luminescent additive under excitation using Xe lamp. The Tyndall effect of the lipid particles and green luminescence of the dye doped particles are clearly visible.
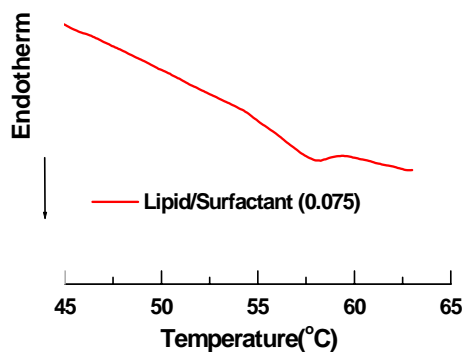
Fig. A 1.4. *DSC scans of lipid particles.*

A 1.3.5. Drug tracking by luminescent lipid particles

The most obvious use of such luminescent lipid particles is to track the localization of drug carriers in biological systems and detection of biomolecular

interactions. Fluorescent quantum dots, dye encapsulated silica particles etc. have been widely employed for cell tracking [290-291]. Recently, highly stable luminescent vesicles have been prepared via spontaneous assembly of dimyristoylphosphatidylcholine and a fluorescent amphiphile [292]. Typically, nanoparticle of radius around 25-30 nm has shown enhanced uptake at physiological conditions. Thus, we believe that these luminescent lipid NPs can be efficiently utilized for biosensing, bioimaging and drug targeting applications. Size selective delivery system based on polymeric micelles show enhanced pancreatic tumour uptake for 30 nm particles [286].
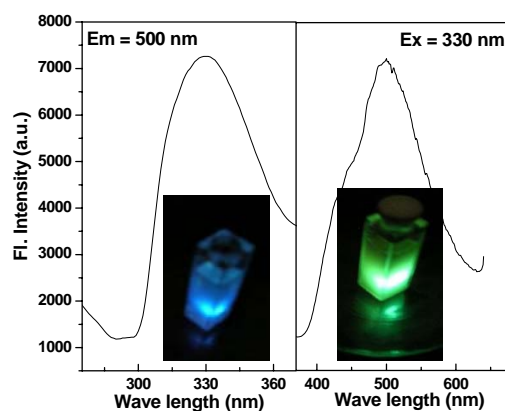
Fig. A 1.5. *Excitation and emission spectra of luminescent lipid particles. Inset shows the photographs of lipid solubilized microemulsion with (green) and without (blue) luminescent SHNC additive.*

The size distribution and zeta-potential of these particles did not change significantly when dispersed in PBS and BSA indicating the feasibility of dispersing them in isotonic solutions. (Fig. A 1.6). Also, the excellent stability in protein solutions is favorable for intravenous administration to the hosts. Previous reports

indicate that such PEG grafting on lecithin particles leads to enhanced cellular internalization in model cancer cell lines.
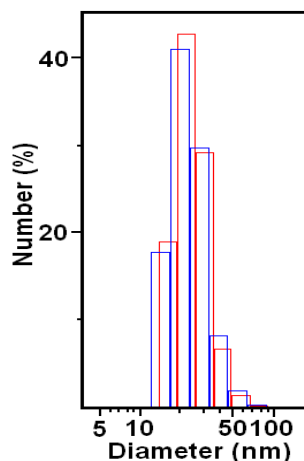
Fig. A 1.6. *DLS plots of lipid particles in BSA (blue) and PBS (red).*

PEG functionalization has been explored for delivery of paclitaxel as it can preferentially accumulate in tumours through enhanced permeability and retention (EPR) effect [293]. To explore the applications of luminescent lipid particles in bio-diagnostics, the cellular internalization of the particles was monitored using fluorescence imaging. Fig. A 1.7 shows the confocal microscopy images for WEHI-164 cells after incubation with fluorescent lipid particle. It can be observed that the fluorescent lipid NPs are located mostly in the cytoplasmic region of the cells. This result indicates that a significant amount of the lipid particles are successfully internalized in WEHI-164 cells.

Recent studies on diffusion of PEG functionalized polystyrene particles in mucus gel indicate that a high density of short PEG chains are highly conducive for the permeation of such particles through the mucus [276]. Mucus gel is viscous enough to trap pathogens or bacteria and hence can act as a barrier for drug molecules

or delivery systems. The fast diffusion of PEG functionalized particles in mucus gel indicate its potential of surpassing the mucosal barrier for treatment against diseases such as lung and cervix cancers. Moreover, the fluorescence emission from the NPs can be used for *in-vitro* or *in-vivo* imaging of cells.
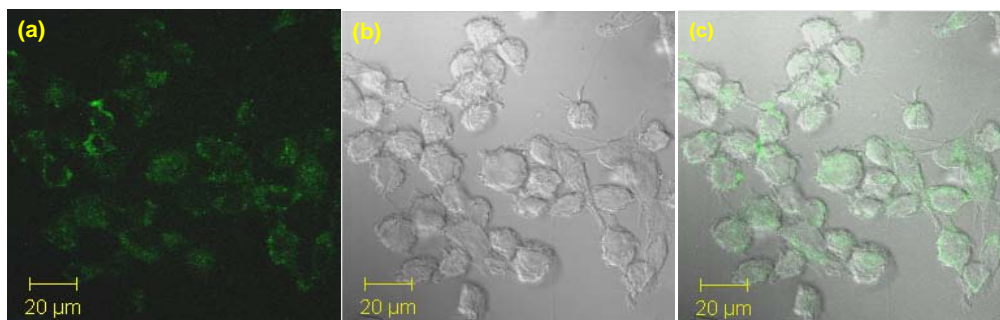
Fig. A 1.7. *Confocal microscopy images of WEHI-164 cells treated with fluorescent lipid particles: (a) fluorescence image, (b) bright field image and (c) merged image.*

A 1.4. Summary

A strategy to prepare size selective luminescent phospholipid particles with a PEG stealth using microemulsion route has been demonstrated. The size distribution of lipid particles can be tuned by changing the oil to surfactant ratio. Luminescent molecules can be physically trapped in the solid matrix while a biocompatible PEG stealth can be formed by anchoring non ionic surfactants on the surface of the particles. This methodology provides a convenient strategy to produce multifunctional lipid NPs for various biomedical applications such as cell labeling, imaging and drug delivery.

References

1.	S. H. Sun and C. B. Murray, *J. Appl. Phys.* **85** (1999) 4325.

2.	T. Hyeon, S. S. Lee, J. Park, Y. Chung and H. B. Na, *J. Am. Chem. Soc.* **123** (2001) 12798.

3.	 F. Dumestre, B. Chaudret, C. Amiens, P. Renaud and P. Fejes, *Science* **303** (2004) 821.

4.	 M. Chen, J. P. Liu and S. Sun, *J. Am. Chem. Soc.* **126** (2004) 8394.

5.	M. Chen and D. E. Nikles, *J. Appl. Phys.* **91** (2002) 8477.

6.	 E. V. Shevchenko, D. V. Talapin, H. Schnablegger, A. Kornowski, O. Festin, P. Svedlindh, M. Haase and H. Weller, *J. Am. Chem. Soc.* **125** (2003) 9090.

7.	 M. Chen and D. E. Nikles, *Nano Lett.* **2** (2002) 211.

8.	S. S. Shankar and S. Deka, *Sci. Adv. Mater.* **3** (2011) 169.

9.	M. Haruta, *J. New. Mat. Electrochem. Systems* **7** (2004) 163.

10.	S. J. Oldenburg, R. D. Averitt, S. L. Westcott and N. J. Halas, *Chem. Phys. Lett.* **288** (1998) 243.

11.	X. Huang, I. H. El-Sayed, W. Qian and M. A. El-Sayed, *J. Am. Chem. Soc.* **128** (2006) 2115.

12.	L. R. Hirsch, R. J. Stafford, J. A. Bankson, S. R. Sershen, B. Rivera, R. E. Price, J. D. Hazle, N. J. Halas and J. L. West, *Proc. Natl. Acad. Sci. U. S. A.* **100** (2003) 13549.

13.	M. G. Bawendi, M. L. Steigerwald and L. E. Brus, *Annu. Rev. Phys. Chem.* **41** (1990) 477.

14.	A. P. Alivisatos, *Science* **271** (1996) 933.

15. X. Michalet, F. F. Pinaud, L. A. Bentolila, J. M. say, S. Doose, J. J. Li, G. Sundaresan, A. M. Wu, S. S. Gambhir and S. Weiss, *Science* **307** (2005) 538.

16. L. Medintz, H. T. Uyeda, E. R. Goldman and H. Mattoussi, *Nat. Mater.* **4** (2005) 435.

17. M. Bruchez, M. Moronne, P. Gin, S. Weiss and A. P. Alivisatos, *Science* **281** (1998) 2013.

18. W. C. W. Chan and S. Nie, *Science* **281** (1998) 2016.

19.   J. K. Jaiswal, H. Mattoussi, J. M. Mauro and S. M. Simon, *Nat. Biotechnol.* **21** (2003) 47.

20. S. Courty, C. Luccardini, Y. Bellaiche, G. Cappello and M. Dahan, *Nano Lett.* **6** (2006) 1491.

21. W. Cai, D.- W. Shin, K. Chen, O. Gheysens, Q. Cao, S. X. Wang, S. S. Gambhir and X. Chen, *Nano Lett.* **6** (2006) 669.

22. S. Kim, Y. T. Lim, E. G. Soltesz, A. M. De Grand, J. Lee, A. Nakayama, J. A. Parker, T. Mihaljevic, R. G. Laurence, D. M. Dor, L. H. Cohn, M. G. Bawendi and J. V. Frangioni, *Nat. Biotechnol.* **22** (2004) 93.

23.   X. Gao, Y. Cui, R. M. Levenson, L. W. K. Chung and S. Nie, *Nat. Biotechnol.* **22** (2004) 969.

24. H. Kobayashi, Y. Hama, Y. Koyama, T. Barrett, C. A. S. Regino, Y. Urano and P. L. Choyke, *Nano Lett.* **7** (2007) 1711.

25. Z. A. Peng and X. Peng, *J. Am. Chem. Soc.* **123** (2000) 183.

26. J. M. Pietryga, D. J. Werder, D. J. Williams, J. L. Casson, R. D. Schaller, V. I. Klimov and J. A. Hollingsworth, *J. Am. Chem. Soc.* **130** (2008) 4879.

27. R. Werlin, J. H. Priester, M. E. Mielke, S. Krämer, S. Jackson, P. K. Stoimenov, G. D. Stucky, G. N. Cherr, E. Orias and P. A. Holden, *Nat. Nanotechnol.* **6** (2011) 65.

28. Y. H. Paik, H. S. Kojori and S. J. Kim, *Nanotechnology* **27** (2016).

29. I. Ahmed, S. G. Eriksson, E. Ahlberg, C. S. Knee, H. Götlind, L. G. Johansson, A. M. Matic Karlsson and L. Börjesson, *Solid State Ionics*, **178** (2007) 515-520.

30. F. Q. Hu, L. Wei, Z. Zhou, Y. L. Ran, Z. Li and M. Y. Gao, *Adv. Mater.* **18** (2006) 2553.

31. S. Mornet, S. Vasseur, F. Grasset and E. Duguet, *J. Mater. Chem.* **14** (2004) 2161.

32. J.-H. Lee, J.-T. Jang, J.-S. Choi, S. H. Moon, S.-H. Noh, J.-W. Kim, J.-G. Kim, I.-S. Kim, K. I. Park and J. Cheon, *Nat. Nanotechnol.* **6** (2011) 418.

33. B. D. Cullity and C. D. Graham, *Introduction to Magnetic Materials*, New York: Addison-Wesley, 1972.

34. D. Jiles, *Introduction to Magnetism and Magnetic Materials*, 1st ed. New York: Chapman and Hall, 1990.

35. E. C. Stoner and E. P. Wohlfarth, *Magnetics, IEEE Transactions* **27** (1991) 3475.

36. Brown and W. Fuller, *Physical Review* **130** (1963) 1677.

37. M. E. Fleet, *Acta Cryst. B* **37** (1981) 917.

38. C. Liu, B. Zou, A. J. Rondinone and Z. J. Zhang, *J. Am. Chem. Soc.* **122** (2000) 6263.

39. P. Pradhan, J. Giri, G. Samanta, H. D. Sarma, K. P. Mishra, J. Bellare, R. Banerjee and D. Bahadur, *J. Bio. Med. Mat. Res. B: Appl. Biomater.* **81b** (2007) 12.

40. S. S. Papell, *Low viscosity magnetic fluid obtained by the colloidal suspensions of magnetic particles,* US Patent No. 3 215 572, 1964.

41. W. C. Elmore, *Physical Review* **54** (1938) 1092.

42. L. F. Shen, P. E. Laibinis and T. A. Hatton, *Langmuir* **15** (1999) 447.

43. A. Wooding, M. Kilner and D. B. Lambrick, *J. Coll. Interf. Sci.* **144** (1991) 236.

44. R. F. Ziolo, E. P. Giannelis, B. A. Weinstein, M. P. O'Horo, B. N. Ganguly, V. Mehrotra, M. W. Russell and D. R. Huffman, *Science* **257** (1992) 219.

45. L. Zhang, G. C. Papaefthymiou and J. Y. Ying, *J. Appl. Phys.* **81** (1997) 6892.

46. R. Y. Hong, J.-H. Li, H.-Z. Li, J. Ding, Y. Zheng and D. G. Wei, *J. Magn. Magn. Mater.* **320** (2008) 1605.

47. C. Q. Hu, Z. H. Gao and X. R. Yang, *Chem. Phys. Lett.* **429** (2006) 513.

48. H. S. Nalwa, *Handbook of Nanostructured Materials and Nanotechnology* **1**, pp. 3.

49. R. M. Cornell, U. Schertmann and Weinheim, *Iron Oxides in the Laboratory: Preparation and Characterization,* VCH Publishers, Germany, 1991.

50. S. Chen, J. Feng, X. Guo, J. Hong and W. Ding, *Mater. Lett.* **59** (2005) 985.

51. D.-S. Bae, K.-S. Han, S. B. Cho and S. H. Choi, *Mater. Lett.* **37** (1998) 255.

52. S. Sun and H. Zeng, *J. Am. Chem. Soc.* **124** (2002) 8204.

53. C. Cannas, A. Musinu, A. Ardu, F. Orrù, D. Peddis, M. Casu, R. Sanna, F. Angius, G. Diaz and G. Piccaluga, *Chem. Mater.* **22** (2010) 3353.

54. K. A. Park, Y. Hwang, H. J. Noh, J. Y. Kim, J. H. Park, N. M. Hwang and T. Hyeon, *Nat. Mater.* **3** (2004) 891.

55. A.-H. Lu, E. L. Salabas and F. Schüth, *Angew. Chem*. **46** (2007) 1222.

56. K. C. barick, M. Aslam, Y. P. Lin, D. Bahadur, P. V. Prasad and V. P. Prasad, *J. Mat. Chem.* **19** (2009) 7023.

57. T. J. Mason and J. P. Lorimal, *Applied Sonochemistry*, New York, Wiley, 2002.

58. E. H. Kim, H. S. Lee, B. K. Kwak and B.-K. Kim, *J. Magn. Magn. Mater.* **289** (2005) 328.

59. J. Wang, J. Sun, Q. Sun and Q. Chen, *Mater. Res. Bull.* **38** (2003) 1113.

60. S. Komarneni and H. Katsuki, *Pure Appl. Chem.* **74** (2002) 1537.

61. A. López, T. Gonzàlez-Carreño, M. P. Morales and C. J. Serna, *J. Magn. Magn. Mater.* **383** (1995) 140.

62. G. Decher, *Science* **277** (1997) 1232.

63. S. Veintemillas- Verdaguer, M. P. Morales and C. J. Serna, *J. Appl. Organometal. Chem.* **15** (2001) 365.

64. H. Maeda, J. Wu, T. Sawa, Y. Matsumura and K. Hori, *J. Control. Rel.* **65** (2000) 271.

65. P. Decuzzi, F. Causa, M. Ferrari and P. A. Netti, *Annals Biomed. Eng.* **34** (2006) 633.

66. I. Brigger, C. Dubernet and P. Couvreur, *Adv. Drug Del. Rev.* **54** (2002) 631.

67. F. Q. Hu, L. Wei, Z. Zhou, Y. L. Ran, Z. Li and M. Y. Gao, *Adv. Mater.* **18** (2006) 2553.

68. J. Xie, C. Xu, N. Kohler, Y. Hou and S. Sun, *Adv. Mater.* **19** (2007) 3163.

69. F. Yu and V. C. Yang, *J. Biomed. Mater. Res. A* **92** (2010) 1468.

70. M. Hasegawa and S. Hokkoku, Magnetic iron oxide-dextran complex and process for its production, US Patent 4, 101, 435: July 18, 1978.

71. P. Pradhan, J. Giri, R. Banerjee, J. Bellare and D. Bahadur, *J. Magn. Magn. Mater.* **311** (2007) 282.

72. B. Feng, R. Y. Hong, L. S. Wang, L. Guo, H. I. Li, J. Ding, Y. Zheng and D. G. Wei, *Colloids Surf., A* **328** (2008) 52.

73. L. T. Mai Hoa, T. T. Dung, T. M. Danh, N. H. Duc and D. M. Chien, *Journal of Physics: Conference Series* **187** (2009) 012048.

74. P. J. Photos, L. Bacakova, B. Discher, F. S. Bates and D. E. Discher, *J. Control. Release* **90** (2003) 323.

75. L. E. Vlerken, T. K. Vyas and M. M. Amiji, *Pharmaceutical research* **24** (2007) 1405.

76. J. Zhang and R. D. K. Misra, *Acta Biomater.* **3** (2007) 838.

77. J. Qin, S. Laurent, Y. S. Jo, A. Roch, M. Mikhaylova, Z. M. Bhujwalla, R. N. Muller and M. Muhammed, *Adv. Mater.* **19** (2007) 1874.

78. B. Pan, D. Cui, Y. Sheng, C. Ozkan, F. Gao, R. He, Q. Li, P. Xu and T. Huang, *Cancer Res.* **67** (2007) 8156.

79. S. Chandra, S. Mehta, S. Nigam and D. Bahadur, *New J. Chem.* **34** (2010) 648.

80. M. Kumar, R. A. A. Muzzarelli, C. Muzzarelli, H. Sashiwa and A. J. Domb, *Chemical Reviews* **104** (2004) 6017.

81. K. A. Janes, P. Calvo and M. J. Alonso, *Adv. Drug Deliv. Rev.* **47** (2001) 83.

82. S. R. Bhattarai, K. C. R. Bahadur, S. Aryal, M. S. Khil and H. Y. Kim, *Carbohydrate Polymers* **69** (2007) 467.

83. S. R. Bhattarai, S. Y. Kim, K. Y. Jang, K. C. Lee, H. K. Yi, D. Y. Lee, H. Y. Kim and P. H. Hwang, *Journal of Virological Methods* **147** (2008) 213.

84. E. Munnier, S. C. Jonathan, C. Linassier, L. D. - Eyrolles, H. Marchais, M. Soucé, K. Hervé, P. Dubois and I. Chourpa, *Int. J. Pharma.* **361** (2008) 170.

85. K. C. Barick, M. Aslam, P. V. Prasad, V. P. Dravid and D. Bahadur, *J. Magn. Magn. Mater.* **321** (2009) 1529.

86. W. Stöber, A. Fink and E. J. Bohn, *Coll. Interf. Sci.* **26** (1968) 62.

87. Y. Zhang, S. W. Y. Gong, L. Jin, S. M. Li, Z. P. Chen, M. Ma and N. Gu, *Chinese Chem. Lett.* **20** (2009) 969.

88. C. W. Lai, Y. H. Wang, C. H. Lai, M. J. Yang, C. Y. Chen, P. T. Chou, C. S. Chan, Y. Chi, Y. C. Chen and J. K. Hsiao, *Small* **4** (2008) 218.

89. C. Xu, B. Wang and S. Sun, *J. Am. Chem. Soc.* **131** (2009) 4216.

90. J. K. Lim, S. A. Majetich and R. D. Tilton, *Langmuir* **25** (2009) 13384.

91. H.-Y. Park, M. J. Schadt, Lingyan, I. I. S. Lim, P. N Njoki, S. H. Kim, M.-Y. Jang, J. Luo and C.-J. Zhong, *Langmuir* **23** (2007) 9050.

92. S. Nagarajan and Z. Yong, *Recent Patents Biomed. Eng.* **1** (2008) 34.

93. P. Wust, B. Hildebrandt, G. Sreenivasa, B. Rau, J. Gellermann, H. Riess, R. Felix and P. M. Schlag, *The Lancet Oncology* **3** (2002) 487.

94. G. P. Raaphorst, M. L. Freeman and W. C. Dewey, *Radiat. Res.* **79** (1979) 390.

95. M. H. Falk and R. D. Issels, *Int. J. Hyperther.* **17** (2001) 1.

96. R. K. Gilchrist, R. Medal, W. D. Shorey, R. C. Hanselman, J. C. Parrott and C. B. Taylor, *Ann. Surg.* **146** (1957) 596.

97. J. van der Zee, Ann. Oncol. 2002, 13, 1173-1184.

98. A. K. Gupta and M. Gupta, *Biomaterials* **26** (2005) 3995.

99. B. A. Bornstein, P. S. Zouranjian, J. L. Hansen, S. M. Fraser, L. A. Gelwan, B. A. Teicher and G. K. Svensson, *J. Radiat. Oncol. Biol. Phys.* **25** (1993) 79.

100. A. Jordan, P. Wust, H. Fahling, W. John, A. Hinz and R. Felix, *Int. J. Hyperther.* **9** (1993) 51.

101. R. Ghosh, L. Pradhan, Y. P. Devi, S. S. Meena, R. Tewari, A. Kumar, S. Sharma, N. S. Gajbhiye, R. K. Vatsa, B. N. Pandey and R. S. Ningthoujam, *J. Mater. Chem.* **21** (2011) 13388.

102. R. E. Rosensweig, *J. Magn. Magn. Mater.* **252** (2002) 370.

103. J. P. Fortin, F. Gazeau and C. Wilhelm, *Eur. Biophys. J.* **37** (2008) 223.

104. D. L. Zhao, X. X. Wang, X. W. Zeng, Q. S. Xia and J. T. Tang, *J. Alloys Compd.* **477** (2009) 739.

105. K. Hayashi, K. Ono, H. Suzuki, M. Sawada, M. Moriya, W. Sakamoto and T. Yogo, *Chem. Mater.* **22** (2010) 3768.

106. P. B. Shete, R. M. Patil, R. S. Ningthoujam, S. Ghosh and S. H. Pawar, *New J. Chem.* **37** (2013) 3784.

107. D. Nevozhay, U. Kañska, R. Budzyñska and J. Boratyñski, *Postepy Hig Med Dosw* **61** (2007) 350.

108. J. Panyam and V. Labhasetwar, *Adv. Drug Deliv. Rev.* **55** (2003) 329–347.

109. S. S. Suri, H. Fenniri and B. Singh, *J Occup Med Toxicol* **2** (2007) 16.

110. A. Figuerola, R. Di Corato, L. Manna and T. Pellegrino, *Pharmacol Res* **62** (2010) 126.

111. M. M. Yallapu, S. F. Othman, E. T. Curtis, B. K. Gupta, M. Jaggi and S. C. Chauhan, *Biomaterials* **32** (2011) 1890.

112. W. Wu, B. Chen, J. Cheng, J. Wang, W. Xu, L. Liu, G. Xia, H. Wei, X. Wang, M. Yang, Y. Zhang, C. Xu and J. Li, *Int. J. Nanomedicine* **5** (2010) 1079.

113. S. Nigam, K. C. Barick and D. Bahadur, *J. Magn. Magn. Mater.* **323** (2011) 237.

114. S. Guo, D. Li, L. Zhang, J. Li and E. Wang, *Biomaterials* **30** (2009) 1887.

115. X. Yang, H. Hong, J. J. Grailer, I. J. Rowland, A. Javadi, S. A. Hurley, Y. Xiao, Y. Yang, Y. Zhang, R. J. Nickles, W. Cai, D. A. Steeber and S. Gong, *Biomaterials* **32** (2011) 4155.

116. S. M. Moghimi, A. C. Hunter and J. C. Murray, *Pharmacological Reviews* **53** (2001) 283.

117. L. T. Chen and L. Weiss, *Blood* **41** (1973) 529.

118. H. Soo Choi, W. Liu, P. Misra, E. Tanaka, J. P. Zimmer, B. Itty Ipe, M. G. Bawendi and J. V. Frangioni, *Nat. Biotechnol.* **25** (2007) 1165.

119. V. Torchilin, *Adv. Drug Deliv. Rev.* **63** (2011) 131.

120. H. Maeda, *Advances in Enzyme Regulation*, Elsevier Science Ltd., Oxford (2001) 189.

121. J. Fang, H. Nakamura and H. Maeda, *Adv. Drug Deliv. Rev.* **63** (2011) 136.

122. A. E. Nel, L. Madler, D. Velegol, T. Xia, E. M. V. Hoek, P. Somasundaran, F. Klaessig, V. Castranova and M. Thompson, *Nat. Mater.* **8** (2009) 543.

123. B. A. Kairdolf, M. C. Mancini, A. M. Smith and S. Nie, *Anal. Chem.* **80** (2008) 3029.

124. X. Gao, Y. Cui, R. M. Levenson, L. W. K. Chung and S. Nie, *Nat. Biotechnol.* **22** (2004) 969.

125. O. Clément, N. Siauve, M. Lewin, E. de Kerviler, C. A. Cuenod and G. Frija, *Biomed. & Pharmacother.* **52** (1998) 51.

126. D. D. Stark, R. Weissleder, G. Elizondo, P. F. Hahn, S. Saini, L. E. Todd, J. Wittenberg and J. T. Ferrucci, *Radiology* **168** (1988) 297.

127. V. P. Torchilin, *Adv. Drug Deliv. Rev.* **58** (2006) 1532.

128. K. Cho, X. Wang, S. Nie, Z. G. Chen and D. M. Shin, *Clin. Cancer Res.* **14** (2008) 1310.

129. J. L. Arias, *Mini Rev. Med. Chem.* **11** (2011) 1.

130. P. Couvreur and C. Vauthier, *Pharm. Res.* **23** (2006) 1417.

131. D. A. Scheinberg, C. H. Villa, F. E. Escorcia and M. R. McDevitt, *Nat. Rev. Clin. Oncol.* **7** (2010) 266.

132. A. T. Florence, *J. Control. Release* **164** (2012) 115.

133. T. Lammers, F. Kiessling, W. E. Hennink and G. Storm, *J. Control. Release* **161** (2012) 175.

134. S. Taurin, H. Nehoff and K. Greish, *J. Control. Release* **164** (2012) 265.

135. M. Singh, *Curr. Pharm. Des.* **5** (1999) 443.

136. K. C. Gatter, G. Brown, I. Strowbridge, R. E. Woolston and D. Y. Mason, *J. Clin. Pathol.* **36** (1983) 539.

137. J. D. Heidel, Z. Yu, J. Y. Liu, S. M. Rele, Y. Liang, R. K. Zeidan, D. J. Kornbrust and M. E. Davis, *Proc. Natl. Acad. Sci.* U. S. A. **104** (2007) 5715.

138. J. Wu, Y. Lu, A. Lee, X. Pan, X. Yang, X. Zhao and R. J. Lee, *J. Pharm. Sci.* **10** (2007) 350.

139. L. Cattel and P. Couvreur, *J. Pharm. Sci.* **89** (2000) 1452.

140. B. Liang, M. L. He, C. Y. Chan, Y. C. Chen, X. P. Li, Y. Li, D. Zheng, M. C. Lin, H. F. Kung, X. T. Shuai and Y. Peng, *Biomaterials* **30** (2009) 4014.

141. E. K. Park, S. B. Lee and Y. M. Lee, *Biomaterials* **26** (2005) 1053.

142. J. Sudimack and R. J. Lee, *Adv. Drug Deliv. Rev.* **41** (2000) 147.

143. Y. Zhang, C. Sun, N. Kohler and M. Q. Zhang, *Biomed. Microdevices* **6** (2004) 33.

144. C. Sun, R. Sze and M. Q. Zhang, *J Biomed Mater Res Part A* **45** (2006) 550.

145. Y. F. Zhu, Y. Fang and S. Kaskel, *J. Phys. Chem. C* **114** (2010) 16382.

146. S. Zou, N. Cao, D. Cheng, R. Zheng, J. Wang, K. Zhu and X. Shuai, *Int. J. Nanomedicine* **7** (2012) 3823.

147. K. Watanabe, M. Kaneko and Y. Maitani, *Int. J. Nanomedicine* **7** (2012) 3679.

148. C. Alexiou, R. Jurgons, R. J. Schmid, C. Bergemann, J. Henke, W. Erhardt, E. Huenges and F. Parak, *J. Drug Target.* **11** (2003) 139.

149. I. Šafařík and M. Šafaříková, *Monatshefte für Chemie* **133** (2002) 737.

150. A. S. Lubbe, C. Alexiou and C. Bergemann, *J. Surg. Res.* **95** (2001) 200.

151. Z. M. Saiyed, S. D. Telang and C. N. Ramchand, *Biomagn. Res. Technol.* **1** (2003).

152. C. Alexiou, W. Arnold, R. J. Klein, F. G. Parak, P. Hulin, C. Bergemann, W. Erhardt, S. Wagenpfeil and A. S. Lubbe, *Cancer Res* **60** (2000) 6641.

153. Q. A. Pankhurst, J. Connolly, S. K. Jones and J. Dobson, *J. Phys. D: Appl. Phys.* **36** (2003) 167.

154. A. Ito, M. Shinkai, H. Honda and T. Kobayashi, *J Biosci Bioeng* **100** (2005) 1.

155. K. Hayashi, M. Nakamura, W.Sakamoto, T. Yogo, H. Miki, S. Ozaki, M. Abe, T. Matsumoto and K. Ishimura, *Theranostics* **3** (2013) 366.

156. K. C. Barick, S. Singh, N. V. Jadhav, D. Bahadur, B. N. Pandey and P. A. Hassan, *Adv. Funct. Mater.* **22** (2012) 4975.

157. P. Sharma, S. Brown, G. Walter, S. Santra and B. Moudgil, *Adv. Colloid Interface Sci.* **471** (2006) 123.

158. S. Maenosono, T. Suzuki and S. Saita, *J. Magn. Magn. Mater.*, **320** (2008) L79.

159. E. H. Kim, H. S. Lee, B. K. Kwak and B.-K. Kim, *J. Magn. Magn. Mater.* **289** (2005) 328.

160. W. S. Seo, J. H. Lee, X. Sun, Y. Suzuki, D. Mann, Z. Liu, M. Terashima, P. C. Yang, M. V. McConnell, D. G. Nishimura and H. Dai, *Nat. Mater.* **5** (2006) 971.

161. H. Kosuge, S. P. Sherlock, T. Kitagawa, M. Terashima, J. K. Barral, D. G. Nishimura, H. Dai and M. V. McConnell, *PLoS One* **6** (2011) e14523.

162. R. Pecora in "The Scattering of Light and Other Electromagnetic Radiation", Academic Press, New York, 1969.

163. M. D. Graef, Introduction to Conventional Transmission Electron Microscopy, Cambridge University Press, Cambridge, 2000, UK.

164. B. Fultz, J. M. Howe, Transmission Electron Microscopy and Diffractometry of Materials, Springer Berlin Heidelberg, 2008, New York.

165. M. Lundqvist, J. Stigler, T. Cedervall, T. Berggård, M. B. Flanagan, I. Lynch, G. Elia and K. Dawson, *ACS Nano* **5** (2011) 7503.

166. S. Laurent, D. Forge, M. Port, A. Roch, C. Robic, L. V. Elst and R. N. Muller, *Chem. Rev.* **108** (2008) 2064.

167. O. Veiseh, J. W. Gunn, and M. Zhang, *Adv. Drug Deliv. Rev.* **62** (2010) 284.

168. K. N. Jayaprabha and P. A. Joy, *J. Nanofluids* **3** (2014) 1.

169. P. B. Shete, R. M. Patil, N. D. Thorat, A. Prasad, R. S. Ningthoujam, S. J. Ghosh, and S. H. Pawar, *Appl. Surf. Sci.* **288** (2014) 149.

170. K. C. Barick, S. Singh, D. Bahadur, M. A. Lawande, D. P. Patkar, and P. A. Hassan, *J. Colloid Interf. Sci.* **418** (2014) 120.

171. S. Chandra, K. C. Barick, and D. Bahadur, *Adv. Drug Deliv. Rev.* **63** (2011) 1267.

172. J. L. Lyon, D. A. Fleming, B. Stone, P. Schiffer and M. E. Willians, *Nano. Lett.* **4** (2004) 719.

173. R.-Y. Hong, J.-H. Li, S.-Z. Zhang, H.-Z. Li, Y. Zheng, J. Ding, D. -G. Wei, *Appl. Surf. Sci.* **255** (2009) 3485.

174. J. Sangeetha, S. Thomas, J. Arutchelvi, M. Doble, and J. Philip, *J. Biomed. Nanotechnol.* **9** (2013) 751.

175. S. Dietrich, S. Chandra, C. Georgi, S. Thomas, D. Makarov, S. Schulze, M. Hietschold, M. Albrecht, D. Bahadur, and H. Lang, *Mater. Chem. Phys.* **132** (2011) 292.

176. J. Xie, C. Xu, N. Kohler, Y. Hou, and S. Sun, *Adv. Mater.* **19** (2007) 3163.

177. N. Kohler, G. E. Fryxell, and M. Zhang, *J. Am. Chem. Soc.* **126** (2004) 7206.

178. C. Sun, K. Du, C. Fang, N. Bhattarai, O. Veiseh, F. Kievit, Z. Stephen, D. Lee, R. G. Ellenbogen, B. Ratner, and M. Zhang, *ACS Nano* **4** (2010) 2402.

179. W. Lin, M. C. Garnett, E. Schacht, S. S. Davis, and L. Illum, *Int. J. Pharm.* **189** (1999). 161.

180. V. P. Torchilin and V. S. Trubetskoy, *Adv. Drug Deliv. Rev.* **16** (1995). 141.

181. J. Sun, G. Z. Gu, and Y. F. Qian, *J. Biomed. Eng.* **20** (2003). 8.

182. S. Rana, N. V. Jadhav, K. C. Barick, B. N. Pandey, and P. A. Hassan, *Dalton Trans.* **43** (2014). 12263.

183. K. C. Barick and P. A. Hassan, *J. Coll. Interf. Sci.* **369** (2012) 96.

184. S. Nigam, K. C. Barick, and D. Bahadur, *J. Magn. Magn. Mater.* **323** (2011) 237.

185. H. Zhang, R. Wang, G. Zhang, and B. Yang, *Thin Solid Films* **429** (2003) 167.

186. E. Occhipinti, P. Verderio, A. Natalello, E. Galbiati, M. Colombo, S. Mazzucchelli, A. Salvad, P. Tortora, S. M. Doglia, and D. Prosperi, *Nanoscale* **3** (2011) 387.

187. F. Hu, K. W. MacRenaris, E. A. Waters, E. A. Schultz-Sikma, A. L. Eckermann, and T. J. Meade, *Chem. Commun.* **46** (2010) 73.

188. T. Muthukumaran, G. Gnanaprakash, and J. Philip, *J. Nanofluids* **1** (2012) 85.

189. J. Smit and H. P. J. Wijn, Ferrites, Wiley, New York (1959) pp 136–175.

190. L. S. Goldstein, M. W. Dewhirst, M. Repacholi, and L. Kheifets, *Int. J. Hyperth.* **19** (2003) 373.

191. C. S. S. R. Kumar and F. Mohammad, *Adv. Drug Deliv. Rev.* **63** (2011) 789.

192. A. Tomitaka, T. Koshi, S. Hatsugai, T. Yamada, and Y. Takemura, *J. Magn. Magn. Mater.* **323** (2011) 1398.

193. M. Kallumadil, M. Tada, T. Nakagawa, M. Abe, P. Southern, and Q. A. Pankhurst, *J. Magn. Magn. Mater.* **321** (2009) 1509.

194. E. Munnier, F. Tewes, S. Cohen-Jonathan, C. Linassier, L. Douziech-Eyrolles, H. Marchais, M. Soucé, K. Hervé, P. Dubois, and I. Chourpa, *Chem. Pharm. Bull.* **55** (2007) 1006.

195. P. Sharma, S. Rana, K. C. Barick, C. Kumar, H. G. Salunke and P. A. Hassan, *New J. Chem.* **38** (2014) 5500.

196. T. J. Higuchi, *J. Pharm. Sci.* **52** (1963) 1145.

197. H. Oliveira, E. Pérez-Andrés, J. Thevenot, O. Sandre, E. Berra and S. Lecommandoux, *J. Control. Rel.* **169** (2013) 165.

198. M. Liong, J. Lu, M. Kovochich, T. Xia, S. G. Ruehm, A. E. Nel, F. Tamanoi and J. I. Zink, *ACS Nano* **2** (2008) 889.

199. X. F. Zhang, S. Mansouri, L. Clime, H. Q. Ly, L. H. Yahia and T. Veres, *J. Mater. Chem.* **22** (2012) 14450.

200. N. Kohler, C. Sun, A. Fichtenholtz, J. Gunn, C. Fang and M. Zhang, *Small* **2** (2006) 785.

201. A. Aqil, S. Vasseur, E. Duguet, C. Passirani, J. P. Benoît, R. Jérôme and C. Jérôme, *J. Mater. Chem.* **18** (2008) 3352.

202. J. Hu, Y. Qian, X. Wang, T. Liu and S. Liu, *Langmuir* **28** (2012) 2073.

203. M. Das, P. Dhak, S. Gupta, D. Mishra, T. K. Maiti, A. Basak and P. Pramanik, *Nanotechnol.* **21** (2010) 125103.

204. D.-L. Zhao, H.-L. Zhang, X.-W. Zeng, Q.-S. Xia and J.-T. Tang, *Biomed Mater.* **1** (2006) 198.

205. X. L. Liu, H. M. Fan, J. B. Yi, Y. Yang, E. S. G. Choo, J. M. Xue, D. D. Fan and J. Ding, *J. Mater. Chem.* **22** (2012) 8235.

206. V. M. Khot, A. B. Salunkhe, N. D. Thorat, R. S. Ningthoujam and S. H. Pawar, *Dalton Trans.* **42** (2013) 1249.

207. K. C. Barick and P. A. Hassan, *J. Coll. Interf. Sci.* **369** (2012) 96.

208. S. Mornet, S. Vasseur, F. Grasset and E. Duguet, *J. Mater. Chem.* **14** (2004) 2161.

209. J. V. der Zee, *Ann. Oncol.* **13** (2002) 1173.

210. G. Bidan, O. Jarjayes, J. M. Fruchar and E. Hannecart, *Adv. Mater.* **6** (1994) 152.

211. J. Deng, X. Ding, W. Zhang, Y. Peng, J. Wang, X. Long, P. Li and A. C. Chan, *Polymer* **43** (2002) 2179.

212. C.-L. Zhu, S.-W. Chou, S.-F. He, W.-N. Liao and C.-C. Chen, *Nanotechnol.* **18** (2007) 275604.

213. Q. Yu, M. Shi, Y. Cheng, M. Wang and H.-Z. Chen, *Nanotechnol.* **19** (2008) 265702.

214. J. Jang, J. Ha and B. Lim, *Chem. Commun.* (2006) 1622.

215. J. Yin, X. Wang, R. Chang and X. Zhao, *Soft Matter.* **8** (2012) 294.

216. B. González, E. Ruiz-Hernández, M. J. Feito, C. L. de Laorden, D. Arcos, C. Ramírez-Santillán, C. Matesanz, M. T. Portolés and M. Vallet-Regí, *J. Mater. Chem.* **21** (2011) 4598

217. M. Mikhaylova, D. Y. Kim, N. Bobrysheva, M. Osmolowsky, V. Semenov, T. Tsakalakos and M. Muhammed, *Langmuir* **20** (2004) 2472.

218. B. Samanta, H. Yan, N. O. Fischer, J. Shi, D. J. Jerry and V. M. Rotello, *J. Mater. Chem.* **18** (2008) 1204.

219. M. Motskin, D. M. Wright, K. Muller, N. Kyle, T. G. Gard, A. E. Porter and J. N. Skepper, *Biomaterials* **30** (2009) 3307.

220. F. A. D. Wolf, K. Nicolay and B. D. Kruijff, *Biochem.* **31** (1992) 9252.

221. S. Li, Y. Ma, X. Yue, Z. Cao and Z. Dai, *New J. Chem.* **33** (2009) 2414.

222. J. -H. Lee, Y. -M. Huh, Y. Jun, J. -W. Seo, J. -T. Jang, H. -T. Song, S. J. Kim, E. -J. Cho, H. -G. Yoon, J. -S. Suh and J. Cheon, *Nat. Med.* **13** (2007) 95.

223. S. Mondini, S. Cenedese, G. Marinoni, G. Molteni, N. Santo, C. L. Bianchi and A. Ponti, *J. Coll. Interf. Sci.* **322** (2008) 173.

224. S. C. Wuang, K. G. Neoh, E. -T. Kang, D. W. Pack and D. E. Leckband*, J. Mater. Chem.* **17** (2007) 3354.

225. H. H. P. Yiu, H. -J. Niu, E. Biermans, G. Tendeloo and M. J. Rosseinsky, *Adv. Funct. Mater.* **20** (2010) 1599.

226. M. Textor, L. Ruiz, R. Hofer, A. Rossi, K. Feldman, G. Hähner and N. D. Spencer, *Langmuir* **16** (2000) 3257.

227. C. Yee, G. Kataby, A. Ulman, T. Prozorov, H. White, A. King, M. Rafailovich, J. Sokolov and A. Gedanken, *Langmuir* **15** (1999) 7111.

228. O. K. Borggaard, B. Raben-Lange, A. L. Gimsing and B. W. Strobel, *Geoderma* **127** (2005) 270.

229. Y. Sahoo. H. Pizem, T. Fried, D. Golodnitsky, L. Burstein, C. N. Sukenik and G. Markovich, *Langmuir* **17** (*2001) 7907.

230. D. I. Kreller, G. Gibson, W. Novak, G. W. vanLoon and J.H. Horton, *Coll. Surf. A* **212** (2003) 249.

231. M. A. White, J. A. Johnson and J. T. Koberstein, *J. Am. Chem. Soc.* **128** (2006) 11356.

232. L. Qi, J. Fresnais, P. Muller, O. Theodoly, J.-F. Berret and J.-P. Chapel, *Langmuir* **28** (*2012) 11448.

233. C. D. Cruz , O. Sandre and V. Cabuil, *J. Phys. Chem. B* **109** (*2005) 14292.

234. G. Lamanna, M. Kueny-Stotz, H. Mamlouk-Chaouachi, C. Ghobril, B. Basly, A. Bertin, I. Miladi, C. Billotey, G. Pourroy, S. Begin-Colin and D. Felder-Flesch, *Biomater.* **32** (2011) 8562.

235. J. Auernheimer, D. Zukowski, C. Dahmen, M. Kantlehner, A. Enderle, S. L. Goodman and H. Kessler, *Chem. Bio. Chem.* **6** (2005) 2034.

236. H. J. Parab, J.-H. Huang, T.-C. Lai, Y.-H. Jan, R.-S. Liu, J.-L. Wang, M. Hsiao, C.-H. Chen, Y.-K. Hwu, D. P. Tsai, S.-Y. Chuang and J. H. S. Pang, *Nanotechnol.* **22** (2011) 395706.

237. A. Gupta, P. Singh and C. Shivakumara, *Sol. State Commun.* **150** (2010) 386.

238. N. X. Wang, Y. Q. Wang, X. W. He and W. Y. Li, *J. Nanosci. Nanotechnol.* **11** (2011) 4039.

239. M. Kuppayee, G. K. V. Nachiyar and V. Ramasamy, *Appl. Surf. Sci.* **257** (2011) 6779.

240. A. Tiwari, S. A. Khan and R. S. Kher, *Adv. Appl. Sci. Res.* **2** (2011) 105.

241. M. R. Ahsan, M.A. Uddin and M. G. Mortuza, *Indian J. Pure Appl. Phys.* **43** (2005) 89.

242. J. E. Wong, A. K. Gaharwar, D. Müller-Schulte, D. Bahadur and W. Richtering, *J. Nanosci. Nanotechnol.* **8** (2008) 4033.

243. R. Hergt and W. Andrä, (2007) Magnetic Hyperthermia and Thermoablation, in Magnetism in Medicine: A Handbook, 2nd Edition (eds. W. Andrä and H. Nowak), Wiley-VCH Verlag GmbH & Co. KGaA, Weinheim, Germany.

244. H. M. Joshi, Y. P. Lin, M. Aslam, P. V. Prasad, E, A. Schultz-Sikma, R. Edelman, T. Meade and V. P. Dravid, *J. Phys. Chem. C* **113** (2009) 17761.

245. N. K. Prasad, K. Rathinasamy, D. Panda and D. Bahadur, *J. Mater. Chem.* **17** (2007) 5042.

246. J. P. Fortin, C. Wilhelm, J. Servais, C. Menager, J. C. Bacri and F. Gazeau, *J. Am. Chem. Soc.* **129** (2007) 2628.

247. F. A. D. Wolf, K. Nicolay and B. D. Kruijff, *Biochem.* **31** (1992) 9252.

248. E. S. Day, J. G. Morton and J. L. West, *J. Biomech. Eng. Trans. ASME* **131** (2009) 074001.

249. F. Gazeau, M. Levy and C. Wilhelm, *Nanomedicine* **3** (2008) 831.

250. G. F. Goya, V. Grazu and M. R. Ibarra, *Curr. Nanosci.* **4** (2008) 1.

251. P. Drake, H.-J. Cho, P.-S. Shih, C.-H. Kao, K.-F. Lee, C.-H. Kuo, X.-Z. Lin and Y.-J. Lin, *J. Mater. Chem.* **17** (2007) 4914.

252. T. T. Luong, T. P. Ha, L. D. Tran, M. H. Do, T. T. Mai, N. H. Pham, H. B. T. Phan, G. H. T. Pham, N. M. T. Hoang, Q. T. Nguyen and P. X. Nguyen, *Colloids Surf. A: Physicochem. Eng. Aspects* **384** (2011) 23.

253. P. Pradhan, P. Pradhan, J. Giri, F. Rieken, C. Koch, O. Mykhaylyk, M. Döblinger, R. Banerjee, D. Bahadur and C. Plank, *J. Control. Release* **142** (2010) 108.

254. M. Arruebo, R. Fern_andez-Pacheco, M. R. Ibarra and J. Santamaria, *Nano Today* **2** (2007) 22.

255. J. D. G. Duran, J. L. Arias, V. Gallardo and A. V. Delgado, *J. Pharmaceutical Sci.* **97** (2008) 2948.

256. H. C. Kolb, M. G. Finn and K. B. Sharpless, *Angew. Chem.* **40** (2001) 2004

257. C. E. Hoyle and C. N. Bowman, *Angew. Chem.* **49** (2010) 1540.

258. S. Zhang, X. He, L. Chen and Y. Zhang, *New J. Chem.* **38** (2014) 4212.

259. L. Yingjuan and P. S. Low, *Adv. Drug Deliv. Rev.* **54** (2002) 675.

260. M. H. Majd, D. Asgari, J. Barar, H. Valizadeh, V. Kafil, A. Abadpour, E. Moumivand, J. S. Mojarrad, M. R. Rashidi, G. Coukos and Y. Omidi, *Colloids and Surfaces B: Biointerfaces* **106** (2013) 117.

261. S. Yang, D. Chen, N. Li, X. Mei, X. Qi, H. Li, Q. Xu and J. Lu, *J. Mater. Chem.* **22** (2012) 25354.

262. P. Huang, L. Bao, C. Zhang, J. Lin, T. Luo, D. Yang, M. He, Z. Li, G. Gao, B. Gao, S. Fu and D. Cui, *Biomater.* **32** (2011) 9796.

263. Y. Zhang, J. Li, M. Lang, X. Tang, L. Li and X. Shen, *J. Coll. Interf. Sci.* **354** (2011) 202.

264. M. Mahmoudi, A. Simchi, A. S. Milani and P. Stroeve, *J. Colloid Interface Sci.* **336** (2009) 510.

265. A. Aquil, S. Vasseur, E. Duguet, C. Passirani, J. P. Benoît, R. Jérôme and C. Jérôme, *J. mater. Chem.* **18** (2008) 3352.

266. N. Wu, L. Fu, M. Su, M. Aslam, K.C. Wong and V.P. Dravid, *Nano Lett.* **4** (2004) 383.

267. C.R. Vestal and Z. J. Zhang, *J. Am. Chem. Soc.* **124** (2002) 14312.

268. A. Sandhu, H. Handa and M. Abe, *Nanotechnology* **21** (2010) 442001.

269. Y.-C. Chang and D.-H. Chen, *J. Colloid Interface Sci.* **283** (2005) 446.

270. J. Cheon and J. -H. Lee, *Acc. Chem. Res.* **41** (2008) 1630–1640.

271. L. Wang, J. Bao, L. Wang, F. Zhang and Y. Li, *Chem. Euro. J.* **12** (2006) 6341.

272. J. Wang, B. Chen, J. Chen, X. Cai, G. Xia, R. Liu, P. Chen, Y. Zhang and X. Wang, *Int. J. Nanomed.* **6** (2011) 203.

273. F. Chen, Z.i. Ma, G. Dong and Z. Wu, *Acta Pharmacol. Sin*. **30** (2009) 485.

274. Y. Zhu, Y. Fang and S. Kaskel, *J. Phys. Chem. C* **114** (2010) 16382–16388.

275. Q. Yang and X. Pan, *J. Appl. Polym. Sci.* **117** (2010) 3639-3644.

276. Y. Cu and W. M. Saltzman, *Nature Mater.* **8** (2009) 11.

277. S. Ehrler, U. Pieles, A. Wirth-Heller and P. Shahgaldian, *Chem. Commun.* (2007) 2605.

278. T. M. Allen and P. R. Cullis, *Science* **303** (2004) 1818.

279. V. P. Torchilin, *Nature Rev.* **5** (2005) 145.

280. R. H. Muller and C. M. Keck, *J. Biotechnol.* **113** (2004)151.

281. H. L. Wong, R. Bendayan, A. M. Rauth, Y. Li and X. Y. Wu, *Adv. Drug Del. Rev.* **59** (2007) 491.

282. N. Yanasarn, B. R. Sloat and Z. Cui, *Int. J. Pharm.* **379** (2009) 174.

283. Z. Cui, F. Qiu and B. R. Sloat, *Int. J. Pharm.* **313** (2006) 206.

284. J. Jeong, E. Yun, Y. Choi, H-Y Jung, S. J. Chung, N. W. Song and B. H. Chung, *Chem.Commun.* **47** (2011) 10668.

285. Z. Liu, P. Koczera, D. Doleschel, F. Kiessling and J. Gätjens, *Chem. Commun.*, **48** (2012) 5142.

286. H. Cabral, Y. Matsumoto, K. Mizuno, Q. Chen, M. Murakami, M. Kimura, Y. Terada, M. R. Kano, K. Miyazono, M. Uesaka, N. Nishiyama and K. Kataoka, *Nature Nanotechnol.* **6** (2011) 815.

287. S. Zhang., J. Li, G. Lykotrafitis, G. Bao and S. Suresh, *Adv. Mater.* **21** (2009) 419.

288. L. Tang, T. M. Fan, L. B. Borst and J. Cheng, *ACS Nano* **6** (2012) 3954.

289. R. V. Tikekar and N. Nitin, *Soft Matter.* **7** (2011) 8149.

290. X. Michalet, F. Pinaud, L. Bentolila, J. Tsay, S. Doose, J. Li, G. Sundaresan, A. Wu, S. Gambhir and S. Weiss, *Science* **307** (2005) 538.

291. W. Kwon and S.-W. Rhee, *Chem.Commun.* **48** (2012) 5256.

292. D. Shi, G. Sfintes, B. W. Laursen and J. B. Simonsen, *Langmuir* **28** (2012) 8608.

293. M.-K. Lee, S.-J. Lim and C.-K. Kim, *Biomater.* **28** (2007) 2137.